AN IN SITU GAMMA-SPECTROMETRY SYSTEM FOR THE CHARACTERIZATION OF NON-CONVENTIONAL RADIONUCLIDES FOR MEDICAL RESEARCH

By

PINELOPI CHRISTODOULOU

A thesis submitted in partial fulfillment of
the requirements for the degree of

MASTER OF SCIENCE

INSTITUTIONS: COMPLUTENSE UNIVERSITY OF MADRID, CERN-MEDICIS
SUPERVISORS: DR. CHARLOTTE DUCHEMIN (MEDICIS - RUN COORDINATOR),
PROF. LUIS MARIO FRAILE PRIETO (GRUPO DE FÍSICA NUCLEAR, UCM)
Erasmus Mundus Joint Master Degree in Nuclear Physics

SEPTEMBER 2020

TABLE OF CONTENTS

LIST OF TABLES

LIST OF FIGURES

Acknowledgments

Writing a master thesis during a pandemic is surely not an easy task. Therefore, this thesis is not only representing the finale of my unique Erasmus Mundus Master's Degree studies, but it also stands as a reminder that effort and patience always pays off. I would like to thank those that helped me achieve this goal. The master thesis was organized to be partially placed in MEDICIS CERN thanks to the efforts of Professor Jose Miguel Arias Carrasco and Dr. Thierry Stora.

This thesis would not have been possible if it wasn't for the precious help from my supervisor Dr. Charlotte Duchemin, whose comments and suggestions were always to the point and constructive. Her friendly behaviour helped me easily adapt to my new working environment at CERN. Being part of the research group of MEDICIS was a truly motivating and rewarding experience. I shall always cherish the memories of the working environment either at the office (and the coffee breaks) or at the laboratory. Special thanks to Tassos Kanellakopoulos and Vasilis Samothrakis for their precious help and company.

Furthermore, this thesis was completed thanks to Professor Luis Fraile, who gave important feedback and managed to have frequent virtual meetings with me even during a pandemic. Unfortunately, I was not able to experience the working environment in Complutense University of Madrid and I am certain that I missed a great opportunity to meet and work alongside amazing people. However, even though we never met in person, I would like to thank Víctor Martínez Nouvillas, who took multiple measurements on my behalf in Madrid.

Lastly, I would like to thank my family and my dear friends (especially my friends from my Master's studies: Patricia, Sergio, Bharat, Jose thank you!) for always supporting me and encouraging me. And of course I would like to express my gratitude for my partner Giorgos, who believed in me and therefore helped me believe in myself.

Abstract

The MEDICIS (Medical Isotopes Collected from ISOLDE) facility is a new and unique facility located at CERN (Switzerland) dedicated to the production of non-conventional radionuclides for research and development in imaging, diagnostics and radiation therapy, with very high specific activity. CERN-MEDICIS has been commissioned in September 2017 and delivered its first radionuclides in December 2017. Since then, the facility is shipping novel radioisotopes for medical research to hospitals and scientific institutes in Switzerland and across Europe, which are part of the MEDICIS collaboration. Since its commissioning, the CERN-MEDICIS facility has shown the feasibility of providing radionuclides such as Tb-149, Tb-155, Er-169 and Yb-175 for innovative medical research. For that purpose, the facility used either the 1.4 GeV proton beam coming from the Proton Synchrotron Booster that irradiates the target in ISOLDE hall, a CERN nuclear physics facility, or sources provided by external institutes being part of the MEDICIS collaboration. The radionuclide of interest is extracted through mass separation and implanted on a thin metallic foil. The goal of this master thesis is first to characterize a GR-1 CZT detector from KROMEK with certified sources. The main objective of this project is then to assess the feasibility of using this kind of detector to get an on-line measurement of the activity being implanted on the collection foil. These measurements are complemented with simulations using PENELOPE Monte Carlo code system. Furthermore, other kinds of CZT detectors provided by the Complutense University of Madrid are also characterized in order to compare their capabilities with the ones of the GR-1 CZT detector.

Chapter One

Introduction

1.1 Scope of the Master Thesis

A plethora of novel and innovative radioisotopes can be collected in the MEDICIS facility. It is important to verify their activity so as to ensure the lack of contamination. Possible contaminations in the produced radioisotopes can be detrimental to the planned treatment as it can lead to the unnecessary irradiation of healthy tissues and increase the dose uptake.

The goal of this master thesis is to characterize a Cadmium Zink Telluride detector (GR-1 from KROMEK) with certified sources and to check the activity being implanted on the collection foil. The feasibility of using this detector for online measurements of the activity is ought to be validated with the collection Tb-155 and Sm-153 at MEDICIS laboratory.

The main objective of the detector is to control the activity accumulated during the collection. It is important to be able to react if there is a problem with the parameters of the production of the radioisotopes. In that case, it will be possible to tune the beam or laser parameters to collect as much activity as possible. The activity control is also ensuring the collection of the desired radionuclide.

Furthermore, different types of Cadmium Zink Telluride detectors (GR-05, SDP500S, LAB CPG, SPEAR) were analysed to check which model is better suited for the MEDICIS operation. This study was focused on Cadmium Zink Telluride (CZT) type of detectors, since

they are the most promising solution for monitoring of the activity, due to their relatively good energy resolution, good efficiency, their high count rate capability and the fact that they can operate at room temperature, without the need for cooling.

Moreover, the measurements were complemented with Monte Carlo simulations using PENMAIN. With the simulations it was possible to reproduce different experimental configurations and predict the experimental results with good precision. Finally, a dose accumulation assessment was performed using both Nucleonica and PENMAIN.

1.2 Nuclear Medicine

Nuclear Medicine utilizes radioisotopes for medical purposes such as diagnosis and therapy, by creating radio-pharmaceuticals that can be injected, ingested or inhaled by the patient.

According to the International Atomic Energy Agency (IAEA) (IAEA, 2016), the radiopharmaceuticals are radioisotopes linked to biological molecules, which are able to connect to particular organs, tissues or cells, thus targeting specifically the desired region of the human body. Usually, medical imaging is used to measure quantitatively the in-vivo biodistribution of the radiopharmateuticals. In the following section, information about radioisotopes, their applications, as well as their productions routes is presented.

1.3 Radioisotopes

Radioisotopes are unstable isotopes that spontaneously dissipate their excess energy in the form of radiation to produce a more stable atom (Carter, 2015).

Radioisotopes have a dual function; they can be used in therapy to directly irradiate the selected region and/or in diagnosis, where they function like a tracer that is being detected by a specific instrument.

Diagnostic radio-pharmaceuticals utilize radioisotopes that emit γ-rays. This is because

γ-rays easily penetrate the tissues and, therefore, are detected outside of the body. The half-life ($T_{1/2}$) of the radioisotope should last approximately the same as the duration of the medical test. The reason for this is the possibility to administrate higher amounts of a short half-life radioisotope to the patient, as it will not be active inside the body for a long period of time (Nijran, 2017). Radioactive isotopes are also utilized for medical research to study if the function of organs is normal, also known as "functional imaging" (Baeta, 2019).

The main difference of the imaging applications of nuclear medicine with planar X-ray and CT is that the latter focus on the morphology of the patient, while nuclear medicine focuses on the physiology of the patient by assessing the biological and metabolic processes (Wheat et al., 2011).

Some of the most common radioisotopes used for diagnosis are Technetium 99 (Tc-99), which fulfills some of the most basic requirements to be used in nuclear medicine scan, such as with SPECT (Single-photon emission computed tomography) and Fluorine 18 (F-18), which is linked with the pharmaceutical fluorodeoxyglucose and is most commonly used in PET (Positron Emission Tomography) imaging.

Radioisotopes in medicine are quite advantageous compared to conventional radiation therapy and hadrontherapy. A small amount, around one-billionth of a gram, is possible to be detected (Phelan, 1968). In addition, they can be attached to various biological vectors, such as chelates and monoclonal antibodies, which directly and specifically target the cause of pathology, while sparing the healthy tissues. This function of Radio-Immuno-Therapy allows to selectively destroy cancer cells and is a really efficient way of dealing with metastatic tumours.

Therapeutic radio-pharmaceuticals exert their radiobiological action through the emission of electrically charged particles, such as α particles, β particles and Auger electrons, which deposit their energy within a limited range in tissue, ranging from a fraction of a micrometer to a few millimeters at most (Orsini, Guidoccio, and Mariani, 2019). The goal of radionuclide therapy is to cause radiobiological effect with irreversible damage to cell DNA, resulting in cell

death. The radionuclides are linked to carrier molecules capable of selectively transporting the radiotracers to the target tissues (in the majority of cases it is used for oncological purpose).

Some of the most common radioisotopes used for therapeutic treatments are Iodine-131 to treat thyroid cancer and Yttrium-90 for the treatment of non-Hodgkin's lymphoma and liver cancer. Furthermore, Actinium-225 is used for targeted alpha therapy (TAT).

The main recent treatments using radio-pharmaceuticals include the treatment of malignant or benign thyroid disease, neural crest-derived tumors, neuroendocrine tumors, Non Hodgkin's lymphoma, metastatic bone disease and intraarterial therapy of liver tumors (Orsini, Guidoccio, and Mariani, 2019).

1.3.1 Production of Radioisotopes

The production routes for radioisotopes involve the use of small medical cyclotrons, nuclear reactors and larger accelerators like electron or proton linacs.

Pure isotope sources have also been produced by the Isotope Separation Online (ISOL) technique. This technique takes into advantage the combination of targets and a particle beam that irradiates these targets. The products of the interaction of the beam with the thick natural targets are separated thanks to mass spectrometry methods. The ISOL technique has constantly been developed at ISOLDE at CERN for over 40 years and it offers many different isotope beams of more than 70 chemical elements (Augusto et al., 2014).

A list of radioisotopes that are produced at CERN-ISOLDE and collected in MEDICIS can be seen in Table 2 of Ref. (Augusto et al., 2014) covering positron, Auger and conversion electron, γ emitters (for SPECT imaging) as well as alpha emitters. Some of the radioisotopes that are of interest are, for example, Tb-149, Tb-152 and Tb-155 (collected from ISOLDE and MEDICIS in 2018). Tb-149 emits both α and β + particles, so it is possible to implement it in theranostics meaning that it can be used for both diagnosis (via Positron Emission

Tomography-PET imaging) and therapy (Müller et al., 2016).

From the previous, it is obvious that the personalized treatment in nuclear medicine makes use of theranostic radioisotopes. The standard production routes for those are limited by radiochemistry techniques, which are unfortunately not able to separate between different isotopes of the same element.

1.4 MEDICIS

The CERN-MEDICIS (MEDical Isotopes Collected from ISOLDE) facility aims to produce novel radioisotopes designed for medical purposes, such as theranostic (diagnosis and therapy) applications (Augusto et al., 2014). The MEDICIS targets are irradiated in the ISOLDE facility hall, taking advantage of the beam which transverses through the ISOLDE target without interacting. The beam is coming from the Proton Synchrotron (PS) Booster with an energy 1.4 GeV and was previously directly stopped in the ISOLDE beam dump. Figure 1.1 shows CERN's accelerator network, where the MEDICIS as well as the ISOLDE facility can be observed to be connected to the PS Booster. However, because of the extended periods of shutdown of the accelerator due to maintenance and upgrade purposes, a second production route for the radioisotopes was foreseen. This alternative production method depends on external facilities, that provide the irradiated targets by making use of cyclotrons or nuclear reactors.

1.4.1 MEDICIS operation

The main steps of the MEDICIS operation from target irradiation to isotope extraction are presented in the following paragraphs and the process can be seen in Figure 1.2.

First step is the target delivery to the MEDICIS area. This transfer is done by the KUKA robotic arm, that puts the target in the Rail Conveyor System (RCS), or so called MONTRAC. The next step is the transportation to the ISOLDE target area and its located

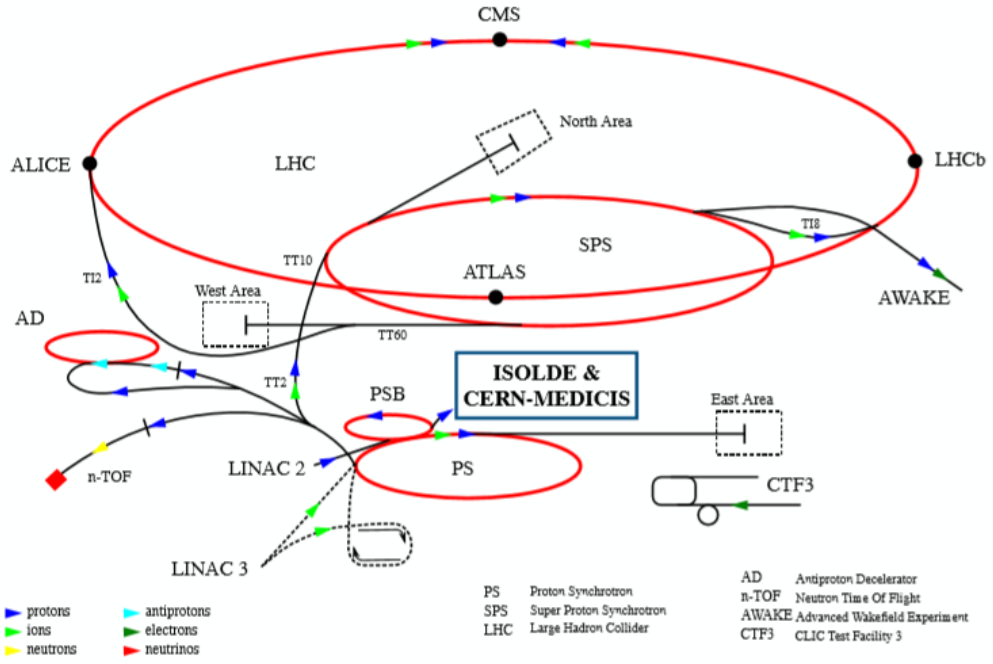

Figure 1.1 CERN accelerator network. Adapted from Ref. (CERN, 2011)

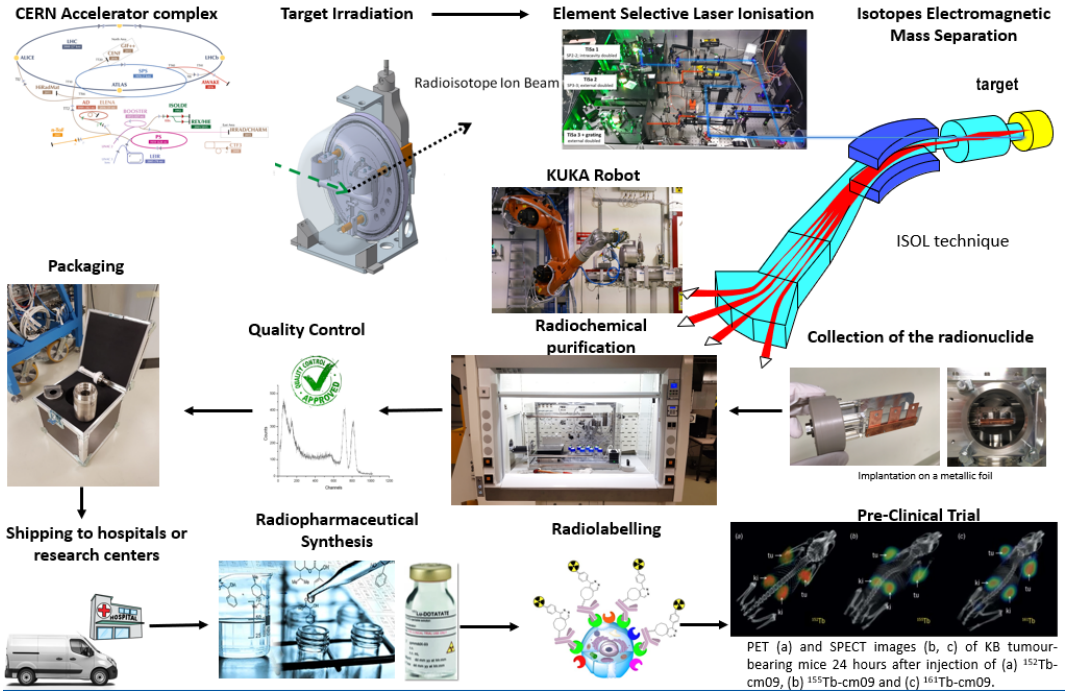

Figure 1.2 Schematic overview of the steps of MEDICIS operation. Adapted from Ref. (CERN-MEDICIS, 2019)

between the target of ISOLDE and its beam dump. Then, the irradiation of the target is executed at the target area, where the MEDICIS target is placed between the ISOLDE target and the beam dump. Portable radiation detectors check the radiation levels. The most probable ways of nuclear reaction, in order to produce radioisotopes, at the energy 1.4 GeV proton beam, are fission and spallation. About 85% of the incoming 1.4 GeV proton beam passes through the ISOLDE target without interaction and reaches the MEDICIS target. The irradiation occurs until the isotope of interest is at saturation. Therefore, the irradiation time will strongly depend on the radionuclide's half-life and the operation schedule. Afterwards, the MEDICIS target is transferred to the MEDICIS laboratory by the RCS and placed in the decay point. Again, the radiation monitors check the radiation levels (Palenzuela, 2019).

The period the target remains at the decay point depends on the irradiation time, the target material, the proton beam intensity and the half-life of the radioisotope. When the dose rate falls below 1 Sv/h (measured at distance of 26cm) the target can be removed from the decay point and placed thanks to the KUKA robotic arm in the MEDICIS front-end. From the plethora of different isotopes created in the target due to the irradiation, the desired medical radioisotopes have to be extracted with as high purity and efficiency as possible. For that reason, the resonance ionization laser ion source (RILIS) technology coupled with a conventional electromagnetic separating unit is employed (Gadelshina et al., 2019).

To increase the radioisotope yield and to offer highly pure product, the laser ion source MELISSA (MEDICIS Laser Ion Source Setup) was built. It began its function in 2019 at the MEDICIS facility. Its performance was investigated for the planned production of Tb radioisotopes which, as it was aforementioned, have great importance for medical applications.

However, there are some cases where the radioisotopes have similar ionisation schemes (for instance in the case of Tb-155 and Gd-155). Therefore, the beam current measured is a mixture of these radioisotopes and it is not possible to assess the activity of the desired

radioisotope collected on the sample. This is one of the reasons why it is crucial to control the collected activity of the radioisotope of interest with an on-line detection system like a γ spectrometer.

The characterization of the Cadmium Zinc Telluride (CZT) detector will allow to get an on-line monitoring of the accumulated activity during collection. With this detector it will be possible to adapt different parameters (tuning of the laser or adjusting the temperature of the target) during collection to maximize the activity collected.

After the collection of the radioisotope a γ-spectrometry team is checking whether the sample is complying with ADR (Accord européen relatif au transport international des marchandises dangereuses par route) rules for shipping radioactive packages. Each batch is analyzed by γ-ray spectroscopy to determine the presence of any possible contaminant collected with the radioisotope of medical interest. This is performed by the shipping service in order to control the activity of the radioisotope before the transfer.

In the near future, radiochemistry will be performed in MEDICIS. At the end of the collection, MEDICIS will be also able to offer a good estimation of the activity of the collected radioisotope by using the CZT detector, which will be characterized in detail in the following sections of this thesis.

Chapter Two

Theoretical Background

2.1 Gamma-ray Spectrometry

The majority of the radioisotopes emit γ-rays, with a variety of energies and intensities. The γ-ray energy spectrum is acquired thanks to spectrometry systems that are capable of detecting and analysing the γ-ray emissions.

Gamma spectrometry detectors need to be consisted of materials that are able to interact with incoming γ-rays. In the appropriate conversion medium of the detectors three mechanisms are possible: the photoelectric effect, the Compton effect and the pair production (Knoll, 2000), as it can be seen from Figure 2.1. From Figure 2.1, it can be seen that low energy photons interact mostly via the photoelectric effect, while the intermediate and high energy photons interact through Compton and pair production effects respectively. These interaction mechanisms are described in detail in the following sections.

2.1.1 Photoelectric effect

In the photoelectric effect the incident photon interacts with the atom of the absorber material. The incident photon gets absorbed and at the same time an electron is emitted from one of the bound shells. The emitted electron is also known as photoelectron (Knoll, 2000). An empty space is created due to the ejection of the photoelectron but it is filled very quickly, in

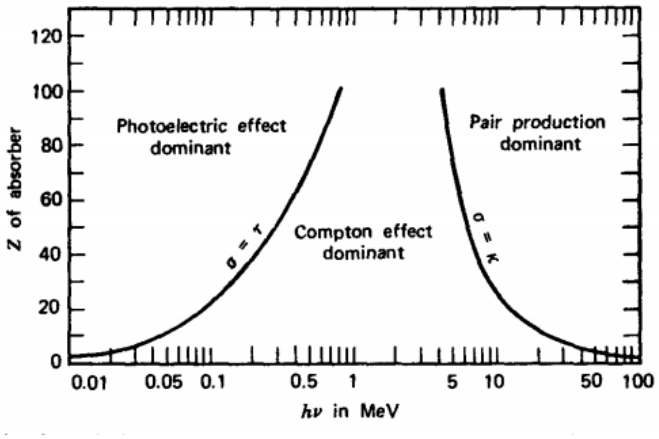

Figure 2.1 The three mechanisms of interaction of γ-ray photons with matter as a function of energy and different atomic number of absorber. Adapted from Ref. (Knoll, 2000)

an order of time of picoseconds, either by a free electron or by electrons from other shells of the atom. The latter method is the mechanism behind the creation of characteristic X-rays. The photoelectric process is the dominant way of interaction for photons belonging to the low energy domain. Furthermore, it is also prevalent for high atomic number (Z) materials. The photoelectric effect is the phenomenon that is more of interest for this thesis, since it is the main effect that is being taken advantage of, inside a semiconductor, which is going to be analysed in more detail in next sections.

The Auger decay is sometimes another way of de-excitation that can occur instead of the characteristic X-ray emission. There are two possible Auger processes. The normal Auger process occurs when the intermediate state is a core ionized state. When an electron from the outer shells fills the hole, the core electron is ejected and an Auger electron is emitted. On the other hand, in the resonant Auger process the intermediate state is core-excited. In this case, the 1s electron is excited to an unoccupied orbital in the valence region and an Auger electron is ejected. Hence, the system is simply ionized.

In Figure 2.2, the photoeletrical cross section in the case of the interaction in CZT as a function of the energy of the γ-ray is presented (AMPTEK, 2001). Figure 2.2 was computed

using the "Photcoeff software package". As it can be seen, CdZnTe has higher photoelectric attenuation coefficient than Germanium and Silicon.

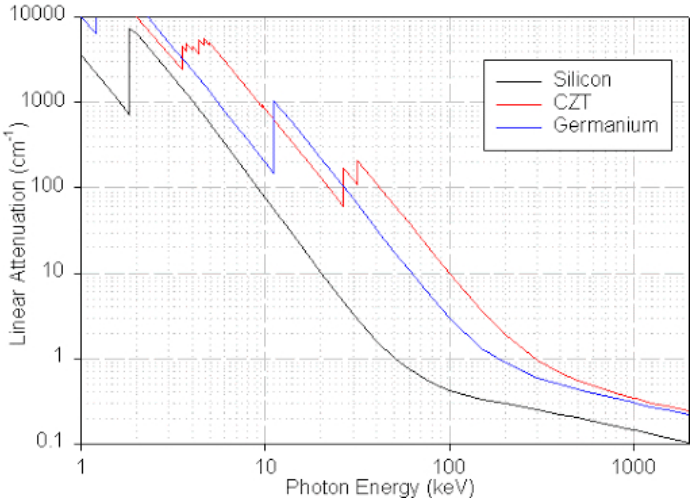

Figure 2.2 Linear attenuation coefficients for Photoelectric Effect in CdZnTe, Silicon and Germanium. Adapted from Ref. (AMPTEK, 2001)

2.1.2 Compton effect

In the Compton scattering the incident photon gives only part of its energy to the electron (also known as recoil electron) of the absorber atom.

Classical electromagnetic theory is not able to describe the inelastic component that was observed when electromagnetic radiation was scattered by charged particles. Compton (Compton, 1923) and Debye (Debye, 1915) independently formulated the relationship between the wavelength and the scattering angle of radiation that was impinging on not bound, stationary electrons (Bergstrom and Pratt, July 1997). The scattered photon energy $E_{\gamma'}$ is given by the following formula:

$$E_{\gamma'} = \frac{E_\gamma}{1 + \frac{E_\gamma}{(m_e c^2)(1-cos\theta)}} \tag{2.1}$$

where θ is the angle from the incoming photon's path which has energy E_γ. The new photon γ' is emitted after the collision of the initial photon γ with the electron of the atom.

Also, m_e stands for the electron mass and c stands for the speed of light.

2.1.3 Pair Production

In the pair production mechanism the incident γ-ray photon produces a pair of an electron and positron. For this purpose, the incident γ-ray photon has to exceed at least twice the rest-mass of an electron which is equal to 1.022 MeV. For the produced positron usually the case is that it will annihilate with an electron in the detector material. Thus, two γ-ray photons of 0.511 MeV each will be created (Buchtela, 2019). The produced electron on the other hand will travel through matter until it loses entirely its kinetic energy via ionization, electron excitation, or bremsstrahlung radiation (L'Annunziata, 2012).

2.1.4 Gamma-ray Spectrometers

Gamma-ray spectrometers are instruments used in a variety of not only scientific but also industrial applications. Only the fast electrons generated due to the aforementioned interactions can provide the characteristics of the impinging γ-ray photons. Through these three mechanisms, the energy of the γ-ray is absorbed and converted into a voltage signal. This voltage is proportional to the energy of the incident γ-ray photon.

The most advantageous mechanism out of the three in terms of accuracy in the energy measurements is the photoelectric effect due to the fact that the photon energy is totally absorbed by the atom. On the other hand, Compton interaction and pair production are not that suitable for energy measurements because some of the energy might escape from the detector. This can lead to energy spectra with overlapping peaks of smaller energy. However, this can be resolved with larger detectors that ensure the total absorption of the γ-ray photon energy.

2.1.5 Semiconductors

The incident γ-ray photons create charge carriers (electrons and holes) in their path. The semiconductor detector's working principle is to detect these charge carriers. A charge carrier is a charged particle able to move freely in the medium. In a conducting medium, an electric field can create an electric current because it obliges these carriers to move in the same direction. Electrons and holes constitute the charge carriers in semiconductors (Myers, 1997).

The band theory in solids determines the electrical conductance behavior of crystals. So according to the energy gap between the valence and the conduction band it is possible to separate between the conductors, insulators and semiconductors, as it can be seen from Figure 2.3. The conduction band can be populated with electrons that go from the valence band to the conduction band if their energy is sufficient. This can cause the increased electrical conductivity of the semiconductor. The number of electrons that move from the valence to the conduction band, hence the electrical conductivity, depend on the temperature. For higher temperature more electrons transfer between the energy bands and thus the electrical conductivity is higher (Huebener, 2016).

In Figure 2.3, the scheme of the bands in a solid can be seen. According to the energy gap between the conduction and the valence bands there are three different categories of solids: the insulators, the semiconductors and metals. Briefly, when the valence and conduction bands overlap the solid is a metal. This overlapping of bands leads to the high conductivity of metals. When the band gap is sufficiently small, meaning that the electrons in valence band can "jump" to the conduction band just because of their thermal energy, the solid is identified as semiconductor. When the valence-conduction band gap is large, the solid is categorised as an insulator, which has a very low conductivity (Sadeghi, 2016).

The most common semiconductor based detectors are made of germanium or silicon. However, there are other substances, which are composed from several elements and are

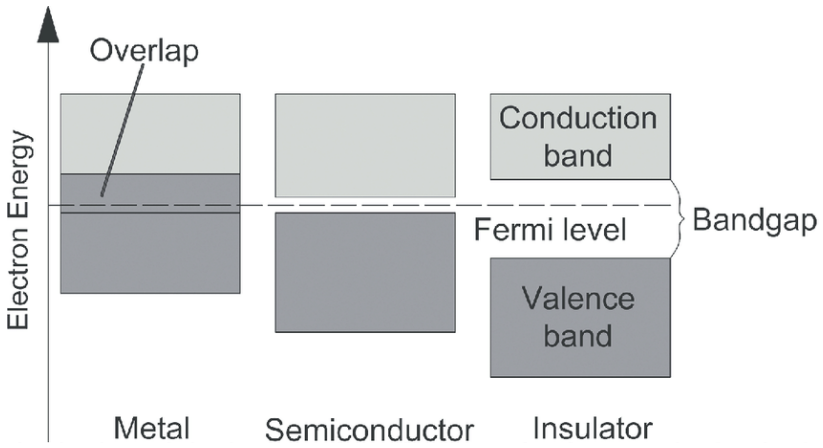

Figure 2.3 Band theory in Solids. Adapted from Ref.(Sadeghi, 2016)

highly interesting for technical applications because of their semiconductor properties.

For instance, the III–V semiconductors (such as InP, InAs, GaAs, GaN, and InSb, which include compounds of elements from the third and fifth group of the Periodic Table) have shown intriguing electronic properties, such as low excitation energy. Electrons and holes of such semiconductors have higher mobility than in germanium and silicon. Another advantage is that the energy gap of the valence and conduction band is bigger that in germanium and silicon. Thus, applications that need quick response of the charge carriers are feasible with these semiconductors (Liu, Ma, and Ye, 2018).

Compound semiconductors include also compounds of elements from the second and the sixth group of the Periodic Table, which are referred to as "II–VI semiconductors". CdZnTe detectors belong to the II-VI semiconductors and allow high resolution with the advantage of operation in room temperatures, as it will be further explained in the following section.

Chapter Three

The principles of operation of a CZT detector

Cadmium Zinc Telluride CZT (written CdZnTe as well) is a semiconductor that can convert X-rays or γ-ray photons into electrons and holes while operating at room temperature. The gap between the valence and conduction bands is 1.44 eV, which reduces the leakage current and offers high resistivity as well as low background density of free carriers at room temperature (Zanio, 1978), (Schlesinger et al., 2001). Cadmium has an atomic number equal to 48, zinc has an atomic number equal to 30, while telluride's atomic number is 52, meaning that these detectors have high photon absorption efficients. This is a great example of why CZT detectors are more advantageous than common germanium or silicon semiconductor based detectors since, for instance, 2 mm of cadmium telluride is equivalent to 10 mm of germanium in respect to γ-ray photon absorption (Gilmore, 2008). One of the main advantages over mainstream semiconductor materials like silicon and germanium are the high radiation stopping power of the CZT detectors (Awadalla, 2017).

This combination of high resolution, ability to work at room temperature without the need for cooling (contrary to the Hyperpure Germanium detectors that need constant cooling in order to operate) and large count rate capability makes CZT detectors ideal for a variety of applications, such as Medical, Industrial and Homeland Security (Kromek, 2020). Recent

studies have shown possible applications of the CZT detector for quality control of positron emission tomography radiopharmaceuticals (Vichi et al., 2016a) and for nondestructive activation assessment of a cyclotron bunker (Vichi et al., 2016b).

Nowadays, cadmium zinc telluride and cadmium telluride (CdTe) are commercially the most common II–VI compound semiconductor systems for X-ray and γ-ray radiation detection (Awadalla, 2017).

CZT detectors consist of very thin metalized electrodes placed on the surfaces of the crystal. The electrical bias on these electrodes creates a electrical potential difference across the detector. Once the ionizing radiation interacts with the CZT detector, a big amount of charged carriers are generated. The number of pairs of electrons and holes is proportional to the energy of the incoming radiation. These charged carriers are collected by the oppositely charged electrodes. The pulse is then sent to the preamplifier, to amplify the voltage pulse so that its height to be proportional to the energy of the incident γ-ray. Afterwards, this signal is sent to the shaping amplifier to create a Gaussian shaped and amplified pulse. The next step is the Pulse Height Analysis with Multi-Channel Analyzer (MCA) in order to obtain the characteristic spectrum for the incident γ-rays. A common practice is to couple the cadmium zinc telluride CZT-based detector to an ASIC (application specific integrated circuit) in order to minimize the size and expense of the readout electronics (Kromek, 2020).

In this thesis, different types of CZT detectors will be characterized and compared to each other. In particular, the models GR-1 (purchased from CERN), GR-05 (available by KU Leuven), SDP500S, LAB Coplanar Grid and SPEAR (purchased by Complutense University of Madrid) were analysed thoroughly. More details are presented in the next sections.

3.1 Characteristics of GR-1 CZT detector

According to the manufacturer the GR-1 CZT detector, as it can be seen in Figure 3.1, has the following characteristics:

- Detector's Crystal size: 10 mm x 10 mm x 10 mm co-planar
- Energy range: 30 keV to 3 MeV
- Resolution: <2.5% @ 662 keV using Cs-137.
- Electronic noise: <10 keV FWHM
- Maximum throughput: 30000 counts/s
- Number of channels: 4096 (12bit)
- Differential non-linearity: $<\pm 1\%$
- Weight: 60 g
- Size: 63 mm x 25 mm x 25 mm
- Power consumption: 250 mW

According to the User Guide from KROMEK, this model can be used coupled with K-Spect and MultiSpect Analysis software, which run on a Windows-based Computer.

The γ-ray spectrometer is able to connect with the computer through a USB port. The casing of the detector includes, apart from the CZT crystal, a preamplifier, a shaping amplifier, a baseline restorer, a pulse height digitizer, and a HV supply. The signals from the CZT detector are processed and digitized inside the GR1 and the information is transferred to the computer. The K-Spect software is able to acquire the spectrum, display and analyse the data.

3.2 Detector Operation

The CZT detector's operation is quite simplified. The first step is to connect the detector with the computer via the USB cable. Then Multispect Software identifies the detector and the setup is ready for data acquisition and analysis.

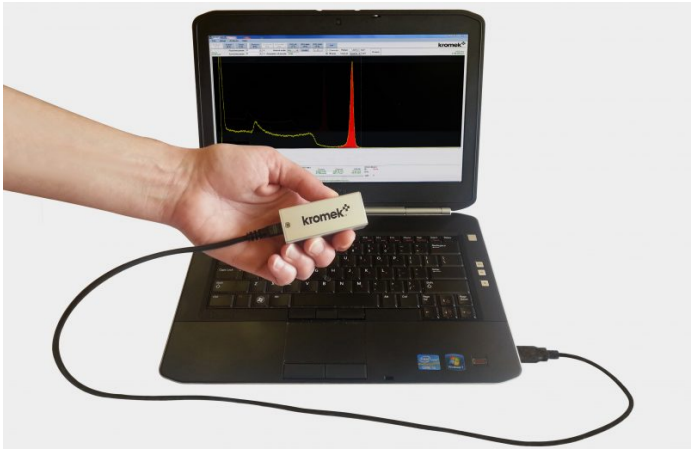

Figure 3.1 CZT GR-1 γ-ray Spectrometer. Adapted from Ref. (Kromek, 2020)

Briefly, when the incident γ-ray photon interacts with the CZT crystal it produces negatively charged electrons and positively charged holes which move and are collected by the respectively opposite charged electrodes leading to a charge pulse. Then, the preamplifier detects this charge pulse and creates a voltage pulse with height proportional to the energy deposited by the γ-ray photon. Afterwards, the voltage pulse is provided to the shaping amplifier, which is responsible for converting the signal into a Gaussian pulse while amplifying it. Finally, the signal is sent to Multi-Channel Analyzer (MCA) and the characteristic spectrum for the incoming γ-ray photons is produced.

To ensure the best performance of the CZT detector it is advised by the manufacturer to allow it to stabilize for at least 5 min before starting the actual acquisition. When it is stabilized, the user can click the appropriate button in the software and acquire the spectrum. Thereafter, the full spectrum is obtained that consists of 4096 channels (equal to approximately 3 MeV). The software allows to set a Lower Level Discriminator (LLD) not lower than channel 32, in order to cut the low-energy part of the spectrum or the noise peak.

3.2.1 Detector Resolution

The resolution of the detector is a crucial characteristic of γ spectroscopic detectors as it can affect the width of the peaks. The ability to separate two adjacent peaks from each other

is a result of the high resolution of the detector. The peaks have usually a Gaussian shape, where the horizontal position indicates the γ ray's energy and the area under them shows the number of counts (Knoll, 2000).

The most common parameter to express detector resolution is Full Width at Half Maximum (FWHM). This is the width of the γ-ray peak at half of the highest point on the peak distribution (Waterstram-Rich and Christian, 2013).

The relative energy resolution corresponds to:

$$Resolution = \frac{FWHM_{peak}}{\mu_{peak}} \times 100 \tag{3.1}$$

where $FWHM_{peak}$ is the full width half maximum of the peak and μ_{peak} is the channel number of the centroid of the peak (CAEN, 2018).

3.2.2 Detector Efficiency

The absolute photopeak efficiency of a detector represents the ratio between the number of hits detected in the full energy peak(s) and the number of γ-ray photons actually emitted by the source. For a given detector and a given energy γ, the detection efficiency is dependent on the source activity, the detector and source's geometry and the distance separating the source from the detector (Duchemin, 2015). The detection efficiency, ϵ for a given geometry, is defined by the following relation:

$$\epsilon(E) = \frac{N}{I(E) \times t \times A} \tag{3.2}$$

where N is the number of counts, $I(E)$ is the intensity of the γ-ray photons at a given energy, t is the live time in seconds and A is the Activity in Becquerels of the source on the day of the measurement. The intensities of the γ-ray photons for all the different radioactive sources were extracted from Ref. (*Laboratoire National Henri Becquerel* last updated 2017-03-03).

3.2.3 Calculation of Efficiency Uncertainty

In statistics, quadratic error propagation is the effect of variables' errors on the error of a function that includes these variables. In this case, the uncertainties from the variables of activity, time, counts and probability of emission are affecting the uncertainty of the efficiency. This uncertainty can be calculated using Equation 3.3 from Ref. (Taylor, 1997):

$$\frac{\Delta\epsilon}{\epsilon} = \sqrt{(\frac{\Delta N}{N})^2 + (\frac{\Delta I}{I})^2 + (\frac{\Delta t}{t})^2 + (\frac{\Delta A}{A})^2} \tag{3.3}$$

3.2.4 Dead space

One of the main advantages of the CZT detector is its size. The fact that it is a direct-conversion detector means that it has limited dead space. Therefore, the volume that needs to be shielded is quite small for a CZT-based detector, henceforth the final configuration is light (*CZT Technology: Fundamentals and Applications* 2011).

3.3 Conclusions

From the above, it is clear that Cadmium Zink Telluride (CZT) detectors should be able to provide good energy resolution, good efficiency and high count rate capability at room temperature without the need of cooling. Thus, different models of CZT detectors were thoroughly characterized and compared in this thesis to ensure that their capabilities are suitable for MEDICIS operation. The analysis of the different types of CZT detectors is presented in the next chapters.

Chapter Four

Comparison between CZT detectors GR-1 and GR-05

In this chapter the comparison of the two different CZT detectors from KROMEK are presented. These two models of the CZT detector (GR-1 and GR-05) were compared in terms of FWHM and detection efficiency. The values of FWHM were cross checked with those given by the manufacturer (KROMEK).

This analysis is important in order to choose which of the models is more suitable for the different steps of MEDICIS operation.

4.1 Manufacturer Specifications

It needs to be noted that the difference between the GR-1 and GR-05 CZT detectors is the size of the crystal. In the case of GR-1 the detector consists of a cubic 1 cm^3 CdZnTe crystal with all the electronics enclosed in a 25 $\times$25 $\times$ 63 mm containment. On the other hand, in the case of GR-05 the device consists of a cubic 0.125 cm^3 CdZnTe crystal.

According to the manufacturer, the specifications of the semiconductor detector GR-05 and GR-1 are presented in Tables 4.1 and 4.2.

Table 4.1 GR-1 SPECIFICATIONS

Parameter	Specification	Actual
Channel no @ 662 keV (Cs-137)	880 ±1%	877.9
Channel no @ 59.5 keV (Am-241)	80 ±10%	77.6
Energy resolution @ 662 keV (Cs-137) at 21^oC	FWHM <2.5%	2.3%
Energy resolution @ 59.5 keV (Am-241)	FWHM <12 keV	6.6 keV

Table 4.2 GR-05 SPECIFICATIONS

Parameter	Specification	Actual
Channel no @ 662 keV (Cs-137)	880 ±1%	879.5
Channel no @ 59.5 keV (Am-241)	80 ±10%	78.2
Energy resolution @ 662 keV (Cs-137) at 21^oC	FWHM <2.5 %	2.0 %
Energy resolution @ 59.5 keV (Am-241)	FWHM <12 keV	6.1 keV

4.2 Experimental set-up

The experimental set-up as shown in Figures 4.2 and 4.3 was structured such as to reproduce the real conditions of the measurement on the collection chamber in the MEDICIS laboratory. This collection chamber contains a sample holder for three collection foils. The position of the foils is selected by a robotic arm which is able to maneuver perpendicularly to the radioactive ion beam. The collection foils are made with gold and an one-sided Zinc coating performed by the CERN EP-DT group. In Figure 4.1, the collection chamber and the collection window as well as the detector in red are presented. The support of the detector has the convenient feature of adjustable height.

The detectors GR-05 and GR-1 were placed 1 cm away from the center of the window of the collection chamber while the source is on the other side, 7 cm away from the center of the collection window and behind the gold collection foil, as depicted in Figures 4.2 and 4.3.

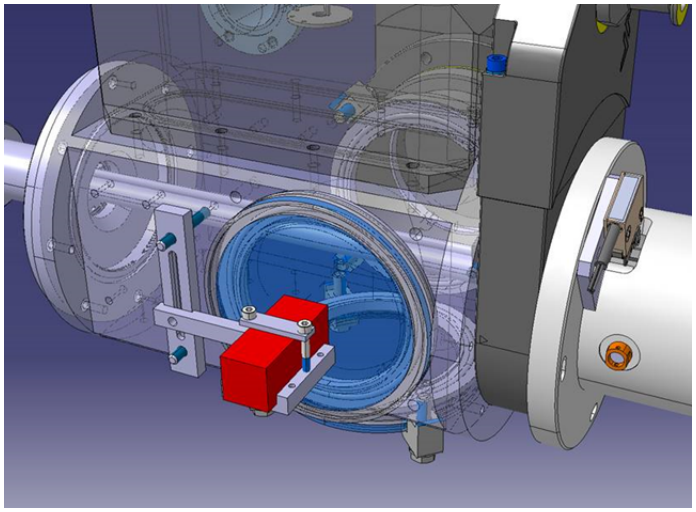

Figure 4.1 Collection chamber and the collection window as well as the detector in red made with CAO 3D CATIA software. Courtesy of Stefano Marzari. Support with adjustable height built by Ermanno Barbero.

Hence, both of the detectors had the same experimental configuration in order to have directly comparable efficiency values.

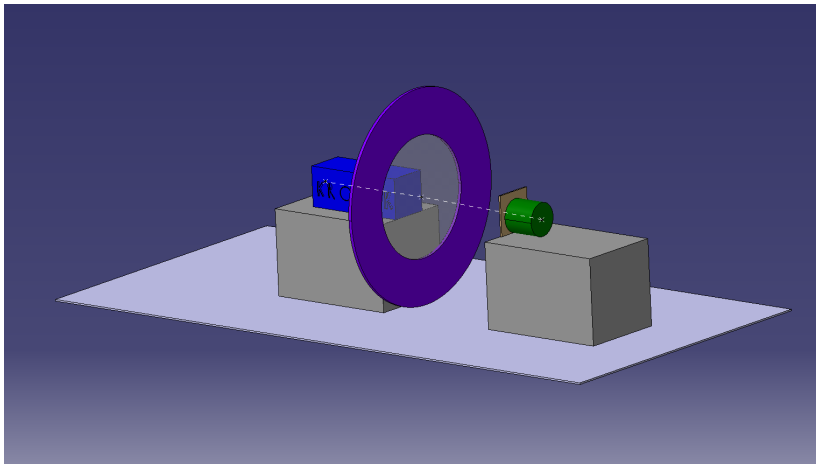

Figure 4.2 Overview of the experimental setup made in CAO 3D CATIA software. Courtesy of Vasilis Samothrakis.

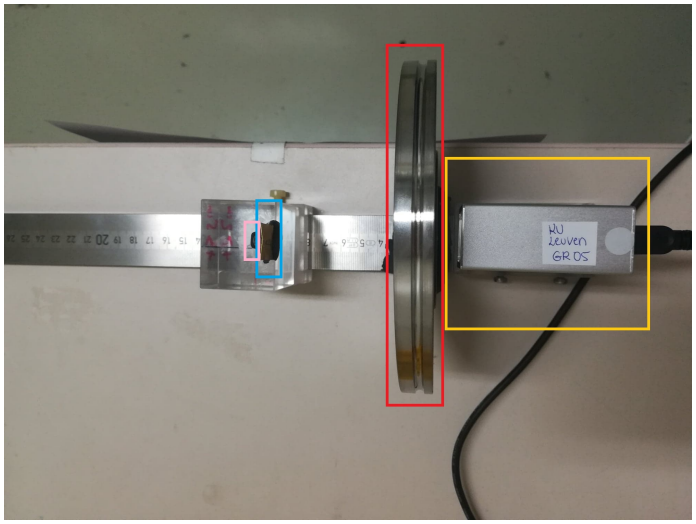

Figure 4.3 Picture of the experimental setup seen from above. Within the Pink Square is the source, within the blue square is the gold foil, within the Red Square is the Window from the collection chamber and within the Yellow Square is the GR-05 CZT detector.

4.2.1 Sources

For the efficiency calibration an Eu-152 and a Cs-137 source were used (see in table 4.3). The intensities of the γ-ray photons for all the different radioactive sources were extracted from Ref. (Laboratoire National Henri Bequerel), which is based on the ENDF (Evaluated Nuclear Data File) library from IAEA.

Table 4.3 Sources

Source	**Activity (Bq)**	**Uncertainty**	**Half-life (years)**	**γ emissions (keV)**	**Intensity (%)**
Am-241	3.7 E08	30 %	432.2	59.5	35.9
Cs-137	2.9 E04	5 %	30.1	661.6	85.1
Eu-152	3.7 E04	1.7 %	13.5	121.8, 244.7, 344.3	28.6, 7.6, 26.5
Eu-152	3.7 E04	1.7 %	13.5	778.9, 964.1, 1408.0	12.9, 14.6, 21.0

The Am-241 source was utilized in order to check the dead time value of GR-05 and to check how the detector behaves with a strong radioactive source as well as compare it with the respective results of GR-1.

4.3 Results and discussions

4.3.1 Dead time analysis with an Am-241

For Am-241 with an activity of 365 MBq, as it can be seen in Table 4.3, using the same configuration GR-1 gives a dead time of 4.6% while GR-05 gives a dead time of 1.2%. This confirms the statement from the manufacturer that the GR-05 is great for use in high count environments because the higher active nuclides will not saturate the smaller crystal (Kromek, 2020).

Thus, it is safe to assume that GR-05 is better suited for the measurement of the activity during the radiochemistry steps of the MEDICIS operation because during this procedure the detector needs to be located very close to the fume hood.

4.3.2 FWHM of GR-05 and GR-1

The spectrum of Cs-137 source gained by using GR-1 detector with Multispect Software can be observed in Figure 4.4. The energy resolution for Cs-137 can be seen in Figures 4.5 and 4.6. The bright red colour in these figures signifies the area under the peak and the darker red colour the background area. The comparison between the FWHM for Cs-137 is depicted in Table 4.4. It can be observed that both detectors comply with the specifications from KROMEK, with GR-05 having a slightly better FWHM.

Table 4.4 FWHM

Source	**Type of Detector**	**FWHM according to Specification**	**Measured FWHM**	**Live Time**
Cs-137	GR-1	<16.5 keV	14.8 keV	84225.8 s
Cs-137	GR-05	<16.5 keV	11.9 keV	8027.1 s

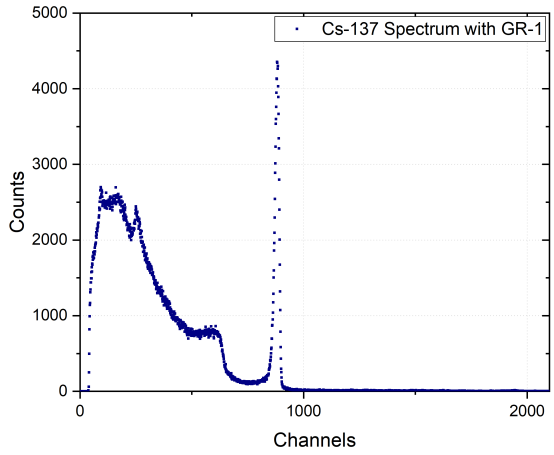

Figure 4.4 Example of Cs-137 spectrum using GR-1 detector

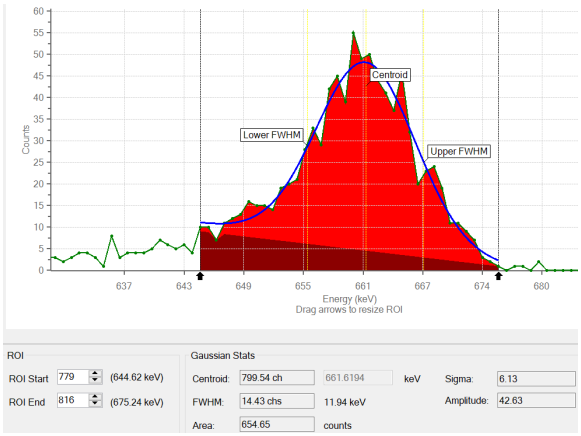

Figure 4.5 Cs-137 FWHM using GR-05 with live time: 8027.1 s

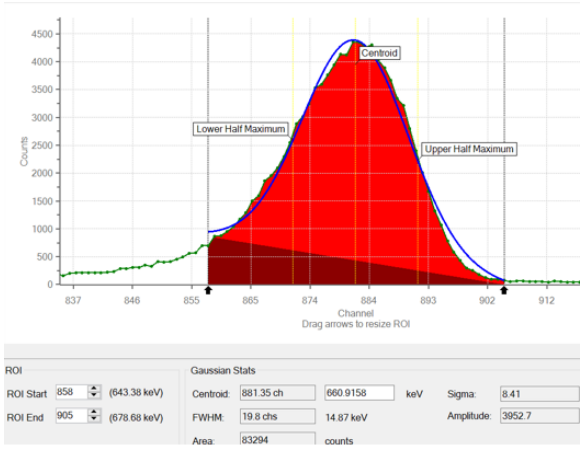

Figure 4.6 Cs-137 FWHM using GR-1 with live time: 84225.8 s

Figure 4.7 FWHM of Cs-137 gained by Multispect Software for GR-05 and GR-1 CZT detectors

4.3.3 Efficiency curves comparisons using Eu-152 and Cs-137 sources

The efficiency curves between GR-1 and GR-05 are compared for the sources Eu-152 and Cs-137 with the same experimental configuration, using Multispect Software from KROMEK. It is obvious from Figure 4.8a that the efficiencies of GR-1 detector are higher than the ones of the GR-05 detector, which is consistent with the fact that GR-05 has a smaller effective area because of the smaller crystal. The error bars represent the uncertainty that is calculated

with the Multispect software and their values can be seen in Table 4.5. For GR-05 the uncertainty of the efficiency range from 0.7% to 7.2% and for GR-1 it ranges from 0.3% to 1.9%. The same plot but in semilog form is depicted in Figure 4.8b.

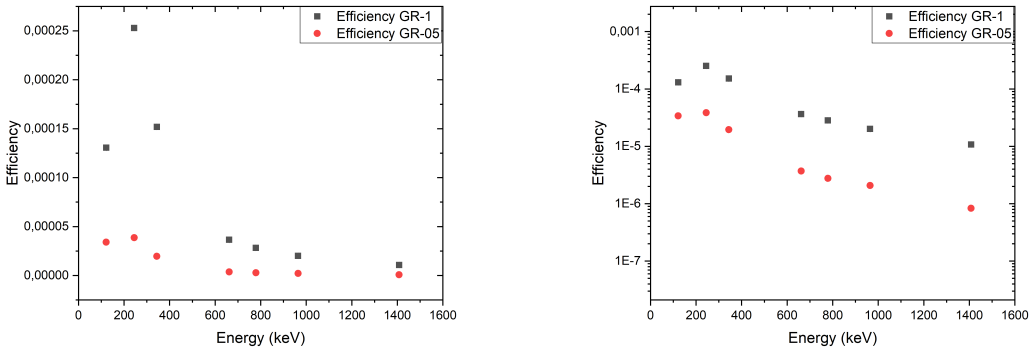

(a) Efficiencies of GR-05 and GR-1 CZT detectors

(b) Efficiencies of GR-05 and GR-1 CZT detectors in semilog

Figure 4.8 Comparison of the efficiencies from the two different models of CZT detectors

The values of the efficiencies with their uncertainties are presented at certain energies for the Eu-152 and Cs-137 sources in Table 4.5 using Multispect Software. The ratio between the efficiency values and the corresponding uncertainty is presented in Table 4.5 and plotted in Figure 4.9.

Table 4.5 Efficiency from Multispect for Eu-152 and Cs-137

Energy	Efficiency GR-05	Uncertainty	Efficiency GR-1	Uncertainty	Ratio	Uncertainty
121.8	3.41 E-05	0.02 E-05	1.31 E-04	0.01 E-04	3.83	0.03
244.7	3.86 E-05	0.06 E-05	2.53 E-04	0.02 E-04	6.55	0.11
344.3	1.96 E-05	0.02 E-05	1.52 E-04	0.01 E-04	7.76	0.07
661.6	3.71 E-06	0.19 E-06	3.65 E-05	0.02 E-05	9.82	0.76
778.9	2.76 E-06	0.19 E-06	2.83 E-05	0.05 E-05	10.25	0.66
964.1	2.07 E-06	0.14 E-06	2.01 E-05	0.03 E-05	9.70	0.82
1408.80	8.31 E-07	0.51 E-07	1.07 E-05	0.02 E-05	12.94	0.52

As it can be seen from Figure 4.9, the ratio between the efficiency values of GR-1 and

GR-05 detectors is increasing logarithmically. The phenomenological fit of the semilog plot gives an equation of

$$y = 3.3484 \ln x - 12.076 \tag{4.1}$$

Thus, the ratio is increasing from 4, since the crystal of the GR-05 model is 1/2 of the GR-1 model in each dimension, to above 12. Therefore the ratio exceeds the theoretically expected value of 8 that would be derived from a pure volume effect.

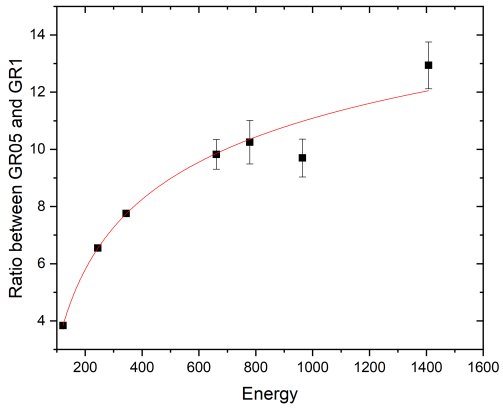

Figure 4.9 Ratio between the efficiency values of the GR-05 and GR-1 models as a function of the γ-ray emission energies and logarithmic fit depicted with the red line.

Since the live time between the two measurements was comparable for the Eu-152 source (Live time for GR-1: 258988.3 sec and Live time for GR-05: 245633.4 sec), it was possible to overlap the two spectra acquired from GR-1 and GR-05, as it can be seen in Figure 4.10. From this Figure, it is possible to see that the GR-1 detector is able to detect more counts. Therefore, it has better efficiency than the GR-05 model for the same geometry configuration and live time.

The values shown on the bottom side of Figure 4.10 correspond to the ones from the spectra acquired from the GR-1 detector.

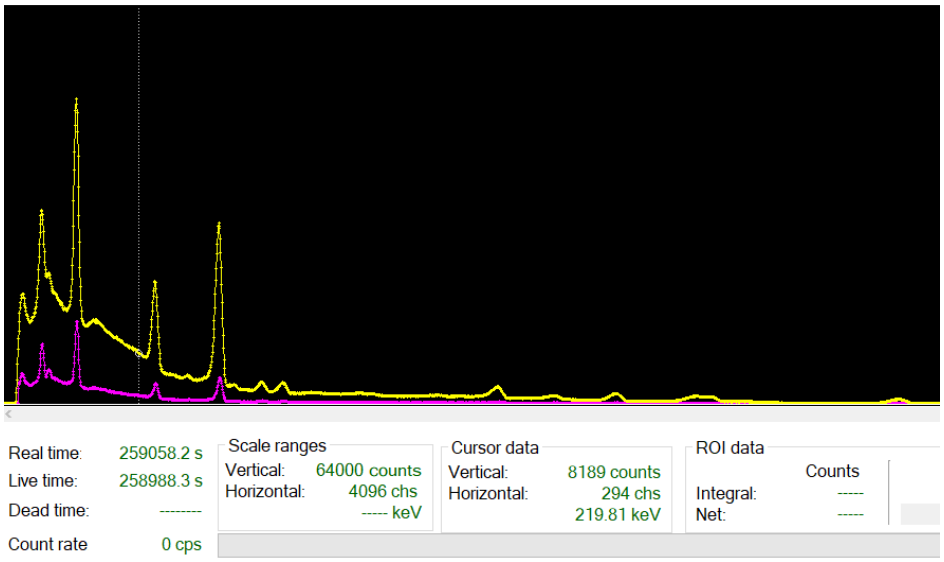

Figure 4.10 Comparison of the Spectra of the two different models. GR-05 is depicted with the purple line while GR-1 is depicted with the yellow line.

4.4 Conclusions

Resulting from the analysis above, it is safe to conclude that the GR-05 model is better suited for radiochemistry steps of the MEDICIS operation for which the detector will need to be almost in contact with the radioactive source. As it was shown, the GR-05 model is more advantageous than the GR-1 model in terms of minimizing the dead time.

On the contrary, the GR-1 model is chosen to be used in the collection chamber of the MEDICIS operation, which is located further from the radioactive source. In the following sections of the thesis the characterization of this detector is presented in order to select the best geometry configuration to find the efficiency curve that is reproducing the real case scenario during a collection at MEDICIS.

Chapter Five

Characterisation of GR-1 detector

For the characterization of the detector, the energy calibration of the detector is conducted, a background spectrum is acquired and the detection efficiency is determined.

The detection efficiency was calculated for different certified sources (and thus, different energies) using a variety of methods (Multispect Software, Fitzpeaks software) for the fitting of the γ-ray spectrum and SATLAS software as well as the Cubic Spline method from ORIGIN for the fit of the efficiency curve.

More details about the methodology and the data analysis are presented in the following sections.

5.1 Experimental Setup configuration

The initial configuration of the experimental setup consisted of the detector GR-1 one centimeter away from the window of the collection chamber, which in turn was situated 7cm away from the source. The source is behind a golden foil, which is used for the collections. The detector the window and the source are aligned to the center of the window of the collection chamber. This experimental setup was configured in such a way such as to recreate the real conditions of the activity measurement at the collection foils inside the MEDICIS facility, using the GR-1 detector.

In this configuration different sources were placed behind the golden collection foil (Co-60, Am-241, Cs-137, Ba-133, Eu-152). All of the presented sources were used for the efficiency calibration except from Am-241 with activity of 3.66 $\times 10^8$ Bq, which was used to test the dead time of the two detector models (GR-1 and GR-05), as presented in chapter 4. The activities of the sources, their uncertainties, the γ-ray emissions and the intensities of these emissions with the uncertainties in parentheses are depicted in Table 5.1. The values of the γ-ray emissions and their uncertainties were extracted from Ref. (Laboratoire National Henri Bequerel).

5.1.1 Background Measurement

The subtraction of the background peaks from the actual γ-ray peaks in the spectra is very important. Usually this is done by subtracting the complete background spectrum from the acquired spectrum, that was normalised to the measurement time. The resulting spectrum can be then analysed.

For the Multispect Software the aforementioned procedure is not necessary since the program itself subtracts the background. The user can determine the background subtraction by defining the "upper" and "lower" window controls under the display of the peak as shown in Figure 5.1.

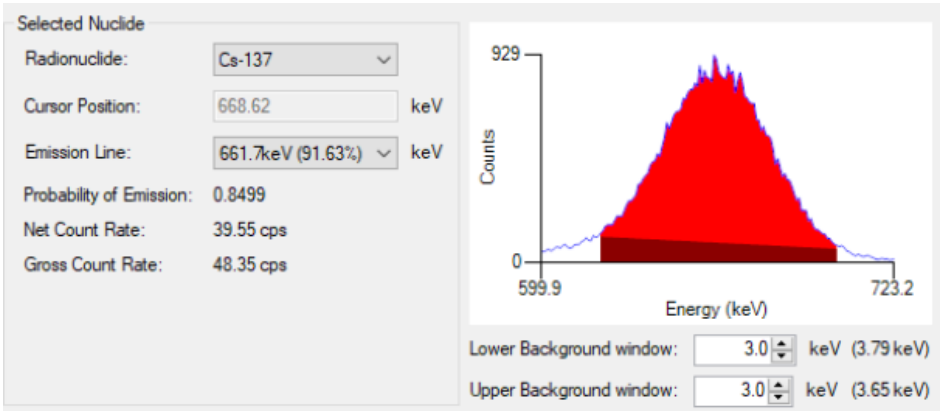

Figure 5.1 Example of background adjustment in Multispect Software for Cs-137

Table 5.1 Sources

Source	**Activity (Bq)**	**Uncertainty (%)**	**Half-life (years)**	**Energy of γ-emissions (keV)**	**Intensity (%)**
Co-60	2.96 E04 on 12.02.2020	±3.00	5.27	1173.24, 1332.50	99.85 (3), 99.98 (6)
Ba-133	5.70 E05 on 12.02.2020	±5.00	10.51	81.00, 276.40, 302.80, 356.00, 383.90	33.31 (30), 7.13 (6), 18.31 (11), 62.05 (19), 8.94 (6)
Am-241	3.66 E08 on 27.02.2020	±30.00	432.20	59.541	35.92 (17)
Cs-137	2.96 E04 on 27.02.2020	±5.00	30.17	661.66	84.99 (20)
Eu-152	3.67 E04 on 12.02.2020	±1.70	13.54	121.78, 244.70, 344.30, 778.90, 964.08, 1408.00	28.41 (13), 7.55 (4), 26.59 (12), 12.97 (6), 14.50 (6), 20.85 (8)

5.1.2 Energy Calibration

The multichannel analyser converts the voltage caused by the energy of the detected γ-ray photon into a channel number. Thanks to the energy calibration these channel numbers are assigned to the respective γ-ray photon energy. The equation that was derived by the linear fit of the relationship between the number of channels and the energy is:

$$E = 0.750973(\pm 0.001) \times ch - 0.99(\pm 0.36) \tag{5.1}$$

where E is the energy and ch is the channel number. The R^2 of the linear fit is 0.99.

5.1.3 Efficiency Calibration

For the efficiency calibration the sources from Table 5.1 were used, except from Am-241.

For the fit of the peaks with the Gaussian shape, two different softwares were used, Multispect Software and Fitzpeaks Software. More details about these two softwares are presented in the next sections.

Multispect Analysis Software

MultiSpect Analysis is designed for KROMEK's range of radiation detectors giving easy connection and setup, and analysis functions tailored to the detectors and their applications. An example of the acquired spectrum using Multispect Software of Ba-133 is shown in Figure 5.2.

The user first has to assign the appropriate radioisotope that is being studied. Then the user can choose the energy of the γ-ray emission that corresponds to the peak of the spectrum that she/he wants to analyse. The activity of the radioactive source on the date of the calibration and its uncertainty can be inserted. The Software is able to calculate the activity on the given day of the measurement and then to provide information on the efficiency of the radioisotope for the selected energy as well as the value of its uncertainty.

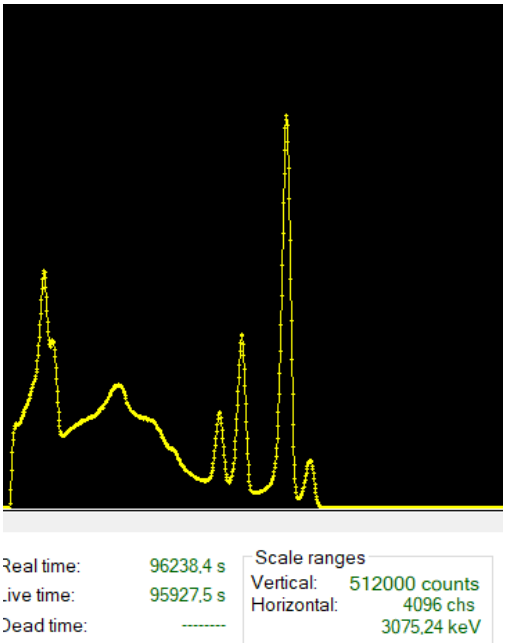

Figure 5.2 Example of Ba-133 spectrum using Multispect Software

The user can repeat the process for all the energies of the most prominent γ-ray emissions of the radioisotope and hence get all the efficiency values.

The results with this method are presented in Table 5.2.

FitzPeaks Software

FitzPeaks is a Gamma Spectroscopy Analysis software package. The algorithms that are utilized to locate and fit peaks as well as to perform the quantitative analysis are based on the paper of (Koskelo, Aarnio, and Routti, 1981) that describes the SAMPO80 program.

First, in the calibration section the user is able to calibrate for energy, peak shape and efficiency.

The peak search algorithm finds the minima in the smoothed second difference of the spectral data. The peak fitting uses a linear least squares routine, by fitting the data with a Gaussian function and an exponential tail on either the low energy side, or on both sides of the selected peak.

Table 5.2 Efficiency values calculated using Multispect Software

Source	Energy of Gamma Emission (keV)	Efficiency from Multispect	Uncertainty of Efficiency
Eu-152	121.78	1.306 E-04	0.005 E-04
Eu-152	244.69	2.529 E-04	0.016 E-04
Ba-133	276.39	1.443 E-04	0.006 E-04
Ba-133	302.85	1.639 E-04	0.002 E-04
Eu-152	344.27	1.519 E-04	0.005 E-04
Ba-133	356.01	1.243 E-04	0.001 E-04
Ba-133	383.84	8.620 E-05	0.031 E-05
Cs-137	661.65	3.647 E-05	0.021 E-05
Eu-152	778.90	2.828 E-05	0.053 E-05
Eu-152	964.07	2.011 E-05	0.039 E-05
Co-60	1173.49	1.396 E-05	0.010 E-05
Co-60	1333.22	1.130 E-05	0.008 E-05
Eu-152	1408.01	1.076 E-05	0.021 E-05

FitzPeaks Software is capable of operating in a range of modes, from a fully automated analysis through to a completely interactive mode. In the interactive modes comprehensive displays are presented, allowing the user to insert new peaks into the spectrum, change the widths of fitting regions, change the type of background continuum used, etc.

The results with this method are presented in Table 5.3. The fit of the peaks of the γ-ray spectrum were completed with the "Summation of Area" option. In Figure 5.3 the interface of FitzPeaks software is presented, while selecting the "Summation of Area" for the fit of the peak corresponding to the 344 keV gamma emission of Eu-152.

Manually assigned fit of the peaks using Multispect Software

With Multispect Software the user is able to manually assign the fit of the peaks by choosing the beginning and the end of the each peak in the spectrum and clicking on the option of performing a Gaussian fit. Hence the counts for each peak of the γ-ray spectrum are gained, as well as the Sigma of the centroid of the peak. Thus, the user is able to calculate the

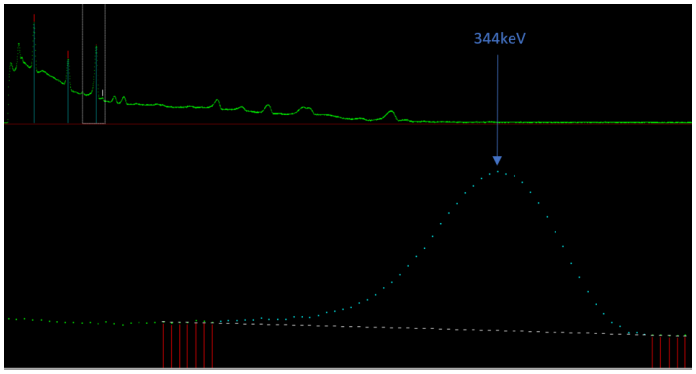

Figure 5.3 Example of fitting with FitzPeaks using "Summation of Area" option for Eu-152

Table 5.3 Efficiency values calculated using FitzPeaks Software

Source	Energy of Emission (keV)	Efficiency from FitzPeaks	Uncertainty of Efficiency
Eu-152	121.78	1.553 E-04	0.041 E-04
Eu-152	244.69	2.596 E-04	0.056 E-04
Ba-133	276.39	1.857 E-04	0.093 E-04
Ba-133	302.85	1.703 E-04	0.085 E-04
Eu-152	344.27	1.566 E-04	0.039 E-04
Ba-133	356.01	1.383 E-04	0.069 E-04
Ba-133	383.84	1.115 E-04	0.056 E-04
Cs-137	661.65	4.526 E-05	0.239 E-05
Eu-152	778.90	4.318 E-05	0.149 E-05
Eu-152	964.08	3.031 E-05	0.094 E-05
Co-60	1173.49	1.907 E-05	0.058 E-05
Co-60	1333.22	1.397 E-05	0.048 E-05
Eu-152	1408.01	1.339 E-05	0.036 E-05

efficiency as all the remaining parameters of equation 3.2 are known (intensities of the γ-ray emissions are shown in Table 5.1).

The results with this method are presented in Table 5.4.

Table 5.4 Efficiency values calculated by manually assigning the fit of the peaks with Multispect Software

Source	Energy of Emission (keV)	Efficiency from assignment	Uncertainty of Efficiency
Eu-152	121.78	1.566 E-04	0.062 E-04
Eu-152	244.69	2.702 E-04	0.073 E-04
Ba-133	276.39	1.938 E-04	0.105 E-04
Ba-133	302.85	1.694 E-04	0.091 E-04
Eu-152	344.27	1.556 E-04	0.037 E-04
Ba-133	356.01	1.274 E-04	0.067 E-04
Ba-133	383.84	1.070 E-04	0.056 E-04
Cs-137	661.65	3.864 E-05	0.199 E-05
Eu-152	778.90	4.077 E-05	0.088 E-05
Eu-152	964.07	2.902 E-05	0.134 E-05
Co-60	1173.49	1.761 E-05	0.057 E-05
Co-60	1333.22	1.332 E-05	0.043 E-05
Eu-152	1408.01	1.174 E-05	0.023 E-05

Weighted Mean Value

After calculating the efficiency values and their uncertainties with three different methods (Multispect software, Fitzpeaks software and by manually assigning the peaks using Multispect software), their weighted mean values were calculated. The results are presented in Table 5.5 together with the mean weighted values of their uncertainties.

The weighted mean values were calculated according to the formula 5.2, while the uncertainties were calculated using the following formula 5.3 multiplied with chi-squared.

$$\overline{x} = \frac{\sum_i^n x_i \times w_i}{\sum_i^n w_i} \tag{5.2}$$

$$\Delta\overline{x} = \frac{1}{\sum_i^n \frac{1}{w_i}} \tag{5.3}$$

Plotting the efficiency values vs the energy

In Figures 5.4a, 5.4b, 5.5a and 5.5b the efficiency values as a function of the energy are plotted for the methods of Multispect Software, Fitzpeaks Software and by manually assigning peaks

Table 5.5 Weighted Mean Value Efficiency and Uncertainty of the three Methods (Multispect, Fitzpeaks, manually assigned Peaks)

Source	Energy of Emission (keV)	Weighted mean value of Efficiency	Uncertainty of Efficiency
Eu-152	121.78	1.311 E-04	0.050 E-04
Eu-152	244.69	2.541 E-04	0.054 E-04
Ba-133	276.39	1.445 E-04	0.041 E-04
Ba-133	302.85	1.634 E-04	0.003 E-04
Eu-152	344.27	1.522 E-04	0.011 E-04
Ba-133	356.01	1.243 E-04	0.003 E-04
Ba-133	383.84	8.625 E-05	0.255 E-05
Cs-137	661.65	3.659 E-05	0.163 E-05
Eu-152	778.90	2.920 E-05	0.479 E-05
Eu-152	964.07	2.851 E-05	0.299 E-05
Co-60	1173.49	1.416 E-05	0.317 E-05
Co-60	1333.22	1.148 E-05	0.099 E-05
Eu-152	1408.01	1.153 E-05	0.083 E-05

in Multispect Software as shown from the data in tables 5.2, 5.3, 5.4 and 5.5 respectively.

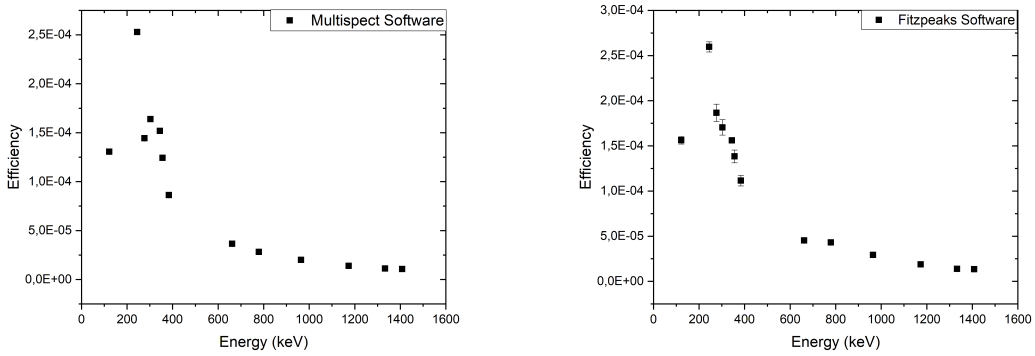

(a) Multispect software **(b)** Fitzpeaks software

Figure 5.4 Efficiency curves

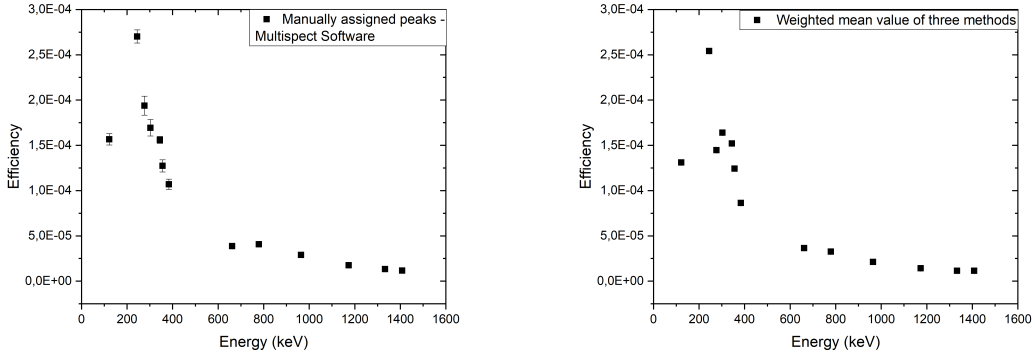

(a) Manually assigned peaks using Multispect Software

(b) Weighted mean value of the three methods

Figure 5.5 Efficiency curves

5.2 Fitting of the Efficiency Curve

In order to create the efficiency curves, the efficiency values from the Gaussian fit from Multispect and Fitzpeaks Software of the peaks were used. Then the fit of the efficiency curve was performed following three different methodologies; Multispect Software, non-linear least chi- squared fitting with SATLAS package and Cubic Spline Fit with Origin. More details about the fitting routines are described in the next sections.

5.2.1 Multispect Software Efficiency Curve Fit

When there is a certain geometry between the radioactive source and the detector and the measured count rates of the spectrum peaks are known, an efficiency calibration of the system can be used to calculate the source activity.

Multispect Software Tools allows the user to determine the efficiency of their system using a calibration source of known activity. The detector must have an energy calibration and a resolution calibration before an efficiency calibration can be entered, and the spectrum must be displayed in 'Energy Mode' with an energy horizontal axis.

After recording a spectrum from a calibration source of known activity the software

gives the option to press the 'Add Cursor Point' button. An efficiency calculation window is displayed allowing the efficiency and error to be determined for the selected peak. It is important to note that the efficiency is calculated for a specific peak of the spectrum at a specific energy with known intensity.

According to KROMEK's manual for the Multispect Software, all efficiency calibration points must be made with the same region of interest width factor setting for analysing the net counts in the peak. The error on each data point is calculated from the errors on the net count rate and the source activity. MultiSpect fits the efficiency data points with the following curve:

$$\ln \epsilon = \alpha_0 + \alpha_1 \ln E + \alpha_2 \ln E^2 + ...\alpha_n \ln E^n \tag{5.4}$$

Where: ϵ is the efficiency, E the energy, α_i are fitted coefficients, and the order of fit, n, is between 3 and 7.

5.2.2 SATLAS package Efficiency Curve Fit

The efficiencies at certain energies were calculated using the above methods for the sources Cs-137, Ba-133, Eu-152 and Co-60. These efficiencies were plotted as a function of the energy creating a curve. This efficiency curve was fitted with a chi-square fitting routine using the custom-written Python package named "Statistical Analysis Toolbox for LAser Spectroscopy" (SATLAS) (Gins et al., 2018). The chi-square minimization fitting routine applies a quickly converging algorithm known as Levenberg–Marquardt algorithm. The uncertainty is estimated with the use of a random walk through parameter space, for which the emcee package is utilized. In this package the "walkers" maneuver through the parametric space so that the space is explored faster than with the traditional Hamiltonian walking system (Gins et al., 2018).

The fit was modeled using the following 5 parameter function:

$$\epsilon = \frac{\sum_{i=0}^{4} \alpha_i (lnE)^i}{E} \tag{5.5}$$

where ϵ is the efficiency, E is the energy and the parameters α_i were calculated thanks to the chi-square fitting routine of SATLAS package.

5.2.3 Cubic Spline Fit

Interpolation is a technique used to estimate new data points from known data values.

Cubic Spline interpolation is a case for Spline interpolation that leads to an interpolating polynomial with smoother and less significant error than the ones from different interpolating polynomials (Lagrange polynomial or Newton polynomial).

Origin gives the user the possibility to use different interpolation techniques like Linear, Cubic Spline, Cubic B-Spline and Akima Spline interpolation. In this case the Cubic B-Spline method was utilised in order to be able to adjust the smoothness of the fit. The Cubic Spline method makes use of 3rd order polynomials, and fits the data in a piecewise way. The fact that the interplot is smoother means that the Spline interpolation has smaller error than the linear interpolation. The only difference between Cubic Spline interpolation and the Cubic B - Spline interpolation is the fact that it uses 3rd order Bezier splines to approximate the data. Reference (OriginLab, updated 2020) provides more details about the aforementioned interpolation techniques.

5.3 Activity measurement

The efficiency curve calculation allows a quantitative evaluation of activity concentration by simply using the Equation 5.7, which is 3.2 solved for the activity.

$$A = \frac{N}{\epsilon \times I \times t} \tag{5.6}$$

The activity of the sources was calculated for all the different methods using the different fit methods that were presented in the previous section (Multispect Software, SATLAS, Cubic Spline).

In the following sections the results from the different fitting methodologies are presented and compared.

5.3.1 Efficiency curve fit using SATLAS

Using the fit of the efficiency curve from the SATLAS package in Python, the activity was calculated and compared with the actual values of the activity of the sources on the day of the measurement, in order to check if the result is better for the fit of the efficiency curve provided by Multispect Software.

The efficiency values given to the SATLAS package were the ones calculated using the data from Multispect Software, Fitzpeaks Software and by manually assigning the peaks of the spectra with Multispect Software in order to make a Gaussian fit of the γ-ray spectra.

In Figures 5.6a, 5.6b, 5.7a and 5.7b the fit of the efficiency curve is presented using the efficiency values from Multispect Software, Fitzpeaks Software, from manually selecting the peaks using Multispect Software and their weighted mean values respectively. The full black line is a fit to the data according to equation 5.5 using SATLAS and the shaded area depicts the uncertainty of the fit. In Table 5.22 the fitting parameters are presented for the efficiency data calculated by the Multispect Software.

In Figure 5.7b, the efficiency curve of the weighted mean efficiency values from the Multispect Software, FitzPeaks Software and the manually assigned peaks using Multispect Software is fitted using SATLAS Python Package.

In Tables 5.6, 5.7, 5.8 and 5.9 the fitting parameters, as well as their uncertainties for all the different methods of calculating the efficiencies are presented, corresponding to the SATLAS fit shown in Figures 5.6a, 5.6b, 5.7a and 5.7b. With these fitting parameters it

Table 5.6 Fitting Parameters for Multispect Efficiency values

Fitting Parameters	**Values of Parameters**	**Uncertainty of Parameters**
a_1	-1.862 $E01$	$\pm 3.799E-01$
a_2	1.165 $E01$	$\pm 2.561E-01$
a_3	-2.699	$\pm 6.432E-02$
a_4	2.755 $E-01$	$\pm 7.128E-03$
a_5	-1.047 $E-02$	$\pm 2.944E-04$

Table 5.7 Fitting Parameters from FitzPeaks Efficiency values

Fitting Parameters	**Values of the Parameters**	**Uncertainty of Parameters**
a_1	-1.934 $E01$	± 2.703
a_2	1.217 $E01$	± 1.808
a_3	-2.838	$\pm 4.497E-01$
a_4	2.922 $E-01$	$\pm 4.932E-02$
a_5	-1.121 $E-02$	$\pm 2.014E-03$

Table 5.8 Fitting Parameters from Multispect Software by manually assigned fit

Fitting Parameters	**Values of the Parameters**	**Uncertainty of Parameters**
a_1	-3.115 $E01$	± 3.047
a_2	2.012 $E01$	± 2.035
a_3	-4.832	$\pm 5.052E-01$
a_4	5.125 $E-01$	$\pm 5.532E-02$
a_5	-2.029 $E-02$	$\pm 2.225E-03$

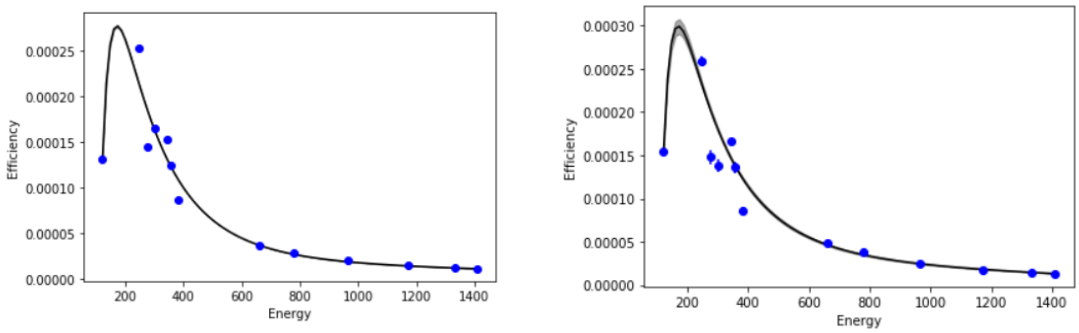

(a) Multispect software

(b) Fitzpeaks software

Figure 5.6 Fit of the efficiency curve for the middle position of the detector using SATLAS fit.

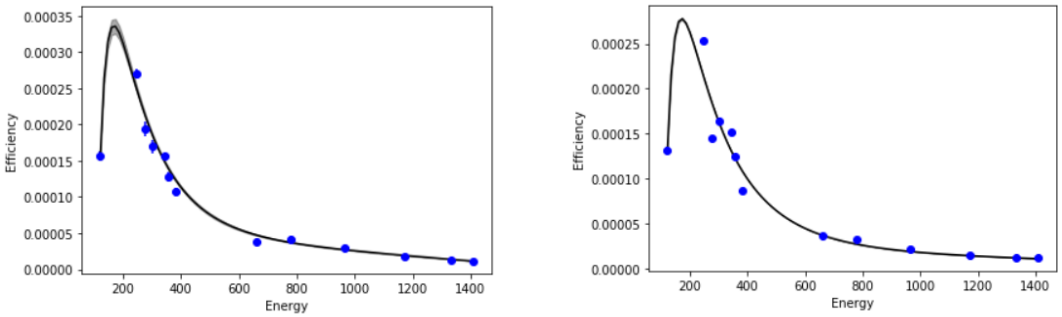

(a) Manually selecting peaks with Multispect software

(b) Weighted Mean Efficiency Values from the three methods

Figure 5.7 Fit of the efficiency curve for the middle position of the detector using SATLAS fit. The energies are shown in keV.

is possible to calculate the efficiency for any energy. The user only needs to insert these parameters to formula 5.5.

In the next section, the activity is calculated by implementing the above results of the SATLAS fit.

5.3.2 Calculation of the activity from the fit of the efficiency curve using SATLAS for the middle position of GR-1 detector

In this section, the activity of the sources used for the efficiency measurements in MEDICIS (Ba-133, Co-60, Eu-152 and Cs-137) is evaluated using the fit of the efficiency curves,

Table 5.9 Fitting Paramaters from weighted mean value efficiency data

Fitting Parameters	Values of the Parameters	Uncertainty of Parameters
a_1	-1.916 $E01$	$\pm 3.613E-01$
a_2	1.203 $E01$	$\pm 2.433E-01$
a_3	-2.796	$\pm 6.099E-02$
a_4	2.863 $E-01$	$\pm 6.749E-03$
a_5	-1.092 $E-02$	$\pm 2.783E-04$

which were presented in the previous section. In the next paragraphs, the comparison of the activities acquired by the fit using SATLAS package of the three efficiency curves (using Multispect, Fitzpeaks and Manually assigned peaks using Multispect), as well as their weighted mean value, is presented.

As it was aforementioned in section 5.3, the activity can be calculated using Equation 5.7, which is simply Equation 3.2 but solved for the activity. Since the efficiency has been calculated for every energy thanks to the fit of the efficiency curves and the live times, the counts of each peak as well as the intensities of the γ-ray emissions are known for each radioactive source (presented in Table 5.1), it is possible to calculate the activity that corresponds to each γ-ray emission energy. Henceforth, the plain average of the activities of the γ-ray emissions with the strongest emissions of each radioisotope is taken to calculate the activity of the source.

$$A = \frac{N}{\epsilon \times I \times t} \tag{5.7}$$

In Table 5.10, the comparison between the calculated activities after performing the fit of the efficiency curve using the efficiency data from Multispect and the actual activity of the sources is presented. The fit gives a good approximation of the activity especially for Ba-133 and Cs-137. However, it is obvious that the fit of the efficiency values from Multispect does not provide a sufficiently good approximation of the activity of Eu-152 and Co-60 sources.

In Table 5.11, the comparison between the calculated activity using the fitting parame-

ters acquired from SATLAS package for the efficiency curve gained from the analysis using the Fitzpeaks Software and the actual known activities of the sources on the day of the measurement is presented. As it can be seen from the small percentage difference, the SATLAS fit of the efficiency values extracted from the analysis of the data by the FitzPeaks Software provide a better estimation of the activity than the one from Multispect Software, especially for the case of Eu-152 and Co-60.

Table 5.10 Comparison of calculated Activity from the SATLAS fit of the efficiency curve versus the Actual Activity using the efficiency data from Multispect

Source	**Calculated Activity (Bq)**	**Actual Activity (Bq)**	**Difference in (%)**
Ba-133	5.91 E05	5.69 E05	3.7
Co-60	3.63 E04	2.98 E04	22
Eu-152	4.82 E04	3.68 E04	31
Cs-137	3.14 E04	2.96 E04	6.4

Table 5.11 Comparison of calculated Activity from the SATLAS fit of the efficiency curve versus the Actual Activity using the efficiency data from Fitzpeaks

Source	**Calculated Activity (Bq)**	**Actual Activity (Bq)**	**Difference in (%)**
Ba-133	5.29 E05	5.69 E05	7.1
Co-60	2.79 E04	2.98 E04	6.4
Eu-152	3.95 E04	3.68 E04	7.5
Cs-137	2.46 E04	2.96 E04	16

Table 5.12 presents the comparison between the calculated activity from the fitting parameters using SATLAS package for the fit of the efficiency curve calculated by manually selected peaks using Multispect Software and the actual activity of the sources on the day of the measurement. It is clear from the relatively small percentage difference that it also provides a good approximation for the calculation of the activity.

Furthermore, the comparison of the calculated activity from the fit using SATLAS package of the efficiency curve gained by the weighted mean efficiency values of the aforementioned methods (Multispect Software, Fitzpeaks and manually assigned peaks) is depicted in Table

Table 5.12 Comparison of calculated Activity from the SATLAS fit of the efficiency curve versus the Actual Activity using the efficiency data from manually assigned peaks with Mulatispect Software

Source	Calculated Activity (Bq)	Actual Activity (Bq)	Difference in (%)
Ba-133	5.16 E05	5.69 E05	9.3
Co-60	2.78 E04	2.97 E04	6.7
Eu-152	3.86 E04	3.68 E04	5
Cs-137	2.41 E04	2.96 E04	19

5.13.

Table 5.13 Comparison of calculated Activity from the SATLAS fit of the weighted mean efficiency values

Source	Calculated Activity (Bq)	Actual Activity (Bq)	Difference in (%)
Ba-133	5.90 E05	5.69 E05	3.7
Co-60	3.52 E04	2.98 E04	18
Eu-152	4.75 E04	3.68 E04	29
Cs-137	3.10 E04	2.96 E04	4.9

As it can be seen from Table 5.13, the fit of the weighted values does not give as good values for the activity as it is desired (especially for Co-60 and Eu-152) and it could be attributed to the contribution of the values from the method of Multispect that as it can be seen from Table 5.10 which also does not give a good approximation for the activities of the sources of Co-60 and Eu-152.

A solution to the problem is to calculate the weighted mean values of the efficiency data acquired through FitzPeaks Software and manually assigned Peaks using Multispect Software. The results are shown in Table 5.15 and the fit using SATLAS is depicted in Figure 5.8.

Finally, as it can be seen from Table 5.15 the weighted mean values of the efficiency of the two methods without including the results from Multispect provide a very good approximation for the calculation of the activity. Only the calculation of the activity for Cs-137

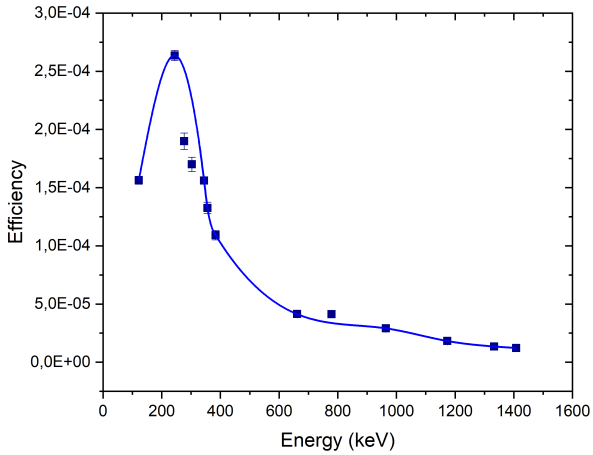

Figure 5.8 Efficiency as a function of the energy using the weighted mean efficiency values of the two methods (FitzPeaks and Manually assigned peaks with Multispect).

Table 5.14 Fitting Parameters from the fit of the weighted mean efficiency values of the two methods (Fitzpeaks and Manually assigned peaks with Multispect)

Fitting Parameters	**Values of the Parameters**	**Uncertainty of Parameters**
a_1	-2.896 E01	± 2.130
a_2	1.865 E01	± 1.424
a_3	-4.463	$\pm 3.539E-01$
a_4	4.719 E-01	$\pm 3.880E-02$
a_5	-1.863 E-02	$\pm 1.583E-03$

exceeds 10% difference.

In the next section, another kind of fitting of the efficiency curve (named Cubic Spline Fit) using Origin Software is utilized to check if it provides a better estimation of the activity than the fitting process using SATLAS package from Python. More details about this fit are presented in the next paragraphs.

Table 5.15 Comparison of calculated Activity from the SATLAS fit of the weighted mean efficiency values from Fitzpeaks and the Manually assigned Peaks from Multispect Software

Source	Calculated Activity (Bq)	Actual Activity (Bq)	Difference in (%)
Ba-133	5.13 E05	5.69 E05	9.9
Co-60	2.74 E04	2.98 E04	7.9
Eu-152	3.83 E04	3.68 E04	4.1
Cs-137	2.46 E04	2.96 E04	16

5.3.3 Cubic Spline Fit of the Efficiency Curve

In this section, the results of the Cubic Spline fit of the Efficiency curve using Origin are presented.

The Cubic Spline fit is able to create a smooth fit of the efficiency curve. With Origin program the smoothness of the fit can be adjusted. For example, in the case of FitzPeaks, after comparison of different smoothness parameters, the best choice for this parameter was 3×10^{-10}, while for the method of manually assigning the peaks, the smoothness factor was selected to the value of 6×10^{-10}.

In Figures 5.9a, 5.9b the Cubic Spline fit of the efficiency curve using the values extracted from Multispect Software and Fitzpeaks Software is presented.

In Figure 5.10a, the Cubic Spline fit of the efficiency curve using the values extracted from manually selecting the peaks from the spectra with Multispect Software is presented.

The Cubic Spline fit of the weighted mean efficiency values was also calculated. First the weighted mean values of all three different methods of calculating the efficiency values were calculated. Then, the weighted mean values of only FitzPeaks and from the manually assigned peaks using Multispect Software were calculated, as it was deemed that Multispect Software was not able to give as good an approximation of the activity as the ones from the other two methods. The estimation of the activity using the fit is presented in the next section.

In Figure 5.10b, the Cubic Spline fit of the weighted mean values of the efficiencies using all three methods (Multispect, FitzPeaks and manually assigned peaks with Multispect). In Figure 5.11, the Cubic Spline fit of the weighted mean values of only the two methods (FitzPeaks and Manually assigning peaks using Multispect) is presented.

The values of the interpolation of this fit from Figure 5.11 are shown in the Appendix (see Table A.2). Furthermore, the extrapolated values of the fit of the weighted mean value of the two methods (as shown in Figure A.2) are presented in the Appendix (see Table A.1).

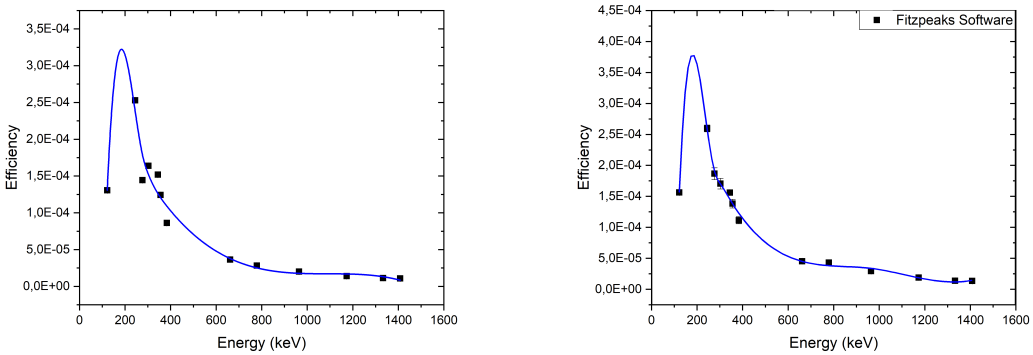

(a) Multispect software **(b)** Fitzpeaks software

Figure 5.9 Fit of the efficiency curve for the middle position of the detector using Cubic Spline Fit.

In Figure 5.11, the Cubic Spline fit of only the two methods (FitzPeaks and Manually assigned peaks using Multispect) is presented. These two methods were preferred as they provide a better approximation of the activity than the one from Multispect Software.

The aforementioned Cubic Spline fits of the efficiency curves were utilized to calculate the activity of the certified sources that were used in the MEDICIS laboratory. The results from this analysis are presented in the next section.

5.3.4 Calculation of the activity from Cubic Spline fit

In this section, the calculation of the activity using Cubic Spline fit (with Origin) is presented and compared with the respective results from the SATLAS fit.

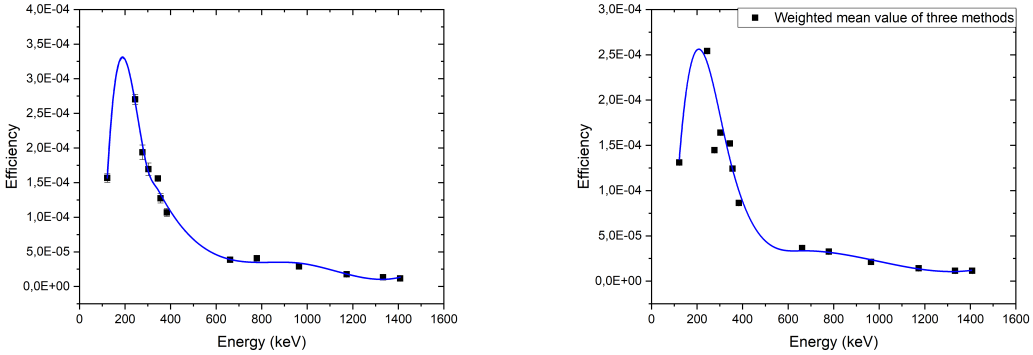

(a) Manually assigning peaks with Multispect software

(b) Weighted mean values of three methods

Figure 5.10 Fit of the efficiency curve for the middle position of the detector using Cubic Spline Fit.

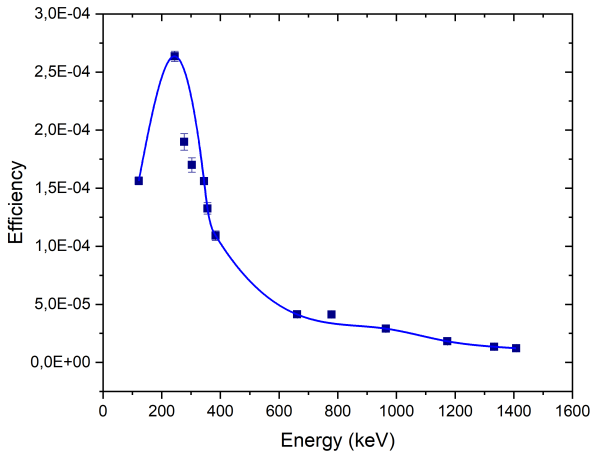

Figure 5.11 Efficiency as a function of the energy using the weighted mean efficiency values of the two aforementioned techniques (Fitzpeaks and manually assigned peaks from Multispect Software) for the middle position of the detector.

In Table 5.16, the comparison between the calculated activity using this Cubic Spline fit is shown. It is obvious that the Cubic Spline fit of these efficiency values gives a good approximation of the activity of the sources except from the one of Eu-152.

In Table 5.17, the comparison between the calculated activity using this Cubic Spline fit is shown. It is obvious that the activity values are better than the ones provided by

Multispect Software. There is no issue with the calculation of the activity of the source of Eu-152, as in the case of the analysis of the data with Multispect Software.

In Table 5.18, the comparison between the calculated activity using this Cubic Spline fit is shown. As it can be seen from this Table, the approximation of activity is as good as the one derived from the analysis of the efficiency values with FitzPeaks Software.

Table 5.16 Comparison of calculated Activity from the Cubic Spline fit Multispect efficiency values

Source	**Calculated Activity (Bq)**	**Actual Activity (Bq)**	**Difference in (%)**
Ba-133	6.04 E05	5.69 E05	6.2
Co-60	3.05 E04	2.98 E04	2.6
Eu-152	5.02 E04	3.68 E04	36
Cs-137	3.02 E04	2.96 E04	2.1

Table 5.17 Comparison of calculated Activity from the Cubic Spline fit FitzPeaks efficiency values

Source	**Calculated Activity (Bq)**	**Actual Activity (Bq)**	**Difference in (%)**
Ba-133	5.43 E05	5.69 E05	4.7
Co-60	3.08 E04	2.98 E04	3.6
Eu-152	3.58 E04	3.68 E04	2.6
Cs-137	2.54 E04	2.96 E04	14

In Table 5.19, the comparison between the calculated activity from the Cubic Spline fit of the weighted mean efficiency of the aforementioned three techniques is presented.

Table 5.18 Comparison of calculated Activity from the Cubic Spline fit using the data from the manually assigned peaks in Multispect Software

Source	**Calculated Activity (Bq)**	**Actual Activity (Bq)**	**Difference in (%**
Ba-133	5.49 E05	5.69 E05	3.7
Co-60	3.38 E04	2.97 E04	14
Eu-152	3.70 E04	3.68 E04	0.6
Cs-137	2.92 E04	2.96 E04	1.2

Table 5.19 Comparison of calculated Activity from the Cubic Spline fit of the weighted mean efficiency values

Source)	Calculated Activity (Bq)	Actual Activity (Bq)	Difference in (%)
Ba-133	5.92 E05	5.69 E05	3.9
Co-60	2.86 E04	2.98 E04	3.9
Eu-152	4.94 E04	3.68 E04	34
Cs-137	2.97 E04	2.96 E04	0.5

As it can be seen from Table 5.20, the relative difference of the activity values is very small in the case of Cubic Spline fit of the weighted mean efficiency values (below 5% difference for all the sources with the only exception of Cs-137 with 6.65%). These values were extracted from the fitting process of the efficiency curves from only two methods: the FitzPeaks Software and by manually assigning peaks using Multispect Software.

Table 5.20 Comparison of calculated Activity from the Cubic Spline fit of the weighted mean efficiency values of only two methods (Fitzpeaks and Manually assigned peaks using Multispect Software)

Source	Calculated Activity (Bq)	Actual Activity (Bq)	Difference in (%)
Ba-133	5.53 E05	5.69 E05	2.8
Co-60	2.89 E04	2.98 E04	2.6
Eu-152	3.66 E04	3.68 E04	0.5
Cs-137	2.76 E04	2.96 E04	6.6

5.4 Lower Position of the GR-1 CZT detector

In this section, the same experimental setup was implemented to recreate the experimental configuration in MEDICIS laboratory, but this time with lower position of the GR-1 CZT detector. Instead of being aligned with the center of the collection window, the detector was placed 1.25 cm below the center of the collection window. This was done in order to check if the efficiency of the detector would be comparable or even better than the previous geometry. A similar analysis with the middle position of the detectors was followed and the results are presented in the following sections.

5.4.1 SATLAS fit of the efficiency curve for the lower position

The fit of the efficiency curves with the data from Multispect Software, FitzPeaks Software and by manually assigned peaks using Multispect can be observed in Figures 5.12a, 5.12b, 5.13a and 5.13b. The full black line is a fit to the data according to equation 5.5 and the shaded area depicts the uncertainty of the fit.

The respective fitting parameters α_i from the chi-square fitting routine of SATLAS package have the values shown in Tables 5.21, 5.22, 5.23 and 5.24.

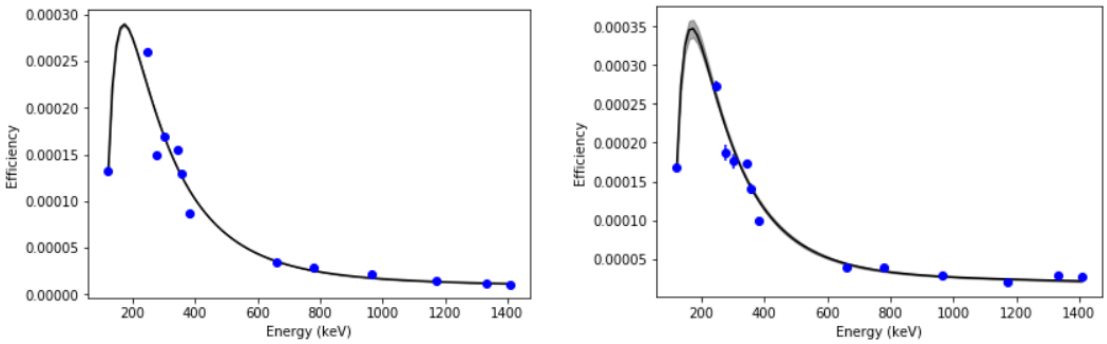

(a) Multispect software **(b)** Fitzpeaks software

Figure 5.12 Fit of the efficiency curve for the lower position of the detector.

The efficiency as a function of the energy using the weighted mean values of the efficiency from the two methods, which gave the best estimation of the activity (Manually assigned

Table 5.21 Fitting Parameters for the lower position of the detector using the efficiency values from Multispect Software

Fitting Parameters	Values of the Parameters	Uncertainty of Parameters
a_1	-1.918E01	$\pm 4.672E-01$
a_2	1.193E01	$\pm 3.153E-01$
a_3	-2.744	$\pm 7.919E-02$
a_4	$2.775E-01$	$\pm 8.779E-03$
a_5	$-1.043E-02$	$\pm 3.627E-04$

Table 5.22 Fitting Parameters for the lower position of the detector using the efficiency values from Fitzpeaks Software

Fitting Parameters	Values of the Parameters	Uncertainty of Parameters
a_1	-2.659E01	± 4.108
a_2	1.679E01	± 2.769
a_3	-3.925	$\pm 6.946E-01$
a_4	$4.039E-01$	$\pm 7.769E-02$
a_5	$-1.545E-02$	$\pm 3.169E-03$

Table 5.23 Fitting Parameters for the lower position of the detector using the efficiency values from manually assigning the peaks with Multispect Software

Fitting Parameters	Values of the Parameters	Uncertainty of Parameters
a_1	-2.637E01	± 1.341
a_2	1.659E01	$\pm 8.959E-01$
a_3	-3.872	$\pm 2.226E-01$
a_4	$3.979E-01$	$\pm 2.440E-02$
a_5	$-1.523E-02$	$\pm 9.953E-04$

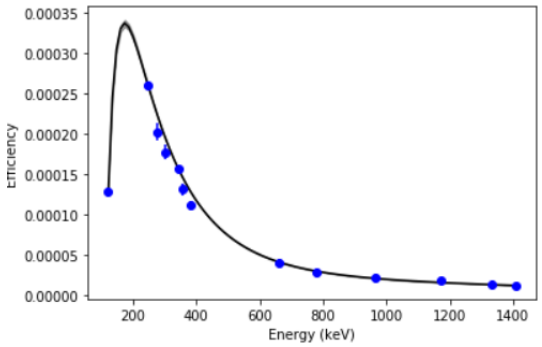

(a) Manually selecting from Multispect Software

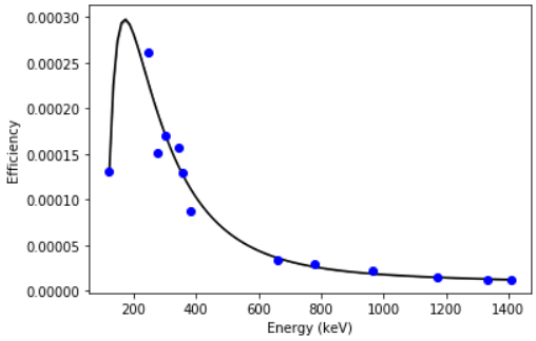

(b) Weighted mean Value of three methods

Figure 5.13 Fit of the efficiency curve for the lower position of the detector.

Table 5.24 Fitting Parameters for the lower position of the detector using the efficiency values from the weighted mean values of the three methods

Fitting Parameters	**Values of the Parameters**	**Uncertainty of Parameters**
a_1	-2.161E01	$\pm 4.074E-01$
a_2	1.355E01	$\pm 2.741E-01$
a_3	-3.147	$\pm 6.864E-02$
a_4	$3.216E-01$	$\pm 7.584E-03$
a_5	-1.222$E-02$	$\pm 3.122E-04$

peaks using Multispect and FitzPeaks) is presented in Figure 5.14. The result of the comparison of the calculated activity using this fit is presented in Table 5.28. The fitting parameters of this Figure are presented in Table 5.25.

The results of the comparison of the calculated Activity using the efficiency curve fit from SATLAS compared to the actual activity of the sources are presented in the next section.

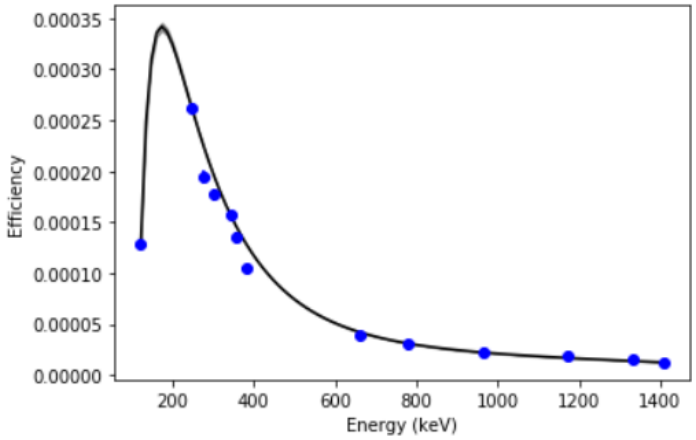

Figure 5.14 Efficiency as a function of the energy using the weighted mean values of the efficiency from the two methods (Manually assigned peaks using Multispect and FitzPeaks) for the lower position of the detector. The full black line is a fit to the data according to Equation 5.5 and the shaded area depicts the uncertainty of the fit.

Table 5.25 Fitting Parameters for the lower position of the detector using the efficiency values from the weighted mean values of the two methods (Manually assigned peaks using Multispect and FitzPeaks)

Fitting Parameters	Values of the Parameters	Uncertainty of Parameters
a_1	-2.846E01	$\pm$1.244
a_2	1.802E01	$\pm$8.315$E-01$
a_3	-4.231	$\pm$2.07$E-01$
a_4	4.380$E-01$	$\pm$2.265$E-02$
a_5	-1.690$E-02$	$\pm$9.245$E-04$

5.4.2 Calculation of the Activity using SATLAS fit for the lower position

The comparison between the calculated and the expected activity of the radioactive sources used for the efficiency calculation of the detector in the lower position is presented using the SATLAS fit with Python.

It is clear that the weighted mean efficiency values of either all the methods or just the two which provide a better estimation than the one from Multispect, give a good estimation of the activity of the sources, with the exception of Eu-152, which has a relatively big

Table 5.26 Comparison of calculated Activity from the SATLAS fit of the efficiency curve versus the Actual Activity for the lower position of the detector using FitzPeaks

Source	Calculated Activity (Bq)	Actual Activity (Bq)	Difference in (%)
Ba-133	5.03 E05	5.67 E05	11
Eu-152	4.05 E04	3.66 E04	11
Co-60	3.09 E04	2.95 E04	4.8
Cs-137	2.68 E04	2.95 E04	9.2

Table 5.27 Comparison of calculated Activity from the SATLAS fit of the efficiency curve obtained by the weighted mean value of the three aforementioned methods versus the Actual Activity for the lower position of the detector.

Source	Calculated Activity (Bq)	Actual Activity (Bq)	Difference in (%)
Ba-133	5.85 E05	5.67 E05	3.2
Co-60	3.52 E04	2.95 E04	19
Eu-152	5.47 E04	3.66 E04	49
Cs-137	3.30 E04	2.95 E04	12

Table 5.28 Comparison of calculated Activity from the SATLAS fit of the efficiency curve obtained by the weighted mean value of the two methods versus the actual activity for the lower position of the detector.

Source	Calculated Activity (Bq)	Actual Activity (Bq)	Difference in (%)
Ba-133	5.10 E05	5.67 E05	10
Co-60	3.13 E04	2.95 E04	6.3
Eu-152	4.92 E04	3.66 E04	34
Cs-137	2.81 E04	2.95 E04	5

percentage difference.

Next, the Cubic Spline Fit of the efficiency curve will be presented and compared with the SATLAS fit.

5.4.3 Cubic Spline Fit of the efficiency curve for the lower position

In this section, the Cubic Spline fit of the efficiency curve using Origin is presented in order to be compared with the SATLAS fit using Python, which was presented in the previous section. Figure 5.15 presents the Cubic Spline fit of the efficiency curve from the lower position of the GR-1 CZT detector. The efficiency curve presented is calculated from the weighted mean value of the absolute (for the position) photopeak efficiencies acquired from Multispect and Fitzpeaks Software. In the next section, the Cubic Spline fit is utilized to calculate the activity of the certified sources.

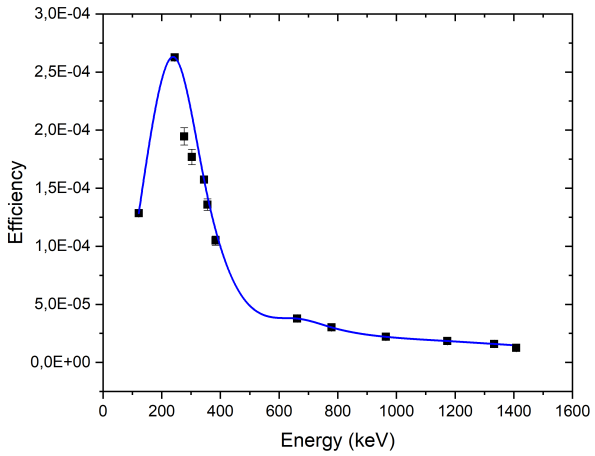

Figure 5.15 Cubic Spline fit of the efficiency curve using the weighted mean efficiency values from the two methods (Manually assigned peaks using Multispect and FitzPeaks) for the lower position of the detector.

5.4.4 Calculation of the Activity from the Cubic Spline fit

In this section, the calculation of the activity from the Cubic Spline fit, as well as the comparison with the actual activity of the sources are presented.

In Table 5.29, the comparison of calculated Activity from the Cubic Spline fit of the efficiency curve obtained by the weighted mean value of the two methods versus the actual activity for the lower position of the detector is shown. It is clear that, except from Eu-152 (with a percentage difference of 20%), the estimation of the activity has small percentage difference (below 10%).

It is clear that Cubic Spline fit is able to give a better approximation of the the activity of the sources than the chi-squared fitting routine from SATLAS.

Table 5.29 Comparison of calculated Activity from the Cubic Spline fit of the efficiency curve obtained by the weighted mean value of the two methods versus the actual activity for the lower position of the detector.

Source	Calculated Activity (Bq)	Actual Activity (Bq)	Difference in (%)
Ba-133	5.04 E05	5.67 E05	11
Co-60	2.81 E04	2.95 E04	4.6
Eu-152	4.41 E04	3.66 E04	20
Cs-137	2.97 E04	2.95 E04	0.7

5.5 Comparison between the middle and the lower position of the detector

In this section, the comparison between the efficiency values between the middle and the lower position of the GR-1 detector are presented. In Figure 5.16a, the efficiency values from the middle position of the detector are compared to the efficiency values from the lower position of the detector. Both of the efficiency values are the result of the weighted mean value of two methods (FitzPeaks Software and Manually assigned peaks using Multispect Software).

As it can be seen from Figure 5.16b, the ratio between the efficiency values of the two configurations and its uncertainty is plotted. It is obvious that it does not exceed 1.5 ratio, henceforth both configurations give approximately the same results. The biggest difference appears to be for the lower and middle energies. Simulations were performed using PENMAIN to verify this result, as shown in Chapter 8.

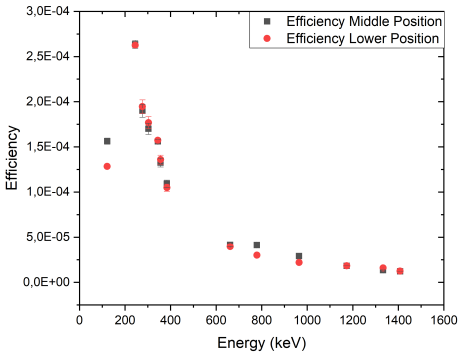

(a) Comparison of efficiencies for the lower and middle position of GR-1 detector.

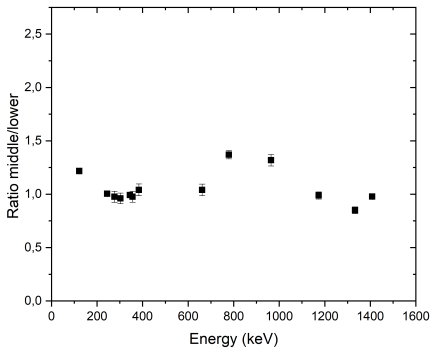

(b) Ratio between the efficiency values with the detector in Middle and Lower Position

5.6 Two sources in a row behind the collection foils

A different geometry was also tested by placing two sources next to each other, each behind a collection foil. This was done to check if the source next to the central one affects the γ-ray spectrum and therefore, if it affects the measured activity.

The central source behind the foil was Ba-133 with an activity of 5.7 E05 Bq on 12.02.2020 and next to it, again behind a foil, the source of Eu-152 with an activity of 3.7 E04 Bq calculated on 12.02.2020. In Figure 5.17a, the resulting spectrum can be observed with a yellow line with live time of the detector 74078.7 seconds. With the pink line, the spectrum of Ba-133 with live time 95927.5 seconds is presented. The blue line represents the spectrum of Eu-152 with live time 258988.3 seconds. As it can be seen from Figure 5.17a, the final spectrum of the two aligned sources is very similar to the spectrum of the source with the higher activity, which was the central one, Ba-133. The peak of 120 keV from the Eu-152 is the only one appearing clearly in the final spectrum of the two sources.

In Figure 5.17b, the resulting spectrum of combining the Ba-133 source with Co-57 can be seen. The pink line is the spectrum of the two sources aligned behind the golden foils with a live time of 84255.3 seconds. Ba-133 was situated behind the central foil while Co-57 was located on the side again behind a golden foil. The yellow line in the figure corresponds to the spectrum of Co-57 alone with a live time of 95927.5 seconds. The live times are comparable so the comparison of the two spectra has logical sense. It is obvious that, since Co-57 was a source with high activity (514130 Bq), the peak of 122.06 keV that corresponds to just the Co-57 source is prominent.

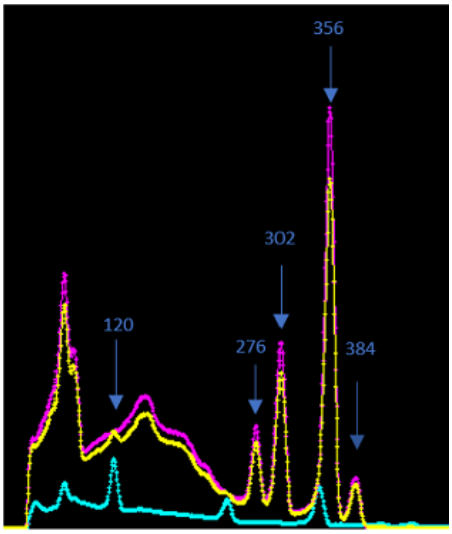

(a) Gamma-ray photon spectra using GR-1 with Multispect Software. The yellow line is the spectrum of combined Ba-133 and Eu-152. The pink line is the spectrum of Ba-133 and the blue line is the spectrum of Eu-152 source.

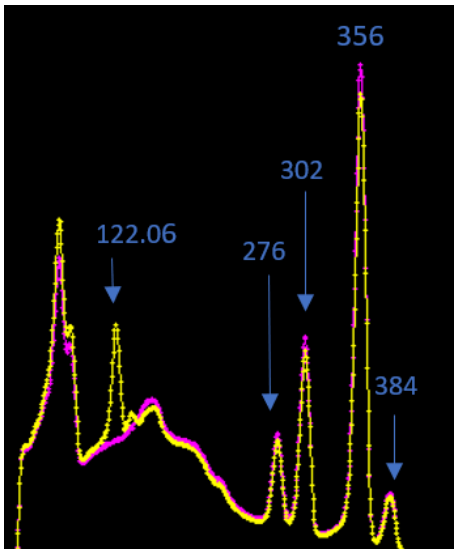

(b) Gamma-ray photon spectra using GR-1 with Multispect Software. The yellow line is the spectrum of Ba-133 and Co-57 together. The pink line is the spectrum of Ba-133.

Figure 5.17 Comparison of the acquired γ-ray photon spectra using GR-1 detector with Multispect Software to check the effect of a second source behind the collection foil.

5.7 Conclusions

For the middle position of the detector, two different fitting processes were tested for the calculated efficiency curves and both methods seem to provide a good approximation of the activity of the sources. The small difference between the calculated activity and the actual activity for each source indicated that the fit of the efficiency curve provided by Multispect software gave in both fitting processes a substandard approximation for the Eu-152 source (31% for SATLAS fit and 37% for Cubic Spline fit). Therefore, it was deemed a good solution to exclude from the weighted mean value calculation the efficiency values calculated with Multispect Software. Moreover, from the comparison of the Cubic Spline fit in Origin with the fit using SATLAS package in Python, it is clear that the Cubic Spline fit of the weighted mean values using the data from Fitzpeaks and the manually assigned peaks from Multispect gives a better estimation of the activity values, with a percentage difference that is not exceeding 3% for all the sources except from Cs-137 with 6.6% difference. The relative differences are within the uncertainties of the activity of the sources.

for the lower position of the GR-1 detector, the comparison between the two different methods of fitting the efficiency curve, indicate that the Cubic Spline fit using Origin gives slightly better results for the purpose of the activity calculation than the fit using SATLAS package in Python. From the comparison of the weighted mean values of the efficiency values gained by the Fitzpeaks software and Manually assigned peaks, it is clear that the relative difference in both fitting processes is below 10% with the exception of Eu-152 with a percentage difference of 34% for the fit using SATLAS package and 20% using the Cubic Spline fit in Origin. Furthermore, simulations using PENMAIN have been performed and will be discussed in detail in Chapter 8.

From the comparison between the two different positions of the detector it is concluded that both of the configurations give approximately the same efficiency results. This result suggests that it is possible to use GR-1 detector at a lower position (1.25 cm below the center

of the window of the collection chamber) without significant difference in the efficiency values.

The measurements with two sources behind the foil were performed to check whether the collection of a radioisotope other than the expected one, situated at the neighbor collection foil, affects the activity calculation of the desired and expected radioisotope. It should be reminded that in MEDICIS laboratory, there are three collection foils in the collection chamber. In conclusion, the acquired spectra from the two different sources with different activities behind the golden foil showed that there is a negligible effect on the calculated activity when two sources were located behind the collection foil.

Further analysis with simulations using PENMAIN verifies this experimental result between the two different geometries and is presented later in this thesis in Chapter 8.

Indeed, in Chapter 6 the online measurement of activity was performed using GR-1 CZT detector at the lower position and the results verify that GR-1 CZT detector from KROMEK can be used for activity assessment during the operation of MEDICIS facility successfully.

Chapter Six

Online measurements of activity during MEDICIS operation

In this chapter, the online measurements of the activity during the collection of radioisotopes in MEDICIS laboratory are presented. These measurements were performed using GR-1 CZT detector from KROMEK and they were verified with measurements gained by a High Purity Germanium detector. More details about this process are described in detail in the next sections.

6.1 Collection of Radioisotopes Tb-155 and Sm-153

After a 3 month-period of maintenance and upgrade of the facility and due to the special CERN closure because of the Covid-19 outbreak, the MEDICIS facility could restart operation with the extraction of radioactive ion beam only in May 2020. Up to mid-august 2020, five collections of radioactive isotopes have been performed. Two batches of Tb-155 have been radio-chemically purified at NPL (UK), and then used by the CHUV (Lausanne Hospital) and the radiopharmaceutical research center of KU Leuven (Belgium). Both institutes have used Tb-155 for radiolabeling studies and successfully managed to, respectively, label Tb-155 with DTPA chelated antibodies (CHUV) and with heat-sensitive biomolecules

(KU Leuven). The former reached a 100% labelling yield indicating that the purified Tb-155 provided by MEDICIS can be used for pre-clinical applications. Three batches of Sm-153 have been shipped to SCK (Belgium), where radiochemistry studies are performed and the institute is ready to perform the first radiolabeling trials, in collaboration with KU Leuven (Belgium).

6.1.1 Implementation of GR-1 for online Calculation of Activity in MEDICIS

The implementation of the KROMEK GR-1 CZT detector helped the operation team to improve the collection and get an estimation of the implantation rate in MBq/h during beam extraction. The efficiency curve was taken from the one measured during this thesis for the lower position of the detector in order to accommodate with the camera placed above the detector and also since the efficiency curve were showing similar values in the case of the lower and middle positions. The detector was placed at 1.25 cm below the center of the window and at a distance of 1 cm from the window as shown in the Figures 6.1a and 6.1b and as performed for the calibration of the detector with sources of known activities during this master thesis.

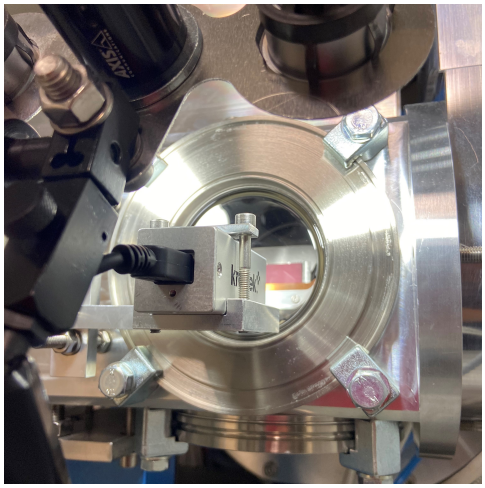

(a) GR-1 detector at lower position at MEDICIS facility

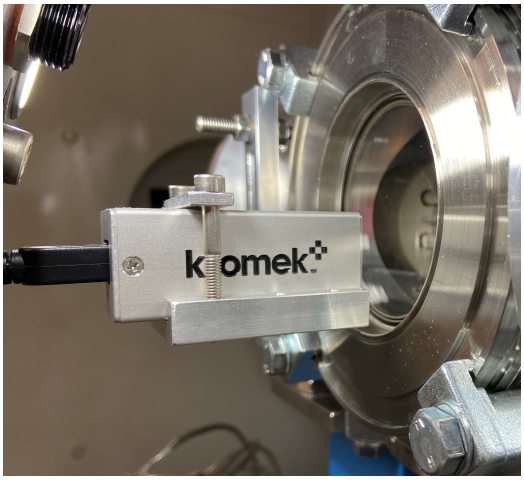

(b) GR-1 detector 1.25cm below the center of the collection window

Figure 6.1 GR-1 detector during the online measurement at MEDICIS

6.1.2 Comparison of results with High Purity Germanium detector

Table 6.1 presents the measurement results from both the High Purity Germanium (HPGe) detector used by the radiation protection team and the online measurement of CZT - GR1 KROMEK detector. The small relative difference between these measurements, especially for the activity measurements of Sm-153, confirms that the GR-1 detector can be used for online activity measurements. It can also be seen that the dead time of GR-1 CZT detector does not exceed 5%.

Table 6.1 Comparison of measured activities between the two detectors

Radioisotope	**Detector**	**Measured Activity (MBq)**	**Difference in (%)**	**Experimental Uncertainty (%)**
Sm-153	HPGe	19.5	6.2	6
Sm-153	KROMEK CZT	18		4% dead time
Tb-155	HPGe	2.90	27	20.40
Tb-155	KROMEK CZT	4.00		1% dead time
Tb-155	HPGe	2.90	25	3.20
Tb-155	KROMEK CZT	3.9		1% dead time
Sm-153	HPGe	31.00	0.0	10.70
Sm-153	KROMEK CZT	31		4% dead time
Sm-153	HPGe	21.00	4.8	21.30
Sm-153	KROMEK CZT	20		4% dead time

6.2 Conclusions

The comparison between the results for the activity on the foil, as shown in Table 6.1, using the high purity germanium detector by the radiation protection team and the measurement using GR-1 CZT detector from KROMEK, verifies that the GR-1 detector can be used for online activity measurements providing an accurate estimate of the activity implanted on the foils. GR-1 CZT gives results with good resolution, good efficiency, it is a robust detector and it can operate in room temperatures without cooling unlike the HPGe detector, that cannot operate unless it is being cooled down.

Chapter Seven

CZT Spectrometric Detection Probes

CZT detectors have been shown to be the option of choice for MEDICIS monitoring. They come in several shapes and models, and recent developments of hemispherical CZT detectors may prove even more convenient for this purpose. In the following we investigate several CZT detectors. They were tested in the laboratory of Complutense University of Madrid. A brief description of each detectors characteristics as well the experimental results will be presented in the following sections.

7.1 SDP500S CZT detector

In order to improve the spectrometric performance of the CZT detectors, quasi-hemispherical detectors were developed, which take advantage of the optimized charge collection due to the unique quasi-hemispherical shape of these detectors (Ivanov et al., 2009). Therefore, it is interesting to compare this kind of detector to the GR-1 model, to check which one is better suited for spectrometric measurements in MEDICIS.

Spectrometric Detection Probe SDP500S from RITEC (RITEC, updated 2020) is a quasi-hemispherical detector, able to operate in room temperatures (preferable range $0 - 50^oC$), while providing high energy resolution, wide detection range, high efficiency, high count rate capability and small consumption power. Figure 7.1 shows the comparison between

SDP500S, SDP1500 and SDP4000 probes. Their difference between these models, as their name suggests, is the size of the CZT crystal that they include ($0.5cm^3$ for SDP500S, $1.5cm^3$ for SDP1500 and $4cm^3$ for SDP4000. In this thesis, the SDP500S Probe was the tested model.

Figure 7.1 Spectrometric Probes. From top to bottom: SDP4000, SDP1500 and SDP500S

In Figure 7.2, the design of the detector is shown.

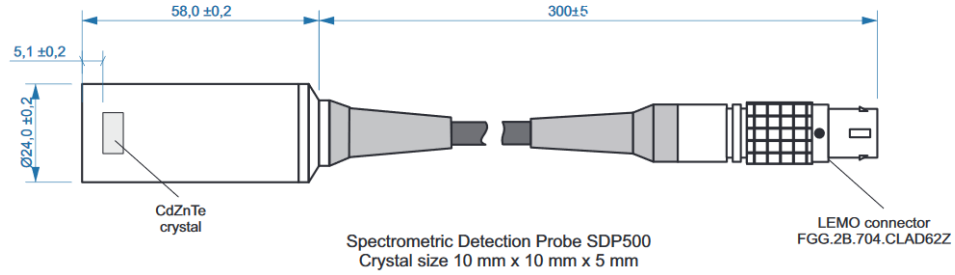

Figure 7.2 Design features of SDP500S. Adapted from Ref. (RITEC, n.d.)

According to the manufacturer the specifications for the SDP500S probe are presented in Table 7.1

In the following paragraphs, the efficiency curve calculation, the activity estimation and the energy resolution of the detector are analysed and presented.

Table 7.1 SDP500S Probe.

Head dimensions	Volume	Bias Voltage	FWHM at 662keV	Peak/Compton at 662keV
$\oslash 24 \times 58mm$	0.5 cm^3	$\leq 1500V$	$\leq 2.5\%$	≥ 5.0

7.1.1 Efficiency Calculation for SDP500S detector

Sources of Eu-152, Ba-133 and Cs-137 were placed in front of the SDP500S detector at different distances (25 mm and 50 mm). Furthermore, the effect of placing an aluminium foil of different thicknesses (1 mm and 3 mm) was studied. This effect is important in order to understand if the casing of a detector plays an important role in the efficiency measurements and to check the effect of materials in front of the detector on its efficiency. The analysis of the spectrum was achieved using Multispect Software, which was described in previous sections of this thesis.

In Figures 7.3a and 7.3b, the effect of the distance and the thickness of the aluminium foil in the efficiency of the SDP500S detector is shown. It can be easily noticed that the effect of the distance is more dominant than the one of thickness of the aluminium foil. Furthermore, both effects are more prominent for the lower energies.

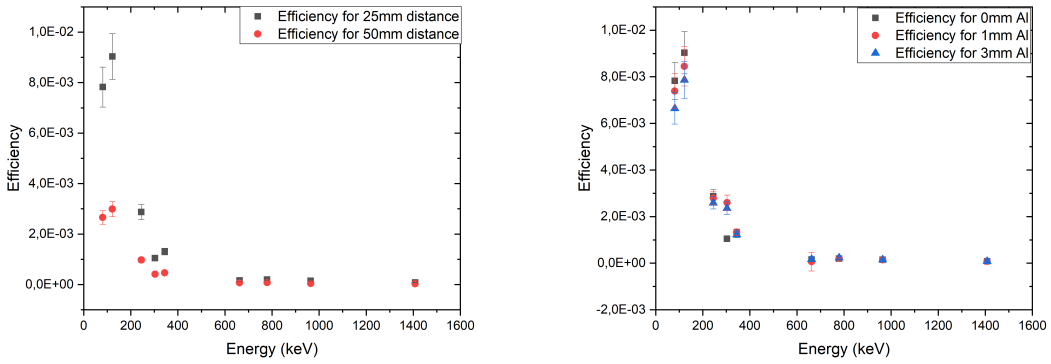

(a) Comparison of Efficiencies for different distances.

(b) Comparison of Efficiencies for different Al thickness.

Figure 7.3 Comparison of Efficiencies of SDP500S detector for different distance and Al thickness.

7.1.2 Activity Calculation with SDP500S detector

In this section, the activity of Ba-133, Cs-137 and Eu-152 sources was calculated for the SDP500S detector, using the SATLAS package from Python to fit the efficiency curves. The methodology that was followed to calculate the activity it the same as the one described for the GR-1 detector. Briefly, equation 5.7 was used, because the live time, the counts, the efficiency from the fit and the intensity of the γ-ray emissions of the sources were known. Then, the average of the calculated activities for each γ-ray emission of the radioisotopes was calculated and compared to the actual activity of the source on the day of the measurement.

In Figures 7.4a and 7.4b, SATLAS fit is represented with the solid black line, while the uncertainty of the fit is depicted with the grey area. The fit was performed for the 50mm distance with no aluminium foil in front of the detector and for 50mm distance with an Aluminium foil of 1mm thickness. In Figures 7.4a and 7.4b, the energies of Eu-152 source (121.8 keV, 244.7 keV, 344.3 keV, 778.9 keV, 964.1 keV and 1408 keV), Ba-133 source (81 keV, 302 keV) and Cs-137 (662 keV) create the efficiency curves.

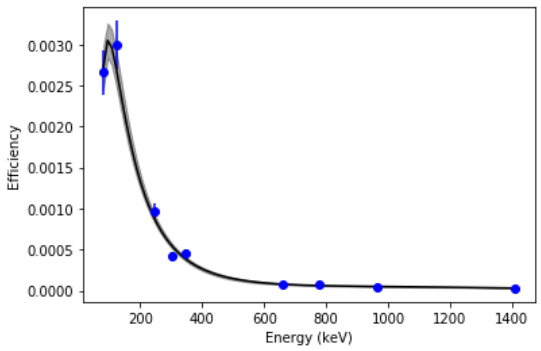

(a) SATLAS fit for 50 mm distance and 0mm Al thickness

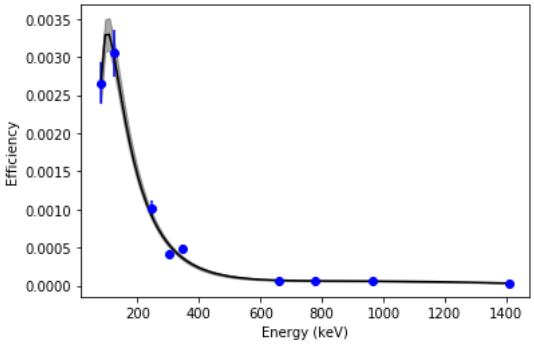

(b) SATLAS fit for 50 mm distance and 1mm Al thickness

Figure 7.4 Comparison of Efficiencies of SDP500S detector for different distance and Al thickness.

In Table 7.2, the comparison between the calculated and the actual Activity for SDP500S detector for the distance of 50 mm without Aluminium in front of the detector is shown. From the small percentage difference it can be concluded that the fit gives a good approximation

of the activity, within the source activity uncertainties

Table 7.2 Comparison between calculated and actual activity with SDP500S detector

Source	**Calculated Activity (Bq)**	**Activity Uncertainty** (%)	**Actual Activity (Bq)**	**Difference in** (%)
Ba-133	1.24 E04	10	1.42 E04	13
Eu-152	1.90 E04	10	1.76 E04	8.1
Cs-137	1.12 E05	10	1.17 E05	4.3

7.1.3 Energy Resolution of SDP500S detector

In this section, the resolution of the SDP500S detector is explored for different energies. Figure 7.5a depicts the energy resolution in percentage as a function of the energy for two different distances of the source from the detector (25 mm and 50 mm), while Figure 7.5b depicts the energy resolution as a function of the energy for the same distance but different thickness of the aluminium foil. It can be seen from Figure 7.5a, that for the energy of 964 keV emission the resolution is increasing, which is not the expected behavior. This could be attributed to the fact that close to the 964 keV peak there are many more peaks from Eu-152 that might overlap.

Furthermore, it can be seen from Figure 7.5b, that the energy resolution has higher values for higher energies and for thicker aluminium foil in front of the detector. In general though, the differences for both different distances and thickness of aluminium are quite minimal and could be thought as negligible.

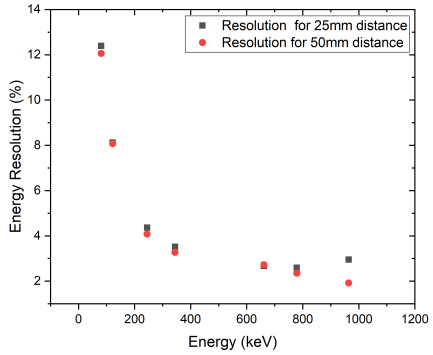

(a) SDP500S resolution for 25 mm and 50 mm distance versus the energy.

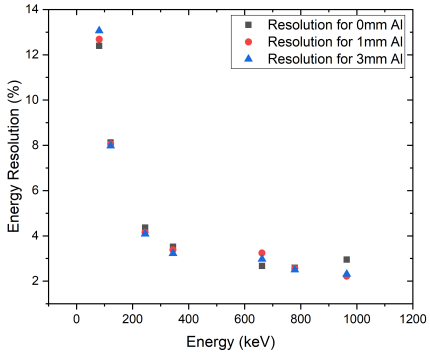

(b) SDP500S resolution for different Al thickness

Figure 7.5 Comparison of the resolution of the SDP500S detector for different distance and Aluminium thickness.

7.1.4 Peak to Compton Ratio for SDP500S detector

In this section, the Peak to Compton ratio for SDP500S CZT detector was calculated from the spectra of Eu-152 and Cs-137 sources for different distances and without an aluminium foil in between (apart from the one of the casing of the detector).

Peak to Compton Ratio is a good indicator of the detector's performance. Compton scattering happens when an incident photon is not completely absorbed by CZT detector. Therefore, the detector counts only part of this incident photon's energy. In a γ-ray spectrum this appears as Compton Continuum. As it is referred in (IEEE, 1997), the ratio between the full-energy peak to the Compton Continuum is known as the Peak to Compton (or P/C) ratio. It is important to have a small Peak to Compton ration in order to ensure a good γ-ray spectrum quality.

Peak to Compton ratio is easily acquired, as it can be seen in Figure 7.6 for the case of Cs-137. The user needs to simply divide the counts from the Photopeak with the counts of the Compton Continuum.

The results are presented in Table 7.3. It can be seen that the Peak to Compton ratio is very good.

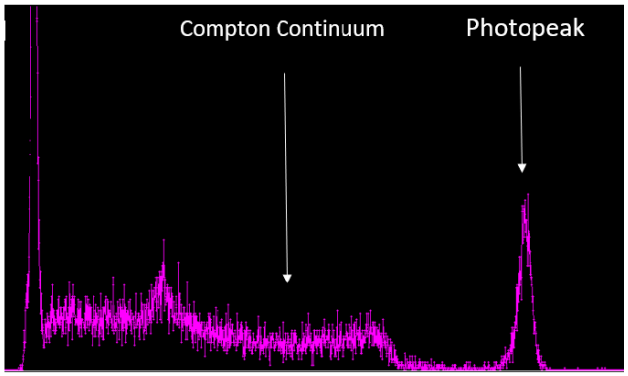

Figure 7.6 Cs-137 spectrum obtained with Multispect Software for 50mm distance with no Al foil using SDP500S and live time 300 seconds.

Table 7.3 Peak to Compton Ratio of SDP500S detector without Al foil

Source	Energy (keV)	Distance (mm)	Peak to Compton Ratio
Eu-152	244.7	84.00	3.96
	1408.0	84.00	12.51
Cs-137	661.7	50.00	4.13

Peak to Compton Ratio for GR-1 and GR-05 detectors

Tables 7.4 and 7.5 present the Peak to Compton Ratio for GR-1 and GR-05 CZT detectors from KROMEK. The analysis was done for the spectra that were acquired at the MEDICIS experimental configuration. It can be seen that the Peak to Compton ratio is very good for the GR-1 detector.

Table 7.4 Peak to Compton Ratio of GR-1 detector at MEDICIS Laboratory

Source	Energy (keV)	Distance (cm)	Peak to Compton Ratio
Eu-152	244.7	8.4	2.26
	1408.0	8.4	13.64
Cs-137	661.7	8.4	5.63

Table 7.5 Peak to Compton Ratio of GR-05 detector at MEDICIS Laboratory

Source	Energy (keV)	Distance (cm)	Peak to Compton Ratio
Eu-152	244.7	8.4	2.14
	1408.0	8.4	13.93
Cs-137	661.7	8.4	19.69

7.1.5 Count rate of SDP500S detector

In this section, the count rate of SDP500S detector is calculated. As it can be observed from Figure 7.7, the decay time τ was calculated by performing an exponential fit at the tail of the preamplified signal and is equal to is 32 μs. Therefore, the full signal time is about 3τ, so equal to 96 μs. Thus, the count rate can be calculated to be around 10000 counts/s for the SDP500S detector.

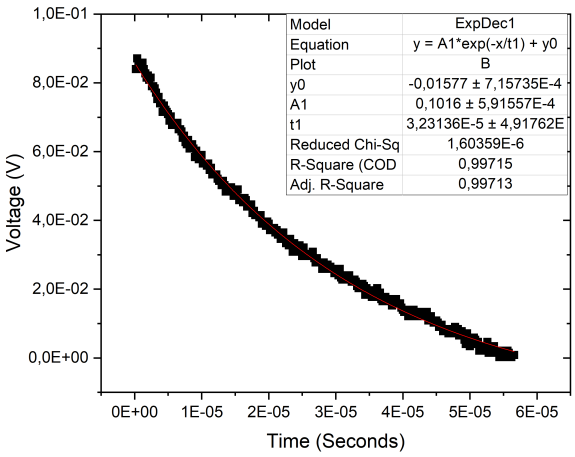

Figure 7.7 Exponential fit of the preamplified signal's tail from SDP500S detector.

7.2 LAB coplanar grid (CPG) detector

LAB CPG detector from KROMEK, as seen in Figure 7.8, consists of a CZT crystal ($1000mm^3$) in a coplanar grid electrode setup. This configuration enables the collection

of electrons-only, which leads to a reduction in tailing that is due to the trapping of charge. Thus, LAB CPG detector offers an improved detector performance suitable for applications that require high resolution and low background signal. Inside the casing (38.1 mm diameter x 159.5 mm length), apart from the CZT crystal, the preamplifier electronics are situated. Furthermore, according to the manufacturer, the detector can be easily connected to both NIM-based and desktop MCA electronics.

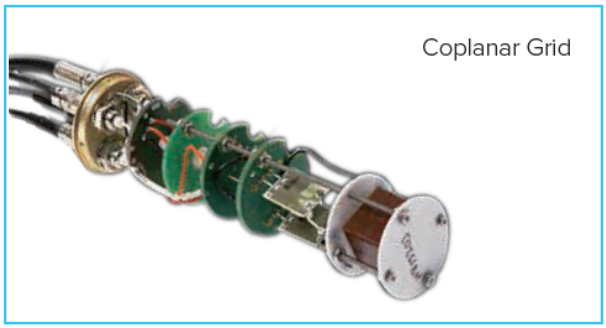

Figure 7.8 Coplanar grid LAB CPG detector. Adapted from Ref. (Mirion, 2019)

7.2.1 Calculation of Efficiency and Activity with LAB CPG detector

In this section, the activity of sources Ba-133 and Eu-152 was calculated for the LAB CPG detector, using the SATLAS package from Python to fit the efficiency curves. The methodology is the same as in the case of GR-1 and SDP500S detectors. The result was compared to the expected activity of the sources on the day of the measurement. In Figures 7.9a and 7.9b, the energies of Eu-152 source (121.8 keV, 244.7 keV, 344.3 keV, 964.1 keV and 1408 keV) and Ba-133 source (81 keV, 302 keV) create the efficiency curves.

As it can be observed from Table 7.6, the calculated activity has a very small percentage difference compared to the actual activity on the day of the measurement. The fit of the efficiency curve using the SATLAS package (Python) for the calculation of the activity was for the efficiency values acquired from the spectra at the distance of 50 mm from the source

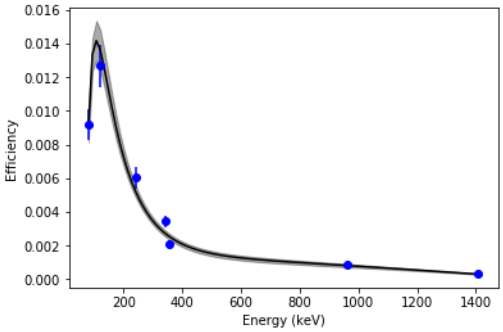

(a) LAB CPG - SATLAS fit of the efficiency curve for 1 mm Al and 25 mm distance

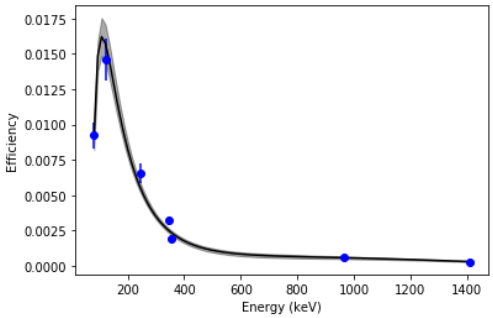

(b) LAB CPG - SATLAS fit of the efficiency curve for 3 mm Al and 25 mm distance

Figure 7.9 Comparison of the Resolution of the SDP500S detector for different distance and aluminium thickness.

without aluminium foil in front of the detector. The difference between the calculated activity and the actual activity does not exceed 10% for both Ba-133 and Eu-152 sources, which is within the source activity uncertainties.

Table 7.6 Comparison between calculated and Actual Activity with LAB CPG detector

Source	**Calculated Activity (Bq)**	**Actual Activity (Bq)**	**Activity Uncertainty** (%)	**Difference in** (%)
Ba-133	1.32 E04	1.42 E04	10	7.3
Eu-152	1.93 E04	1.76 E04	10	9.9

7.2.2 Energy Resolution of LAB CPG detector

In this section, the energy resolution of the LAB CPG detector is studied as a function of the energy. Both the effects of different distance and aluminium thickness were explored in a similar way as for the SDP500S detector, as it can be observed from Figures 7.10a and 7.10b. It can be seen that the energy resolution in this case is not increasing in value with higher energies, contrary to the SDP500S detector.

What is also important to notice is that the energy resolution of LAB CPG detector is inferior to the SDP500S detector, according to Figure 7.11. The results for the resolution

were for the same distance from the Eu-152 source (25 mm), without aluminium foil in between.

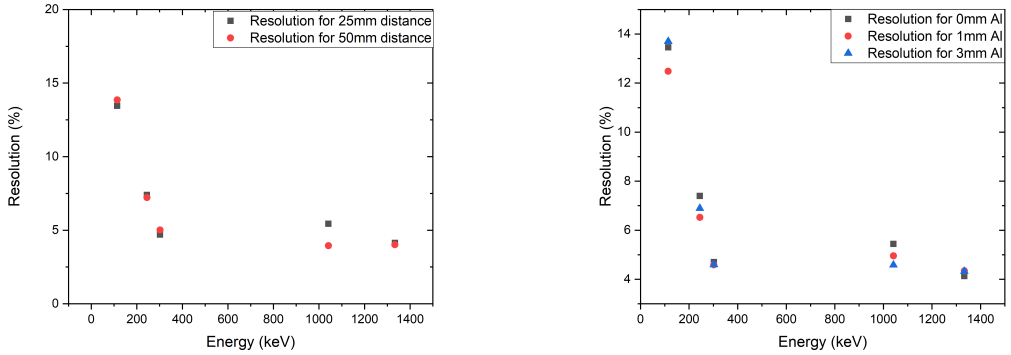

(a) LAB CPG resolution for 25mm and 50mm distance versus the energy

(b) LAB CPG resolution for different Al thickness versus the energy

Figure 7.10 Comparison of the energy resolution of the LAB CPG detector for different distance and aluminium thickness.

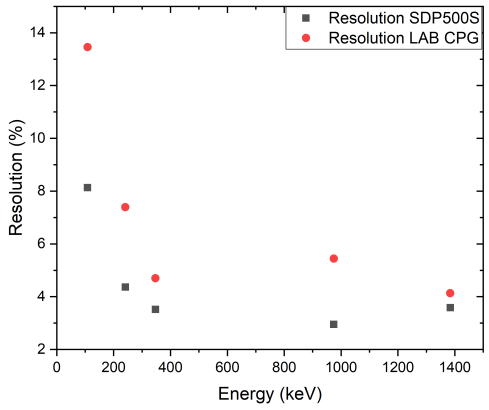

Figure 7.11 Comparison of the energy resolution as a function of the energies from the Eu-152 source for SDP500S and LAB CPG detectors.

7.2.3 Peak to Compton ratio for LAB CPG detector

In this section, the Peak to Compton ratio for LAB CPG CZT detector was calculated from the spectra of Eu-152 for the distance of 50 mm and without an aluminium foil in between (apart from the one of the casing). The P/C ratio was calculated in the same manner as for SDP500S, that was presented in a previous section. The results are presented in Table 7.7.

Table 7.7 Peak to Compton Ratio LAB CPG detector without Al foil

Source	Energy (keV)	Distance (mm)	Peak to Compton Ratio
Eu-152	244.7	50.00	1.32
	344.3	50.00	3.31
	964.1	50.00	1.19
	1408.0	50.00	5.64

7.2.4 Count rate of LAB CPG detector

In this section, the count rate of LAB CPG detector is calculated. As it can be observed from Figure 7.12, the decay time τ of the preamplifed signal is 33.9μs. So the full signal time is about 3τ, so equal to around 100 μs. Therefore, the count rate is around 10000 counts/s for the LAB CPG detector. Therefore, the two models, LAB CPG and SDP500S, have similar count rates. According to the manufacturer, the GR-1 detector has a count rate of the same order with SDP500S and LAB CPG CZT detectors, of around 30000 counts/s.

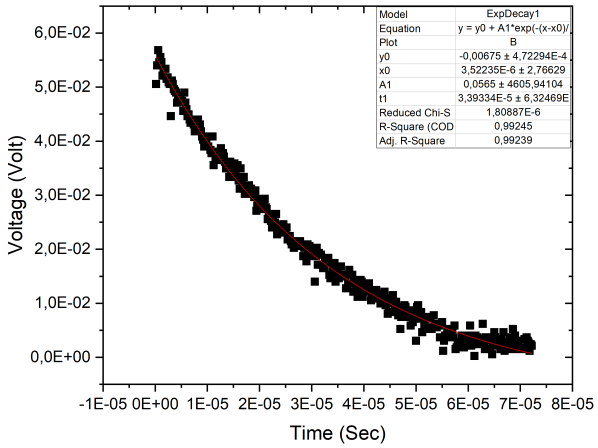

Figure 7.12 Exponential fit of the preamplified signal's tail from LAB CPG detector.

7.3 Single Point Extended Area Radiation detector

Single Point Extended Area Radiation detector (SPEAR) is a detector probe from KROMEK, that consists of a $5 \times 5 \times 5mm^3$ CZT crystal and a low noise hybrid preamplifier. The aluminium casing is just 13 mm diameter x 89 mm in length.

SPEAR detector employs the CAPture technology, which according to the manufacturer, is improving the charge collection efficiency. Therefore, it is supposed to provide good photopeak efficiency and peak to valley ratio while reducing the tailing, thus offering a probe suitable for isotope identification and quantification. In Figure 7.13a, the design of the detector is presented.

The spectra from SPEAR detector could not be analysed in a similar way as the rest of the aforementioned detectors due to low statistics. An example of the γ-ray spectrum is presented in Figure 7.13b. It can be seen that even though the time of the measurement is the same as for the other detectors (5 minutes) the peaks of the spectrum cannot be easily distinguished.

(a) SPEAR. Ref. KROMEK

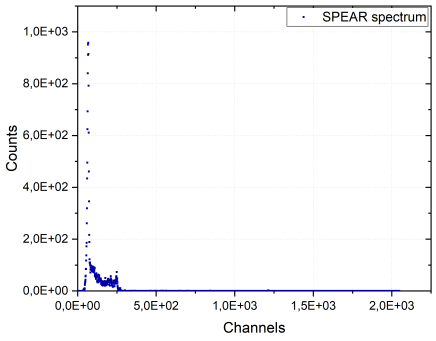

(b) Ba-133 spectrum using SPEAR

Figure 7.13 (left) SPEAR detector and (right) Ba-133 spectrum gained by using this detector

7.4 Comparison of GR-1, SDP500S and LAB CPG detectors

In this section, the comparison between the efficiencies of the three different CZT detectors, SDP500S, LAB CPG and GR-1, is presented. It is possible to compare their efficiencies only considering the common distance of 84 mm from the Eu-152 source. However, the effect of the glass and the golden foil are not taken into account in the case of SDP500S and LAB CPG detectors, since they were not tested in the MEDICIS facility but in Complutense University of Madrid.

Indeed, Figure 7.14 depicts the efficiencies of these three detectors. It is clear that LAB CPG detector provides higher efficiency for the lower energies than the other two detectors. For the lower energy of 121.8 keV the big difference between the efficiencies of GR-1 and the other two detectors can be attributed to the fact that the experimental setup for GR-1 is different since it includes more materials in between. Indeed, there is no window and golden foil between the source and the LAB CPG and the SDP500S detectors. For the rest of the energies the efficiencies of the three detectors are comparable, regardless of the difference in the setup.

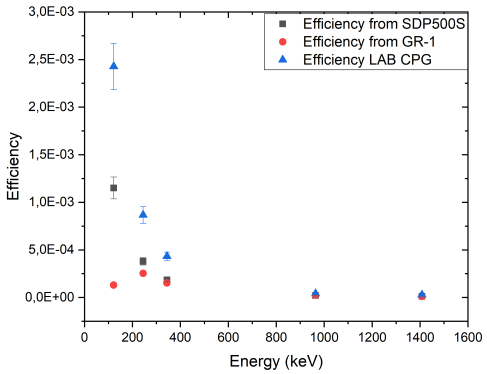

Figure 7.14 Comparison of the efficiencies as a function of the energies from the Eu-152 source for SDP500S, LAB CPG and GR-1 CZT detectors.

7.5 Conclusions

From the above analysis of the aforementioned detector probes (SDP500S, LAB CPG and SPEAR detectors), it is concluded that SDP500S and LAB CPG detectors are good alternatives for the GR-1 KROMEK CZT detector due to their high resolution and efficiency values. LAB CPG detector proved to provide higher efficiency values (especially for the lower energies) than the SDP500S detector for the same experimental configuration (distance of 84mm, no aluminium foil in between and same Eu-152 source and live times of 19 hours). However, SDP500S detector proved to provide better energy resolution from LAB CPG detector. Both of these detectors gave a good approximation of the activity for the certified sources that were used during the experimental process in the laboratory of Complutense University of Madrid. The difference between the actual activity and the calculated one using the least chi-squared fitting routine from SATLAS package in Python did not exceed 10% in all cases except for Ba-133 with SDP500S detector with 13% difference. Moreover, both SDP500S and LAB CPG detectors provided approximately the same count rate capability of 10000 counts/sec and a good Peak to Compton Ratio.

On the other hand, SPEAR detector is not suitable for online activity measurements, since it does not provide spectra with acceptable resolution.

Chapter Eight

Simulations

In this chapter, simulations using Monte Carlo methods with PENMAIN are described and performed. The objective of these calculations is to try to match the simulated results to the experimental results in order to be able to use the PENMAIN to simulate reliably any new situation at MEDICIS, for instance changing the distance, moving the detector around, changing the collection foil, adding a layer and putting the detector at an angle. Furthermore, it is possible to calculate the accumulated dose in the collection foil for different radioisotopes.

8.1 Monte Carlo Simulation

The term "Monte Carlo" was first used to name the numerical methods applied to solve complicated mathematical and physical projects during the nuclear weapon project in Los Alamos. Since then, Monte Carlo simulations have been applied to face a variety of physical and mathematical problems, especially those that include systems with many coupled degrees of freedom.

During a Monte Carlo simulation of a particle moving into a medium, the movement is consisted of a random sequence of tracks, finally leading to an interaction of the particle with the medium. Therefore, there is loss of energy, change of direction and, sometimes,

production of secondary particles. Thus, Monte Carlo simulations are responsible for the generation of random tracks of particles. For this purpose, it is necessary to apply an interaction model, or else, a database of differential cross sections in order to simulate the different ways of interaction. The interaction model sets the probability distribution functions (PDF) of the parameters that determine the track, such as the free path, the interaction type, the loss of energy and the angular deflection of the particle after the interaction. Afterwards, sampling methods will be applied in order to generate tracks using the known probability distribution functions (Salvat, Fernandez-Varea, and Sempau, 2011).

8.2 PENELOPE Simulation

In this thesis, all the simulations were performed using the Monte Carlo simulation package; PENELOPE 2011 version (Salvat, Fernandez-Varea, and Sempau, 2011).

PENELOPE is an acronym for "PENenetration and Energy LOss of Positrons and Electrons". As the name suggests, it was initially created to simulate the energy loss of positron and electrons. Later, the energy loss calculation for photons was added. The model that is being used for these calculations is the scattering model with the use of analytical cross section models for the various mechanisms of interaction (Peyres and a-Tora, 2007).

The kinetic energies of electrons and positrons that can be simulated range between 50 eV to 1 GeV.

The scattering model is being used in combination with the analytical cross section models for the various mechanisms of interaction. The secondary particles are simulated when the primary track is completed.

8.2.1 Penmain

Penmain routine is included in the PENELOPE distribution package as a main generic program providing simplicity for the user by working as a black box for the simulations.

It is user friendly as it does not require from the user to write their own program. PENMAIN was utilized in order to create a simulation based on the geometry subroutine package PENGEOM. PENGEOM is responsible for tracking particles in materials that include homogeneous bodies. These regions are constrained by quadratic surfaces. PENMAIN enables the study of the effect of different types of irradiation on detectors of geometries and materials, which are chosen by the user.

In order for PENMAIN to work properly, it is crucial for the user to provide an input file that includes all the necessary information about the simulation. In the next paragraphs the methodology process is described.

8.2.2 Methodology

First, it is necessary to create the material files, which have .mat extension. In PENMAIN this is possible to create with the command "./material" from the ./mat directory. Once the program is executed the user is able to name the material to enter the stoichiometric formula, atomic number, as well as the stoichiometric coefficients of each of the constituents of the material. It is also possible to change the ionization energies, if this is deemed necessary. Finally, the user can specify the density of the material and save the file.

Next step is to create a geometry file, which has the .geo extension. A program that converts a simple input file into a .geo file was utilized. The command is "./obj-geo file.in name.geo". An example of a input file for the geometry of the experiment in MEDICIS is shown in Figure 8.1.

As it can be seen from Figure 8.1, each line defines one body of the system. The first letter corresponds to the type of coordinate system (rectangular “R”, cylindrical “C” or spherical “S”), the first number of the line refers to the order of the body in the input and the next three numbers are the *center* of the body in Cartesian coordinates (x, y, z). The next three depend on the type of coordinates; if the coordinates are Cartesian, then they correspond to

```
!WRITE ONE OBJECT PER LINE. FILE END WITH A STARTING CHARATER NOT VALID FOR TYPE
R 1 0.0 0.0 0.015 0.3 0.3 0.03 0 0
R 2 0.0 0.0 3.53 10.0 10.0 7.0 0 0
R 3 0.0 0.0 7.21 7.5 7.5 0.36 0 0
R 4 0.0 0.0 7.89 8.0 8.0 1.0 0 0
R 5 0.0 0.0 8.475 1.0 1.0 0.17 0 0
R 6 0.0 0.0 8.81 1.0 1.0 0.5 0 0
R 7 0.0 0.0 9.56 1.0 1.0 1.0 0 0 0
!WRITE ONE OBJECT PER LINE. FILE END WITH A STARTING CHARATER NOT VALID FOR TYPE
```

Figure 8.1 Example of the input that was converted in a .geo file. This file is depicting the experimental configuration of MEDICIS.

the sides of the rectangle. If the coordinates are cylindrical, then the numbers correspond to the inner, outer and height of the cylinder. Lastly, if the coordinates are spherical, then the numbers correspond to the inner and outer radius of the sphere (the third number does not have any effect).

After defining the material and the geometry of the configuration that the user desires to simulate, the next step is to create the input file to implement all the necessary parameters together.

Input

PENMAIN's operation is entirely dependant from the input data files. A guideline on all the possible commands in the input file is shown in Figure A.3 in the Appendix.

The input file used for simulating the GR-1 CZT detector from KROMEK in the geometry configuration of the experimental setup of MEDICIS is shown in Figure 8.2.

As it can be seen from Figure A.3, first line of the input file is the Title. Then, the source is defined through a series of commands like SKPAR, SENERG, SPOSIT, SCONE etc. More details about these commands are given in Reference: (Salvat, Fernandez-Varea, and Sempau, 2011).

Briefly, the most important commands are described:

- SKPAR: The user is able to choose the kind of primary particle.
- SENERG: The initial energy of the photons can be defined.

```
TITLE  MEDICIS.
       .
       >>>>>>>> Source definition.
SKPAR  2             [Primary particles: 1=electron, 2=photon, 3=positron]
SENERG 6.61e5
SPOSIT 0.0 0.0 0.0                            [Coordinates of the source]
SCONE  0.0 0.0 10.0                          [Conical beam; angles in deg]
       .
       >>>>>>>> Material data and simulation parameters.
MFNAME mat/gold.mat                          [Material file, up to 20 chars]
MFNAME mat/air.mat                           [Material file, up to 20 chars]
MFNAME mat/glass.mat                         [Material file, up to 20 chars]
MFNAME mat/air.mat                           [Material file, up to 20 chars]
MFNAME mat/Al.mat                            [Material file, up to 20 chars]
MFNAME mat/air.mat                           [Material file, up to 20 chars]
MFNAME mat/czt.mat                           [Material file, up to 20 chars]
       .
       >>>>>>>> Geometry definition file.
GEOMFN geo/medicis.geo
       .
       >>>>>>>> Emerging particles. Energy and angular distributions.
NBE    0.15e5 1.5e6 1000                     [Energy window and no. of bins]
NBANGL 180 180                  [No. of bins for the angles THETA and PHI]
       .
       >>>>>>>> Impact detectors (up to 25).
IMPDET 0.15e5 1.5e6 1000 0 2
IDBODY 7                              [Active body; one line for each body]
       .
       >>>>>>>> Energy deposition detectors (up to 25).
ENDETC 0.15e5 1.5e6 1000                 [Energy window and number of bins]
EDBODY 7                              [Active body; one line for each body]
       .
       >>>>>>>> Dose Calculation.
GRIDX  10.00 -10.00                [X coordinates of the dose box vertices]
GRIDY  10.00 -10.00                [Y coordinates of the dose box vertices]
GRIDZ  10.00 -10.00                [Z coordinates of the dose box vertices]
GRIDBN 55 55 55                                          [Number of bins]
       .
       >>>>>>>> Job properties
NSIMSH 1e5                            [Desired number of simulated showers]
TIME   2e9                               [Allotted simulation time, in sec]
       .
END                                        [Ends the reading of input data]
```

Figure 8.2 PENMAIN input file for the simulation of GR-1 CZT detector at MEDICIS

- SPOSIT: The position of the source is defined by giving the coordinates of the center of the volume of the source.

- SCONE: In the case of a conical source beam this command determines the angles of the emission. In particular, the user can define the θ, ϕ (which are the cone aperture angles) and the α angle that defines whether the source is mono-directional (if $\alpha = 0$) or isotropic (if $\alpha = 180$).

Afterwards, the material data and simulation parameters, as well as the geometry, are defined in the input file. It is important to note that the materials should be presented in the same order as the corresponding bodies in the geometry file in order for the bodies to

be assigned with the desired material.

Finally, the user can define the number of events and maximum job time needed for the simulation. This is possible with the NSIMSH command, which in our case is $1e5$ stories (or else, simulated showers). For the maximum job time, a very large number is usually used so that the simulation is not interrupted. In this case, it is set to 2E9 seconds.

Geometry

For the KROMEK CZT GR-1 detector the following specifications were taken into account when simulating with PENELOPE: The GR-1 unit contains a one-centimetre cube of CZT, a preamplifier, a shaping amplifier, baseline restorer, pulse height digitizer and HV in a metal case with the size of 25 mm x 25 mm x 63 mm. For the CZT crystal, it is known that it has dimensions of $10 \times 10 \times 10mm^3$. The concentration of each constituent of the crystal is assumed to be $Cd_{0.9}Zn_{0.1}Te$ according to Reference (Sordo et al., 2009).

The geometry files in PENMAIN have the .geo extension. For the visualisation of the geometry, the $gview2d.exe$ was employed. As the name suggests, $gview2d$ is able to visualise the geometry given by the .geo files in 2D. This is very helpful in order to make sure that the correct experimental configuration was used.

In Figure 8.3, the geometry of MEDICIS operation used for the simulations is demonstrated thanks to $gview2d$.

The order of the materials is the one presented in the material section in Figure 8.2. In particular, the thin purple box is the golden foil, the big orange one represents the air, the electric blue box is the glass of the collection window, the green box is again the air, the red box the aluminium casing of the detector, the light blue is the air between the aluminium casing and the CZT crystal. Finally, the ochre box is the CZT crystal.

Furthermore, the geometries have been taken from the specifications by the manufactures. In particular, those for the GR-1 CZT detector, which is of key importance for MEDICIS operation, have been taken from (Kromek, 2020). Nevertheless the initial simulations and

cross-check of the efficiencies were not able to reproduce the experimental results. Several systematic tests have been performed to understand the possible source of this discrepancy, including modifications in the casing thicknesses, the detector dimensions and the distance to the end cap. A good agreement has been obtained by reducing the active volume of the detector from $10x10x10mm^3$ to 9 x 9 x 9 mm^3, which is a large variation of about 27%. This effect has been already discussed in Reference (Tajudin et al., 2019) with a similar detector of GR-1 CZT KROMEK type. In this paper the authors showed that the effective volume of the crystal seemed to be as small as 8 x 8 x 8 mm^3. According to (Tajudin et al., 2019) the simulation implemented the following parameters: the casing dimensions were of 1.2 mm thick aluminium case and 0.5 mm for the aluminium window. Moreover, the distance from the window to the surface of the crystals is 5 mm. With this changes it was possible to reconcile the simulations to the actual experimental results.

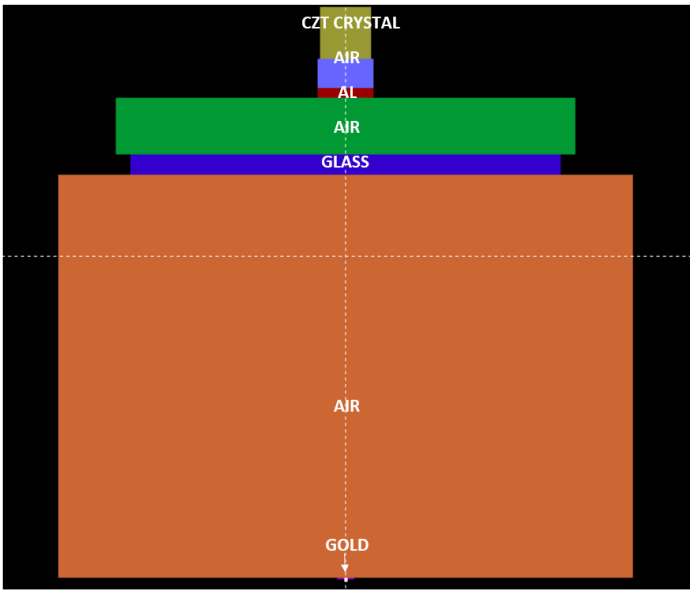

Figure 8.3 Geometry of experiment using *gview2d*

Output files

Three different types of detectors are described in the code so that to provide a variety of parameters and distributions:

- Impact detectors: The main characteristics of the particles coming in the detector are recorded.

- Energy deposition detectors: The energy of a particle that is deposited in the detector is recorded.

- Dose enclosure: To record the dose distribution within a specific system volume.

Two general types of files are produced:

- Files with the main parameters of the simulation and several useful information, such as average values (*penmain.dat*)

- Files with space or energy distribution for various parameters, such as energy distribution of the deposited energy on a detector ($spc.enddet - .dat$)

In this thesis, the energy deposition detector was used. The output file of the energy deposition spectrum has the title "$spc.enddet - 01.dat$" and it showcases the distribution of absorbed energy in the detector. This is possible through a histogram of the probability distribution function (per eV and per initial particle). The $spc.enddet - .dat$ file consists of three columns. The first column is the energy of the particles in eV, the second column is the probability density in $\frac{1}{eV \times particle}$ and the third column is the statistical uncertainty (of the order of 3σ).

In order to get the full energy peak (FEP) efficiency it is necessary to multiply the probability distribution function (second column of the $spc.enddet - .dat$) file by the energy width of the bin. Then, it is necessary to scale for the solid angle corresponding to the chosen cone aperture in the simulation.

8.3 Simulation results

In this section, the results from the simulations for the GR-1 and GR-05 CZT detectors from KROMEK are presented, analysed and discussed. In particular, it was possible to simulate the results for the efficiency of these detectors for the experimental configuration of MEDICIS. The simulated results were then compared to the experimental ones, fitted using the fit from SATLAS package in Python, to check if the calculation of the activity is feasible and compared with the actual values of activity of the sources on the day of the measurement. The simulations gave an insight on the effect of the distance and thickness of the materials in front of the detector on the simulated efficiency and consequently on the simulated activity.

8.3.1 Simulation of GR-1 CZT detector for the middle position

In Figure 8.4a, the comparison between the simulated and experimental efficiency of GR-1 CZT that was set aligned with the center of the window of the collection chamber in MEDICIS can be seen. It can be easily noticed that the simulation gives a good approximation of the experimental values with slightly bigger deviation for the lower energies.

The relative difference between the experimental and simulated efficiencies can be seen in Table 8.1. The uncertainties are not visible because of their small value. It should be noted that the simulated crystal has a volume of $0.9 \times 0.9 \times 0.9 cm^3$. For a volume: $1 \times 1 \times 1 cm^3$ the percentage difference reaches 60%. However, for the $0.9 \times 0.9 \times 0.9 cm^3$ crystal the percentage difference ranges from 1.7% to 30%.

In Figure 8.4b, the fit of the simulated efficiency curve for the middle position of GR-1 in MEDICIS can be observed. In Table 8.2, the parameters of the fit using SATLAS package in Python are presented.

Table 8.1 Comparison between Simulated and Experimental Efficiency for the middle position of the detector

Energy (keV)	**Simulated Efficiency**	**Uncertainty**	**Experiment Efficiency**	**Difference** (%)
121.8	1.01 E-04	0.01 E-04	1.31 E-04	23
244.7	2.16 E-04	0.01 E-04	2.54 E-04	15
276.4	1.88 E-04	0.01 E-04	1.45 E-04	29
302.9	1.67 E-04	0.01 E-04	1.63 E-04	2
344.3	1.32 E-04	0.01 E-04	1.52 E-04	13
356.0	1.22 E-04	0.01 E-04	1.24 E-04	1.7
383.8	1.06 E-04	0.01 E-04	8.62 E-05	22
661.7	4.33 E-05	0.04 E-05	3.66 E-05	18
778.9	3.59 E-05	0.04 E-05	2.92 E-05	9.8
964.1	2.36 E-05	0.03 E-05	2.85 E-05	16
1173.5	1.70 E-05	0.03 E-05	1.42 E-05	20
1333.2	1.47 E-05	0.03 E-05	1.15 E-05	28
1408.0	1.22 E-05	0.03 E-05	1.15 E-05	5.8

Table 8.2 Fitting Parameters for the middle position of the detector using simulated efficiency values

Fitting Parameters	**Values of the Parameters**	**Uncertainty of Parameters**
a_1	-2.504E01	$\pm 7.137E-01$
a_2	1.604E01	$\pm 4.816E-01$
a_3	-3.818	$\pm 1.209E-01$
a_4	$4.015E-01$	$\pm 1.339E-01$
a_5	-1.576$E-02$	$\pm 5.528E-04$

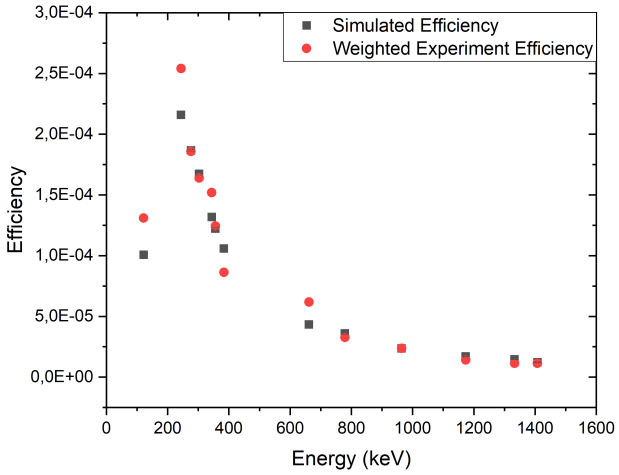

(a) Comparison between the simulated and experimental efficiency and their uncertainties for GR-1

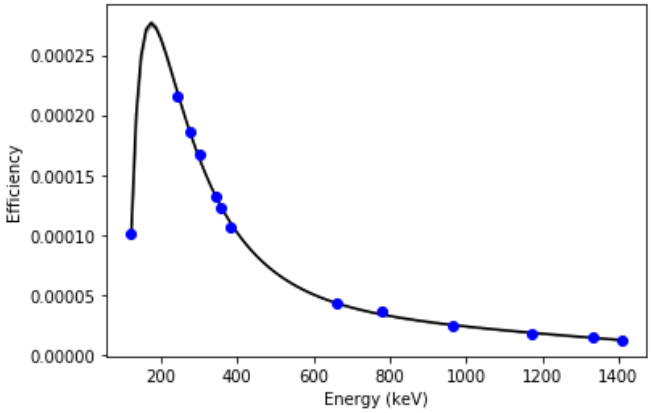

(b) Fit of the Simulated Efficiency curve for GR-1

Figure 8.4 Efficiency curve for the Simulated Efficiency of GR-1 CZT detector in the middle position of the configuration in MEDICIS.

Calculation of the Activity from the Simulated Efficiency Curve

In this section, the calculation of the activity is performed from the SATLAS fit of the simulated efficiency curve as shown in Figure 8.4b. In Table 8.3, the comparison between the simulated and the actual activity of Ba-133, Eu-152, Co-60 and Cs-137 for the middle position of the GR-1 detector are presented. As it can be seen from the small percentage difference, the activity can be calculated with a good approximation. The only source that

exceeds the 10% difference is Eu-152.

Table 8.3 Comparison between Simulated and Actual Activity for the middle position of the detector

Source	Simulated Activity (Bq)	Actual Activity (Bq)	Difference in (%)
Ba-133	5.97 E05	5.69 E05	4.8
Eu-152	4.38 E04	3.68 E04	19
Co-60	2.86 E04	2.98 E04	3.9
Cs-137	3.13 E04	2.96 E04	5.8

8.3.2 Simulation of GR-1 CZT detector for the lower position

In Figure 8.5a, the comparison between the simulated and experimental efficiency of GR-1 CZT in the lower position is presented. Also Figure 8.5b shows the fit of the Simulated efficiency curve for the lower position of the GR-1 CZT detector. The fit was done using SATLAS Python package.

In Figure 8.6, the comparison between the two simulations of the different positions of the GR-1 detector is presented. As it can be seen the efficiencies are similar for the middle and the lower position.

In Table 8.4, the comparison between the simulated and the actual experimental Efficiency for the lower position of the detector in MEDICIS is presented. The GR-1 detector is situated 1.25 cm below the center of the collection window. Again, the GR-1 detector in the simulation has a volume crystal of $0.9 \times 0.9 \times 0.9 cm^3$. The difference between the experimental values and the simulated ones ranges from 0.1% to 34%.

Calculation of the Activity from the Simulated Efficiency Curve for the lower position of GR-1

In this section, the calculation of the activity is performed from the least chi-square fit using SATLAS package from Python of the simulated efficiency curve as shown in Figure 8.5b.

Table 8.4 Comparison between Simulated and Experimental Efficiency for the lower position of the detector

Energy (keV)	**Simulated Efficiency**	**Uncertainty**	**Experiment Efficiency**	**Difference in (%)**
121.8	1.075 E-04	0.001 E-04	1.284 E-04	16
244.7	2.200 E-04	0.002 E-04	2.625 E-04	16
276.4	2.100 E-04	0.002 E-04	1.954 E-04	7.9
302.8	1.725 E-04	0.002 E-04	1.768 E-04	2.4
344.2	1.437 E-04	0.001 E-04	1.577 E-04	8.7
356.0	1.300 E-04	0.001 E-04	1.358 E-04	4.3
383.8	1.050 E-04	0.001 E-04	1.048 E-04	0.1
661.7	3.750 E-05	0.008 E-05	3.778 E-05	0.7
778.9	3.750 E-05	0.008 E-05	3.019 E-05	24
964.1	2.990 E-05	0.007 E-05	2.221 E-05	34
1173.5	1.490 E-05	0.005 E-05	1.846 E-05	19
1333.3	1.990 E-05	0.006 E-05	1.595 E-05	25
1408.0	1.250 E-05	0.005 E-05	1.252 E-05	0.2

Table 8.5 Fitting Parameters for the lower position of the detector using simulated efficiency values

Fitting Parameters	**Values of the Parameters**	**Uncertainty of Parameters**
a_1	-2.892E01	$\pm 1.285E-01$
a_2	1.855E01	$\pm 8.673E-02$
a_3	-4.419	$\pm 2.178E-02$
a_4	$4.648E-01$	$\pm 2.415E-03$
a_5	-1.824$E-02$	$\pm 9.966E-05$

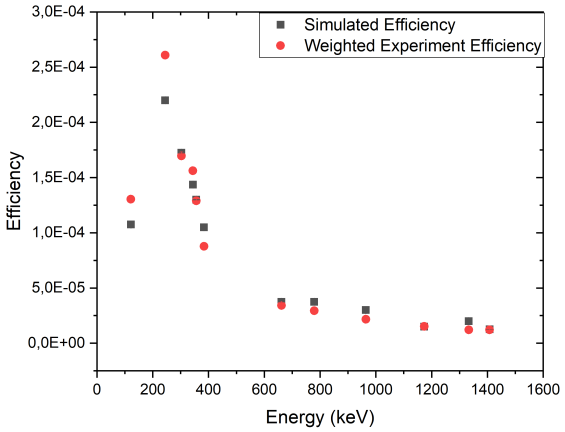

(a) Comparison between the simulated and experimental efficiency and their uncertainties for the lower position of the GR-1 detector

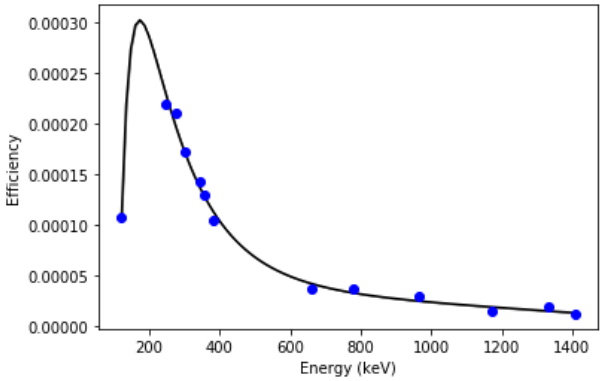

(b) Fit of the Simulated Efficiency curve for the lower position of GR-1

Figure 8.5 Efficiency curve for the Simulated Efficiency of GR-1 CZT detector in the lower position of the configuration in MEDICIS.

In Table 8.6, the comparison between the simulated and the actual activity of Ba-133, Eu-152, Co-60 and Cs-137 for the lower position of the GR-1 detector are presented. As it can be seen from the small percentage difference, the activity can be calculated with a good approximation. The only sources whose activity exceed the 10% relative difference from the experimental values are Eu-152 and Co-60.

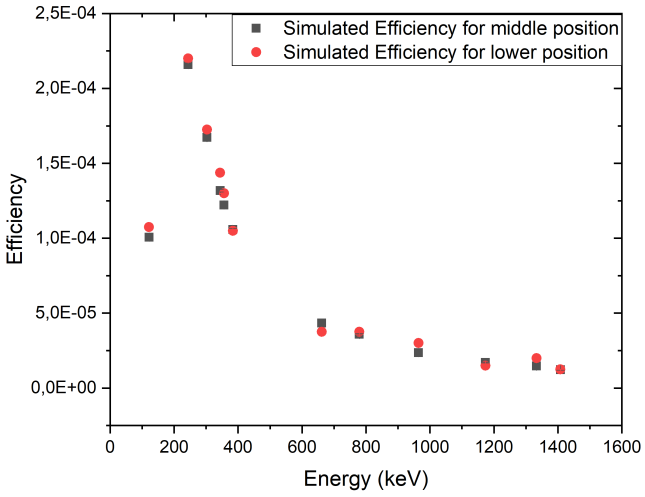

Figure 8.6 Comparison between the two simulations with their uncertainties for the different positions of the detector (middle and lower position of GR-1)

Table 8.6 Comparison between Simulated and Actual Activity for the lower position of GR-1 detector

Source	Simulated Activity (Bq)	Actual Activity (Bq)	Difference in (%)
Ba-133	5.62 E05	5.67 E05	0.9
Eu-152	4.26 E04	3.66 E04	16
Co-60	3.28 E04	2.95 E04	11
Cs-137	2.76 E04	2.95 E04	6.7

8.3.3 Simulation of GR-05 CZT detector

In this section, GR-05 CZT detector was simulated and compared with the experimental values. It should be noted that in order to get a good estimation of the experimental values, of the order shown in Table 8.7, the volume of the CZT crystal was selected to be $0.45 \times 0.45 \times 0.45 cm^3$. The difference between the experimental and simulated values ranges from 0.6% to 26%.

661,6 121,8 244,7 344,3 778,9 964,1 1408

As it can be seen in Figure 8.7a, the simulated efficiencies have really close values to the experimental ones especially for the higher energies. The biggest deviation from the

Table 8.7 Comparison between Simulated and Experimental Efficiency for GR-05 detector

Energy (keV)	Simulated Efficiency	Uncertainty	Experiment Efficiency	Difference in (%)
121.8	2.53 E-05	0.04 E-05	3.41 E-05	26
244.7	3.17 E-05	0.04 E-05	3.86 E-05	18
344.3	1.89 E-05	0.03 E-05	1.96 E-05	3.3
661.7	4.33 E-06	0.15 E-06	3.71 E-05	17
778.9	2.96 E-06	0.13 E-06	2.76 E-05	7.5
964.1	1.90 E-06	0.10 E-06	2.07 E-05	8.3
1408.0	8.36 E-07	0.67 E-07	8.31 E-07	0.6

experimental values is observed for the lower energies. This could be attributed to the self-absorption process in the source for the low-energy photons. This effect has been previously observed in (Issam et al., 2018) and (Salgado et al., 2012). Furthermore, the presence of the materials of gold and aluminium is enhancing the phenomenon of the self-absorption of low-energy γ-rays.

Furthermore, a comparison between the simulated values of the efficiencies for the GR-1 and the GR-05 detectors is depicted in Figure 8.7b. It is clear that for the same simulated configuration, the GR-1 detector provides higher efficiency for different energies than the GR-05, as it was experimentally proven and, of course expected, due to the bigger CZT volume.

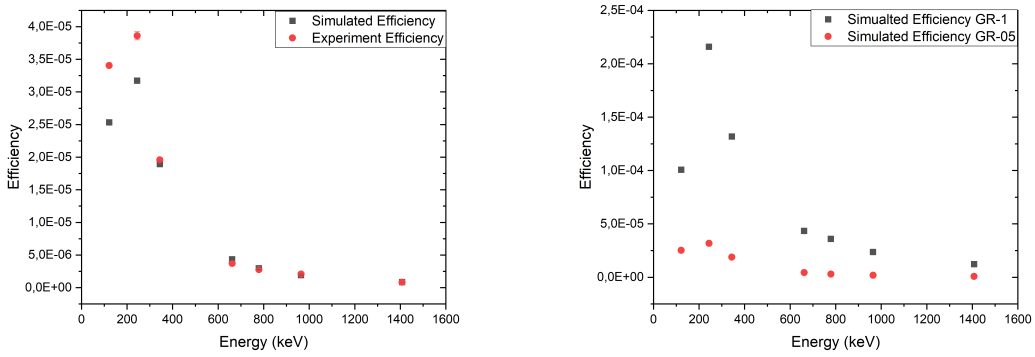

(a) Simulated Efficiencies of GR-05 detector

(b) Comparison of simulated Efficiencies of GR-05 and GR-1 detectors

Figure 8.7 Simulated Efficiencies of GR-05 and comparison with GR-1 detector

8.3.4 Simulation of SDP500S CZT detector

In this section, the simulation of the SDP500S CZT detector is performed using PENMAIN. The simulations recreated the laboratory configuration performed at Complutense University of Madrid. For the geometry of the detector, the specifications of the manufacturer, shown in Figure 7.2, were followed. In particular, the Aluminium casing was selected to be 0.1 cm, the air between the aluminium casing and the CZT crystal was selected to be 0.68cm and the CZT crystal was $1 \times 1 \times 0.5 cm^3$. The results of the simulation, as well as the comparison with the experimental value of the efficiency of the detector, are presented in Table 8.8. The simulation results in Table 8.8 are for 25 mm distance of the SDP500S detector from Eu-152 without an aluminium foil in between. Furthermore, the same procedure was followed for the simulation of the SDP500S detector for the distance of 84 mm for the sources of Eu-152. These results are presented in Table 8.9. From Tables 8.8 and 8.9, it can be concluded that the simulations give a good approximation of the experimental values of the efficiency regardless of the distance of the detector. The relative difference for both cases is not exceeding 27%.

Table 8.8 Comparison between Simulated and Experimental Efficiency for SDP500S detector for 25 mm distance

Energy (keV)	**Simulated Efficiency**	**Sim. Eff. Uncert.**	**Experiment Efficiency**	**Exp. Eff. Uncert.**	**Difference (%)**
244.7	2.19 E-03	0.049 E-03	2.87 E-03	0.29 E-03	24
344.3	1.04 E-03	0.023 E-03	1.31 E-03	0.13 E-03	20
778.9	1.93 E-04	0.043 E-04	1.95 E-04	0.23 E-04	1.1
964.1	1.37 E-04	0.031 E-04	1.52 E-04	0.18 E-04	9.6
1408.0	6.99 E-05	0.16 E-05	8.37 E-05	0.89 E-05	17

Table 8.9 Comparison between Simulated and Experimental Efficiency for SDP500S detector for 84 mm distance

Energy (keV)	Simulated Efficiency	Sim. Eff. Uncert.	Experiment Efficiency	Exp. Eff. Uncert.	Difference (%)
244.7	2.92 E-04	0.26 E-04	3.79 E-04	0.38 E-04	23
344.3	1.43 E-04	0.13 E-04	1.84 E-04	0.18 E-04	23
778.9	2.68 E-05	0.24 E-05	2.78 E-05	0.29 E-05	3.4
964.1	1.77 E-05	0.16 E-05	2.04 E-05	0.23 E-05	13
1408.0	9.20 E-06	0.82 E-06	1.26 E-05	0.13 E-05	27

8.4 Conclusions

In conclusion, PENMAIN simulations allowed to reproduce the experimental measurements successfully with small relative difference. Furthermore, the simulations verified the fact that the slightly lower position of the GR-1 detector (1.25 cm below the center of the collection window) affect the efficiency values negligibly. Therefore, GR-1 detector can be located 1.25 cm below the center of the window of the collection chamber with no noticeable effect on its efficiency. Thus, it is possible to calculate the activity of the produced radioisotope successfully, while leaving space for other instruments to be located at the center of the window, such as a camera.

Additionally, the simulations correctly take into account the materials between the detectors and the radioactive sources, such as the golden foil, the window of the collection chamber (borosilicate glass) as well as the aluminium casing of the detector. That leads to the conclusion that collection foils of any type can be simulated and the effect of different materials to the results of the simulation can be studied. Moreover, the bigger percentage difference between the simulated and the experimental values for the lower energies could be attributed to the self-absorption of low-energy γ-rays due to the presence of the materials of gold and aluminium.

Also, the simulations allowed to reproduce the results for GR-05 CZT detector and compare the results not only with the experimental ones but also with the simulated results for the GR-1 CZT detector. It is important to notice that for GR-1 CZT detector the volume of

the detector was selected to be $0.9 \times 0.9 \times 0.9 cm^3$, while the volume of the GR-05 detector was selected to be $0.45 \times 0.45 \times 0.45 cm^3$ in order to acquire results close to the experimental ones. Furthermore, it was verified with the simulations that for the same geometrical experimental configuration, the GR-1 detector provides higher efficiency for than the GR-05 detector, as it was expected due to difference in the size of the CZT crystal.

An inactive layer of the CZT crystal could explain the difference of the size of the CZT crystal between the simulations and the experiment for the GR-1 and GR-05 models. On the other hand, when SDP500S detector was simulated, the true volume of the detector was used in the simulations, yielding results close to the experimental ones.

Moreover, the simulations for SDP500S work at several distances without any issue. Therefore, it is possible to safely design a movable system for the measurements at MEDICIS facility, where the efficiency at several distances from the window of the chamber can be calculated with maximum uncertainty of the order of 30%.

Chapter Nine

Dose Calculation

The aim in this section is to assess, with Nucleonica (Nucleonica, 2011) the expected dose rate (beta and gamma) on the foils at distances of interest for radiation protection i.e. “contact” (which can never be calculated since it would give a dose at infinity, therefore it was the "in contact" distance was chosen as 0.1 cm), 1 cm, 10 cm and 40 cm for the different radionuclides of interest for MEDICIS, which are depicted in Table 2 of Ref. (Augusto et al., 2014). Nucleonica is a nuclear science web portal, which was originally made by the European Commission’s Joint Research Centre (Masterson, 2017). Currently, it belongs to company "Nucleonica GmbH" (Nucleonica, 2011).

For photons the dose rate is calculated using equation 9.1, where A is the activity of the source in Becquerel, E is the energy of the photons in MeV, d is the distance from the source in cm and P is the probability of emission.

$$H^o(\mu Sv/h) = 1.6 \times 10^{-10} \times 10^6 \times 3600 \times E(MeV) \times \frac{A(Bq) \times P}{4\pi d^2} \frac{\mu_e(cm^2 g^{-1})}{\rho} \tag{9.1}$$

which leads to:

$$H^o(\mu Sv/h) = 4.584 \times 10^{-2} \times E(MeV) \times \frac{A(Bq) \times P}{d^2} \frac{\mu_e(cm^2 g^{-1})}{\rho} \tag{9.2}$$

For the electrons coming from a point-like source that have T_e lower than 300keV the dose rate can be calculated with the following formula:

$$H^o(\mu G/h) = 10^{-3} \times \frac{A(Bq) \times P}{d^2} \tag{9.3}$$

9.1 Nucleonica Dose Measurements

9.1.1 Gamma Ambient dose equivalent rate

According to the ICRP (International Commission on Radiological Protection), the ambient dose equivalent is defined as:

ICRP Publication 103 (ICRP, 2007):

"The dose equivalent at a point in a radiation field that would be produced by the corresponding expanded and aligned field in the ICRU sphere at a depth of 10 mm on the radius vector opposing the direction of the aligned field."

Ambient dose equivalent has the unit of joule per kilogram or Sievert (Sv).

On the other hand, H*(0.07) represents the equivalent dose at 0.07 mm below the surface of the body, otherwise named as skin dose.

In the same plot, the evolution of the dose rate H*10 as a function of the activity for distances of 0.1 cm, 1 cm, 10 cm and 40 cm for each radionuclide of interest for MEDICIS are shown in Figures 9.1a, 9.1b, 9.2a and 9.2b respectively.

The equations from the linear fit are given in Tables A.5 and A.6 in the Appendix.

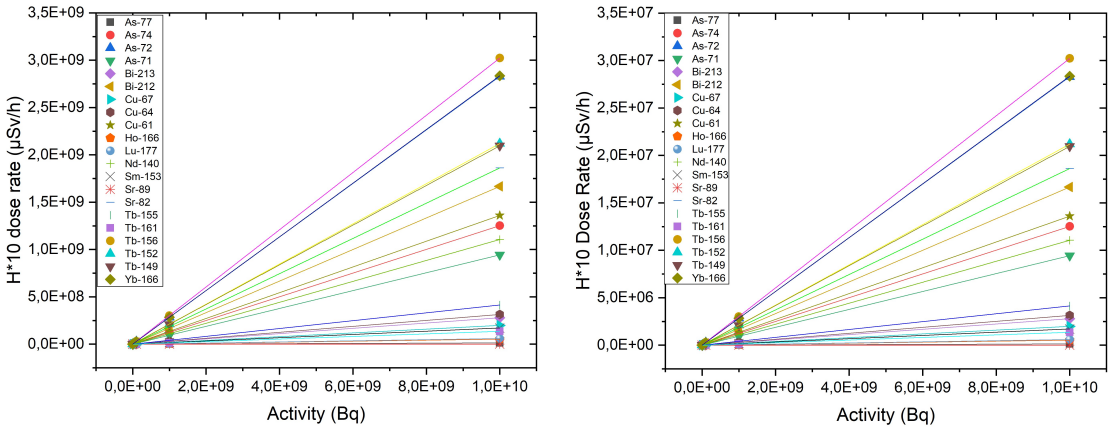

(a) H*10 as a function of Activity for 0.1cm distance

(b) H*10 as a function of Activity for 10cm distance

Figure 9.1 Gamma Ambient dose equivalent rate as a function of the activity.

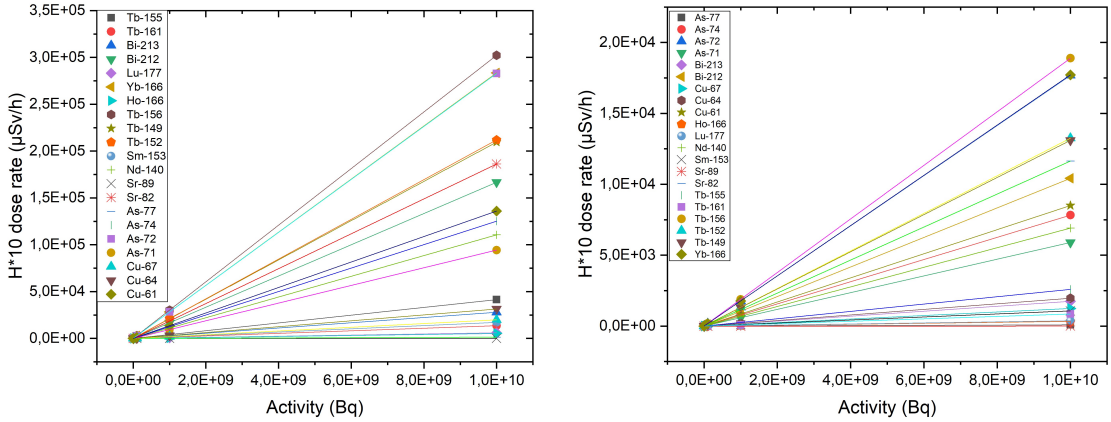

(a) H*10 as a function of Activity for 10cm distance

(b) H*10 as a function of Activity for 40cm distance

Figure 9.2 Gamma Ambient dose equivalent rate as a function of the activity.

9.1.2 Beta dose rate calculation

A graph showing the evolution of the activity versus the equivalent dose rate H*0.07 (for beta) at 10 cm and 40 cm with the linear fit equation are presented in Figure 9.3a and 9.3b. Distances less than 10 cm cannot be calculated with Nucleonica.

The equations from the linear fit are given in Table A.7 in the Appendix.

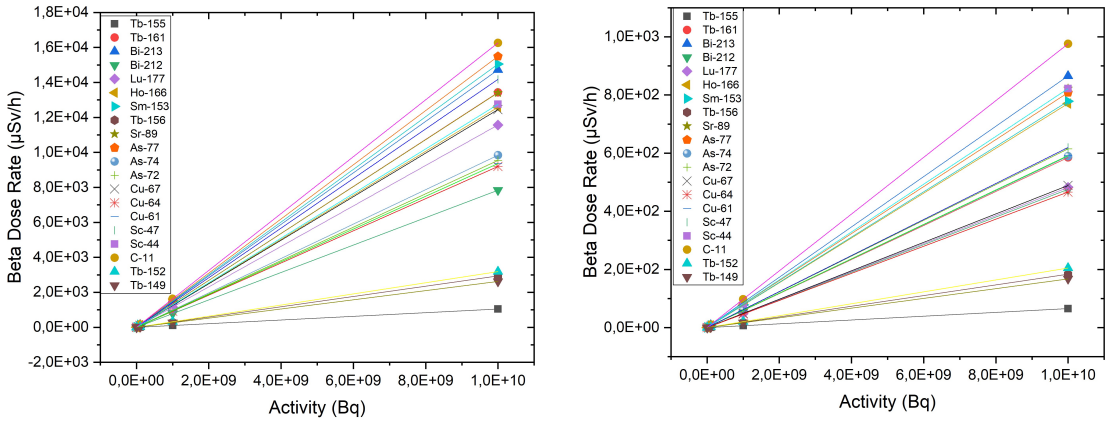

(a) H*0.07 as a function of Activity for a distance of 10cm

(b) H*0.07 as a function of Activity for a distance of 40cm

Figure 9.3 Beta dose equivalent rate as a function of the activity. The dashed lines represent the linear fit from Origin.

9.2 Simulations of Dose

PENMAIN is able to provide the absorbed dose distribution in a box with edges parallel to the laboratory frame axes. The user can determine the size of the dose box by using the commands: GRIDX, GRIDY and GRIDZ that define the coordinates of the vertices of the dose box. Furthermore, the dose is calculated thanks to an orthogonal grid defined the command GRIDBN, where the numbers of the bins are defined by NBDX, NBDY, NBDZ for the corresponding axes. In this case the GRIDX, GRIDY and GRIDZ are chosen to be between -10cm to 10cm and the bins were selected to be 55, as shown in Figure 8.2.

In Figures 9.4a and 9.4b, the simulated dose using GR-1 detector for the experimental configuration in MEDICIS is depicted for different radioisotopes. For this example the isotropic sources of Sm-153 and Lu-177 were simulated. It is obvious that the dose is distributed in a great amount at the golden foil which is situated at the beginning of the z axis and then less dose is distributed along the z axis, where the glass of the collection window and the detector are situated.

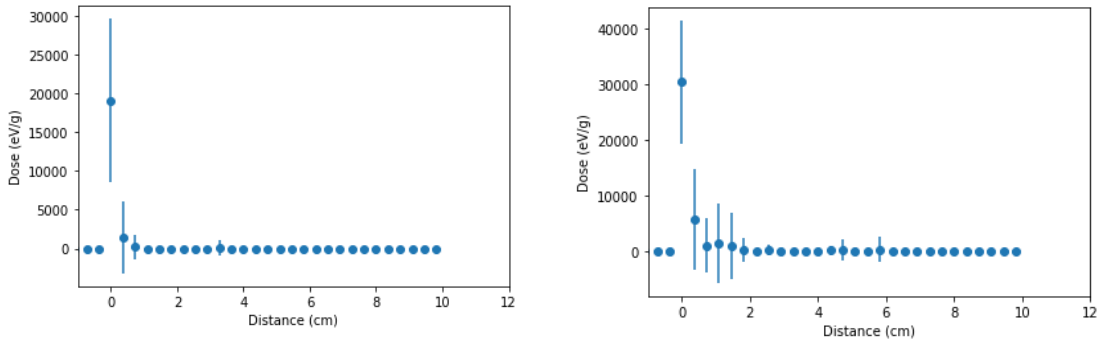

(a) Simulated dose distribution for Sm-153

(b) Simulated dose distribution for Lu-177

Figure 9.4 Dose distribution (eV/g) on z axis of the simulation, depicting the MEDICIS laboratory configuration for different radioisotopes.

9.3 Conclusions

To conclude the study of the dose measurements, an interactive excel file containing all the linear fits shown in the appendix, was created to be used by the technicians at MEDICIS site at CERN. This interactive excel file is user friendly. The user needs to simply choose a radionuclide from a given list, insert the activity in Bq and the distance in which they desire to acquire the dose rate. Then, the excel file can calculate the dose rate (either beta or gamma ambient equivalent dose rate) for the given parameters. Furthermore, the assessment of the accumulated dose at the golden foils was simulated for two of the radioisotopes of interest in MEDICIS (Lu-177 and Sm-153).

Chapter Ten

Conclusions of Thesis

The online activity measurements at MEDICIS laboratory during the extraction of radioactive ion beams is an application, where a better resolution than the one achieved with scintillators is needed, but cryogenic cooling (required for the operation of semiconductors like HPGe) is not practical. The ideal detector for such application would need to have a band gap much larger than that of Si or Ge and constituents with high atomic number and density, due to the fact that photoelectric cross-section depends on Z and because attenuation is proportional to density. This allows a much smaller detector volume for equal stopping power. The most suitable option appears to be the use of CZT detectors, which provide good energy resolution, good efficiency and high count rate capability at room temperature without the need of cooling.

Resulting from the experimental analysis of GR-1 and GR-05, it is safe to conclude that the GR-05 model should be employed for the radiochemistry procedure at MEDICIS laboratory. During the radiochemistry steps the detector has to be very close to the radioactive source. Therefore, a detector with high count capability is required. The GR-05 model is more suitable than the GR-1 model, as it was shown that it was able to minimize the dead time. On the other hand, the GR-1 model could be used outside of the window of the collection chamber during the production of radioisotopes at MEDICIS. Indeed, after recreating the experimental configuration of the collection chamber at MEDICIS laboratory,

it was shown that the GR-1 model provided higher efficiency measurements that the GR-05 detector. This was also verified with simulations using PENMAIN.

Furthermore, a thorough characterization of the CZT detector was performed by fitting the acquired efficiency curves using the chi-square fitting method from SATLAS package with Python and Cubic Spline fit with Origin. The fit from the efficiency curves allowed to calculate the expected activity of the certified sources that were used with small percentage difference from the actual activity of the order of 10%. Cubic Spline fit of the efficiency curve seemed to provide a better estimation of the activity. Additionally, the calculation of the efficiency curves and their fit was performed for a lower position of the GR-1 detector (1.25 cm below the center of the window of the collection chamber). The results between the two different positions were analysed and it was deemed that there is negligible difference. Thus, the GR-1 CZT detector can be placed below the center of the collection window in order to leave space for the camera. These experimental results were verified with simulations using PENMAIN. Indeed, when the MEDICIS facility restarted with the extraction of radioactive ion beams in May 2020, collecting five bunches of radioactive isotopes in total, the implementation of GR-1 detector at the lower position proved to provide a very good estimation of the activity implanted on the foils.

Another measurement was performed to ensure that there is negligible difference in the activity measurement if there is a produced radioisotope next to the desired one. For this purpose, two sources were placed next to each other behind the collection foils. It was proven that there was indeed a very small effect on the γ-ray spectrum that did not affect the activity calculation.

An interactive excel providing results for the equivalent dose rates (beta and gamma ambient) of the produced radioisotopes at MEDICIS was created by taking into account the theoretical calculations from Nucleonica. Moreover, dose distribution measurements were possible with PENMAIN along the axis of the experimental configuration. From this simulations it is possible to acquire the accumulated dose at the collection golden foils for

the radioisotopes of interest in MEDICIS.

Other CZT detectors (SDP500S, LAB CPG and SPEAR) were tested in Complutense University of Madrid to check whether their performance is comparable to GR-1 model from KROMEK. In particular, their energy resolution, Peak to Compton ratio, count rate and efficiencies were analyzed. It was concluded that both SDP500S and LAB CPG detectors are suitable options for the activity measurements at MEDICIS, as they provide high energy resolution, high efficiency, good Peak to Compton ratio and a nice approximation of the activity of the certified sources that were used. However, SPEAR detector was proved to be insufficient for the required spectral measurements.

Finally, PENMAIN simulations allowed to reproduce the experimental measurements successfully and provided an insight on the effect of the distance and the materials on the efficiency of the CZT crystal for different types of detectors (GR-1, GR-05 and SDP500S). The simulations matched the experimental results after some modifications of the parameters specified from the manufacturer in the case of GR-1 and GR-05. In particular, for GR-1 and GR-05 the simulated results approximated within 30% the experimental results only for a reduction of 27% of the crystal volume. PENMAIN was proven able to simulate reliably any new situation at MEDICIS, with different distances and positions of the detector checked. The possibility of using a simulation to approximate the experimental results with different thickness of the materials between the source and the detector was also checked. Further improvements of the simulations in PENMAIN could include the study of more geometries with different composition and thickness of the materials. For future studies it is suggested to check the CZT detectors from Complutense University of Madrid at MEDICIS laboratory.

REFERENCES

AMPTEK (2001). *Application Note (ANCZT-2 Rev. 1)*. http://www.ndtnet.com/m/amptek/anczt2.html#ref1.

Augusto, R. S. et al. (2014). "CERN-MEDICIS (Medical Isotopes Collected from ISOLDE): A New Facility". In: *Applied Sciences, 4(2):265–281*.

Awadalla, Salah (2017). *Solid-State Radiation Detectors*. CRC Press. ISBN: 9781351830904.

Baeta, Alexandra (2019). *Stable Isotope Ecology*. in Encyclopedia of Ecology (Second Edition).

Bergstrom, P.M. and R.H. Pratt (July 1997). "AN OVERVIEW OF THE THEORIES USED IN COMPTON SCATTERING CALCULATIONS". In: *Radiation Physics and Chemistry*, Elsevier.

Buchtela, K. (2019). "RADIOCHEMICAL METHODS | Gamma-Ray Spectrometry". In: *Encyclopedia of Analytical Science (Third Edition)*.

CAEN, Educational Handbook (2018). *Nuclear and Particle Physics Experiments*. CAEN SpA.

Carter, Matt (2015). *Visualizing Neural Structure*. Guide to Research Techniques in Neuroscience (Second Edition).

CERN (2011). *Map of the CERN accelerator complex*. http://public-archive.web.cern.ch/public-archive/en/research/AccelComplex-en.html.

CERN-MEDICIS, Open Days (2019).

Compton, A.H. (1923). "The spectrum of scattered X-rays". In: *Phys. Rev., 22 (1923), p. 409*.

CZT Technology: Fundamentals and Applications (2011). www.gehealthcare.com.

Debye, P. (1915). "Zerstreuung von Röntgenstrahlen und quantentheorie Physik". In: *Wiley Online Library, Volume 351, Issue 6, Pages 809-823*.

Duchemin, Charlotte (2015). *Etude de voies alternatives pour la production de radionuclides innovants pour les applicationes medicales*. PhD Thesis University of Nantes, France.

Gadelshina, V. M. et al. (2019). "MELISSA: Laser ion source setup at CERN-MEDICIS facility." In: *Nuclear Inst. and Methods in Physics Research.*

Gilmore, Gordon (2008). *Practical Gamma-Ray Spectroscopy.* John Wiley Sons, Incorporated.

Gins, W. et al. (2018). "Analysis of counting data: Development of the SATLAS Python package". In: *Computer Physics Communications, 222:286 – 294.*

Huebener, R.P. (2016). *Less Can Be More: Semiconductors. In: Conductors, Semiconductors, Superconductors.* Undergraduate Lecture Notes in Physics. Springer, Cham.

IAEA (2016). *Good Practice for Introducing Radiopharmaceuticals for Clinical Use.* IAEA-TECDOC-1782, IAEA, Vienna. DOI: 10.1109/IEEESTD.1997.82400.

ICRP (2007). *The 2007 Recommendations of the International Commission on Radiological Protectione.* ICRP Publication 103. Ann. ICRP 37 (2-4).

IEEE (1997). *IEEE Standard Test Procedures for Germanium Gamma-Ray Detectors.* IEEE Std 325-1996, vol., no., pp.0_1. DOI: 10.1109/IEEESTD.1997.82400.

Issam, Mouhti et al. (June 2018). "Validation of a NaI(Tl) and LaBr 3 (Ce) detector's models via measurements and Monte Carlo simulations". In: 11, pp. 335–339. DOI: 10.1016/j.jrras.2018.06.003.

Ivanov, V. et al. (2009). *CZT quasi-hemispherical detectors with improved spectrometric characteristics.* IEEE.

Knoll, Glenn F. (2000). *Radiation Detection and Measurement.* John Wiley and Sons, Inc, 3rd ed.

Koskelo, Markku J., Pertti A. Aarnio, and Jorma T. Routti (1981). "SAMPO80: An accurate gamma spectrum analysis method for minicomputers". In: *Nuclear Instruments and Methods in Physics Research* 190 (1), pp. 89–99.

Kromek (2020). *About CZT: cadmium zinc telluride.* https://www.kromek.com/cadmium-zinc-telluride-czt/.

L'Annunziata, Michael F. (2012). "Radiation Physics and Radionuclide Decay". In: *Handbook of Radioactivity Analysis (Third Edition).*

Laboratoire National Henri Becquerel (last updated 2017-03-03). http://www.lnhb.fr/nuclear-data/.

Liu, Zeke, Wanli Ma, and Xing chen Ye (2018). *Anisotropic Particle Assemblies Synthesis, Assembly, Modeling, and Applications, Pages 37-54, Chapter 2:Shape control in the synthesis of colloidal semiconductor nanocrystals.* Elsevier.

Masterson, Robert (2017). *Nuclear engineering fundamentals : a practical perspective.* OCLC.

Mirion (2019). *LAB CPG - CZT COPLANAR GRID DETECTOR, spec-sheets.*

Müller, C. et al. (2016). *Alpha-PET with terbium-149: evidence and perspectives for radiotheragnostics.* JEJNMMI Radiopharmacy and Chemistry, 1(1):5.

Myers, H. P. (1997). *Introductory Solid State Physics.* CRC Press LLC.

Nijran, Kuldip S. (2017). *Diagnostic Radioisotopes in Haematology.* Dacie and Lewis Practical Haematology (Twelfth Edition).

Nucleonica (2011). *Nucleonical web driven nuclear science.* https://www.nucleonica.com/.

OriginLab (updated 2020). https://www.originlab.com/doc/Origin-Help/Math-Inter-Extrapoltate-YfromX.

Orsini, F., F. Guidoccio, and G. Mariani (2019). *Radiopharmaceuticals for Therapy.* Nuclear Medicine Textbook. Springer, Cham.

Palenzuela, Yisel Martinez (2019). "Characterization and optimization of a versatile laser and electron-impact ion source for radioactive ion beam production at ISOLDE and MEDICIS". In: *Dissertation presented in partial fulfillment of the requirements for the degree of Doctor of Science (PhD): Physics.*

Peyres, V. and E. Garcı a-Tora (2007). "Efficiency calibration of an extended-range Ge detector by a detailed Monte Carlo simulation". In: *Nuclear Instruments and Methods in Physics Research A 580 296–298.*

Phelan, W. Earl (1968). *Radioisotopes in Medicine.* U.S. ATOMIC ENERGY COMMISSION / Division of Technical Information.

RITEC (updated 2020). *Nuclear Radiation and Semiconductor Detectors and associated electronics.* http://www.ritec.lv/.

— (n.d.). *LARGE VOLUME HEMISPHERICAL NUCLEAR RADIATION DETECTOR Model CZT/500 User Manual.*

Sadeghi, Soheil (Dec. 2016). "Nitrogen-Doped Carbon Nanotube/Polymer Nanocomposites Towards Thermoelectric Applications". In: pp. 325–350. ISBN: 978-953-51-2845-8. DOI: 10.5772/65675.

Salgado, C. M. et al. (2012). "Validation of a NaI(Tl) detector's model developed with MCNP-X code". In: *Progress in Nuclear Energy* 59, pp. 19–25.

Salvat, Francesc, Jose M Fernandez-Varea, and Josep Sempau (2011). *PENELOPE-2011: A Code System for Monte Carlo Simulation of Electron and Photon transport.* Workshop Proceedings-Barcelona, Spain.

Schlesinger, T. E. et al. (2001). *Cadmium zinc telluride and its use as a nuclear radiation detector material.* Mater. Sci. Eng. R 32 103.

Sordo, Stefano Del et al. (2009). *Progress in the Development of CdTe and CdZnTe Semiconductor Radiation Detectors for Astrophysical and Medical Applications*. sensors, ISSN 1424-8220 www.mdpi.com/journal/sensors.

Tajudin, Suffian Mohamad et al. (2019). "Full-energy peak efficiency and response function of 1 cm3 CdZnTe detectors". In: *Malaysian Journal of Fundamental and Applied Sciences Vol. 15, No. 4 (2019) 580-584*.

Taylor, John R. (1997). *An Introduction to Error Analysis: The Study of Uncertainties in Physical Measurements*. University Science Books, Sausalito, California.

Vichi, Sara et al. (2016a). *An innovative gamma-ray spectrometry system using a compact and portable CZT detector for radionuclidic purity tests of PET radiopharmaceuticals*. Radiat. Eff. 171 (2016) 726-735.

— (2016b). *Efficiency calibration of a portable CZT detector for nondestructive activation assessment of a cyclotron bunker*. Radiat. Eff. 171 705-713.

Waterstram-Rich, Kristen M. and Paul E. Christian (2013). *Nuclear Medicine and PET/CT - E-Book: Technology and Techniques*. Elsevier Mosby 7th edition.

Wheat, J.M. et al. (2011). *An introduction to nuclear medicine*. Australian Society of Medical Imaging and Radiation Therapy. Volume 58 (3).

Zanio, K. R. (1978). *Cadmium telluride, in: Semiconductors and Semimetals.* Vol. 13, New York: Academic Press.

Appendix A

APPENDIX

In case of radioisotopes with lower energy gamma emissions than 121.8 keV, as the ones presented in this report, it was needed to extrapolate. Origin allows to extrapolate the cubic spline fit as shown in Figure A.2 with the red line.

The advantage of SATLAS fit is that the efficiency values for lower energies can be calculated without the need of extrapolation, as the user can simply calculate it by using equation 5.5 with the appropriate fitting parameters (see Tables of fitting parameters in the report).

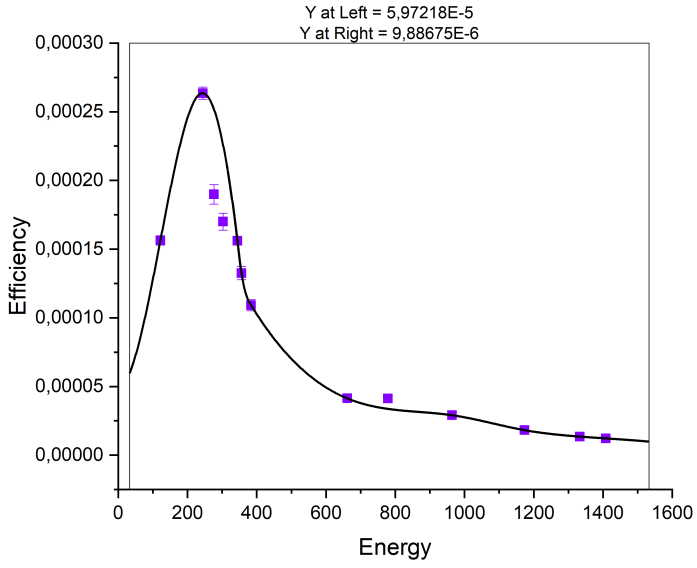

Figure A.1 Cubic Spline Fit of the efficiency curve for the middle position of the detector. The weighted mean values of two methods were used (FitzPeaks and manually assigned peaks using Multispect Software).In this graph the extrapolation of the values can be seen.

Table A.1 Extrapolated values from Cubic Spline fit using the weighted mean values of the efficiency from Fitzpeaks Software and Manually assigned peaks in Multispect Software for the middle position of the detector.

Energy (keV)	Efficiency	Energy (keV)	Efficiency
32,81	3,724E-5	61,34	5,871E-5
34,31	3,775E-5	62,84	6,045E-5
35,81	3,833E-5	64,34	6,224E-5
37,31	3,899E-5	65,84	6,408E-5
38,82	3,972E-5	67,34	6,597E-5
40,32	4,053E-5	68,85	6,791E-5
41,82	4,141E-5	70,34	6,989E-5
43,32	4,235E-5	71,85	7,192E-5
44,82	4,337E-5	73,35	7,400E-5
46,32	4,445E-5	74,85	7,611E-5
47,82	4,561E-5	76,35	7,827E-5
49,32	4,682E-5	77,85	8,047E-5
50,82	4,809E-5	79,36	8,271E-5
52,33	4,944E-5	80,86	8,498E-5
53,83	5,084E-5	82,36	8,728E-5
55,33	5,230E-5	83,86	8,963E-5
56,84	5,382E-5	85,36	9,201E-5
58,34	5,539E-5	86,86	9,441E-5
59,84	5,703E-5	88,37	9,685E-5
61,34	5,871E-5	89,87	9,932E-5
62,84	6,045E-5	91,37	1,018E-4
64,34	6,224E-5	92,87	1,043E-4
65,84	6,408E-5	94,37	1,068E-4
67,34	6,597E-5	95,87	1,094E-4
68,84	6,791E-5	97,37	1,120E-4
70,35	6,989E-5	98,88	1,146E-4
71,85	7,192E-5	100,38	1,173E-4
73,35	7,40019E-5	101,88	1,199E-4
74,85	7,612E-5	103,38	1,226E-4
76,35	7,827E-5	104,88	1,253E-4
77,85	8,047E-5	106,38	1,280E-4
79,36	8,271E-5	107,89	1,307E-4
80,86	8,498E-5	109,39	1,335E-4
82,36	8,728E-5	110,89	1,362E-4
83,86	8,963E-5	112,39	1,389E-4
85,37	9,201E-5	113,89	1,417E-4
86,87	9,441E-5	115,39	1,445E-4
88,37	9,685E-5	116,89	1,472E-4
89,87	9,932E-5	118,40	1,501E-4
91,37	1,018E-4	119,90	1,528E-4

Table A.2 Interpolated values from Cubic Spline fit using the weighted mean values of the efficiency from Fitzpeaks Software and Manually assigned peaks in Multispect Software for the middle position of the detector.

Energy (keV)	Efficiency	Energy (keV)	Efficiency
121,80	1,563E-4	758,40	4,129E-5
134,79	1,865E-4	771,39	4,138E-5
147,78	2,153E-4	784,38	4,131E-5
160,78	2,417E-4	797,37	4,105E-5
173,77	2,642E-4	810,37	4,063E-5
186,75	2,816E-4	823,36	4,006E-5
199,75	2,926E-4	836,35	3,935E-5
212,74	2,959E-4	849,34	3,853E-5
225,74	2,903E-4	862,33	3,761E-5
238,73	2,746E-4	875,33	3,662E-5
251,72	2,476E-4	888,32	3,556E-5
264,71	2,149E-4	901,31	3,446E-5
277,70	1,877E-4	914,31	3,334E-5
290,69	1,735E-4	927,29	3,221E-5
303,68	1,699E-4	940,29	3,109E-5
316,67	1,718E-4	953,28	3,0001E-5
329,67	1,705E-4	966,28	2,895E-5
342,66	1,587E-4	979,27	2,796E-5
355,65	1,333E-4	992,25	2,703E-5
368,65	1,167E-4	1005,25	2,616E-5
381,64	1,099E-4	1018,24	2,534E-5
394,63	1,053E-4	1031,23	2,456E-5
407,62	1,008E-4	1044,22	2,382E-5
420,61	9,637E-5	1057,21	2,314E-5
433,61	9,197E-5	1070,21	2,248E-5
446,59	8,767E-5	1083,20	2,186E-5
459,59	8,346E-5	1096,19	2,128E-5
472,58	7,937E-5	1109,18	2,072E-5
485,57	7,541E-5	1122,17	2,018E-5
498,56	7,158E-5	1135,16	1,967E-5
511,56	6,792E-5	1148,16	1,917E-5
524,55	6,442E-5	1161,15	1,869E-5
537,54	6,111E-5	1174,14	1,823E-5
550,53	5,799E-5	1187,13	1,776E-5
563,52	5,508E-5	1200,13	1,731E-5
576,52	5,240E-5	1213,12	1,687E-5
589,51	4,996E-5	1226,11	1,645E-5
602,50	4,777E-5	1239,11	1,603E-5
615,49	4,585E-5	1252,09	1,564E-5
628,48	4,421E-5	1265,08	1,525E-5
641,48	4,286E-5	1278,08	1,489E-5
654,46	4,182E-5	1291,07	1,454E-5
667,46	4,109E-5	1304,06	1,421E-5
680,45	4,068E-5	1317,05	1,391E-5
693,44	4,050E-5	1330,04	1,362E-5
706,44	4,052E-5	1343,04	1,335E-5
719,43	4,066E-5	1356,03	1,310E-5
732,42	4,088E-5	1369,02	1,287E-5
745,41	4,111E-5	1382,01	1,265E-5

Table A.3 Interpolated values from Cubic Spline fit using the weighted mean values of the efficiency from Fitzpeaks Software and Manually assigned peaks in Multispect Software for the lower position of the detector

Energy (keV)	Efficiency	Energy (keV)	Efficiency
121,80	1,28E-04	771,39	3,07E-05
134,79	1,51E-04	784,38	2,98E-05
147,78	1,73E-04	797,37	2,89E-05
160,77	1,93E-04	810,37	2,81E-05
173,76	2,12E-04	823,36	2,74E-05
186,75	2,29E-04	836,35	2,67E-05
199,75	2,43E-04	849,34	2,61E-05
212,74	2,54E-04	862,33	2,55E-05
225,73	2,61E-04	875,33	2,49E-05
238,72	2,63E-04	888,32	2,44E-05
251,71	2,61E-04	901,31	2,39E-05
264,71	2,53E-04	914,31	2,35E-05
277,70	2,42E-04	927,29	2,31E-05
290,69	2,28E-04	940,29	2,27E-05
303,68	2,12E-04	953,28	2,24E-05
316,67	1,94E-04	966,27	2,20E-05
329,67	1,77E-04	979,26	2,17E-05
342,66	1,59E-04	992,26	2,14E-05
355,65	1,43E-04	1005,25	2,11E-05
368,64	1,29E-04	1018,24	2,08E-05
381,63	1,16E-04	1031,23	2,05E-05
394,63	1,04E-04	1044,23	2,03E-05
407,62	9,37E-05	1057,22	2,00E-05
420,61	8,44E-05	1070,21	1,98E-05
433,60	7,62E-05	1083,20	1,96E-05
446,59	6,90E-05	1096,19	1,94E-05
459,58	6,28E-05	1109,18	1,92E-05
472,58	5,75E-05	1122,17	1,90E-05
485,57	5,30E-05	1135,17	1,89E-05
498,56	4,93E-05	1148,16	1,87E-05
511,55	4,63E-05	1161,15	1,86E-05
524,54	4,39E-05	1174,14	1,85E-05
537,54	4,20E-05	1187,14	1,83E-05
550,53	4,06E-05	1200,13	1,82E-05
563,52	3,96E-05	1213,12	1,81E-05
576,51	3,89E-05	1226,11	1,80E-05
589,51	3,85E-05	1239,11	1,79E-05
602,50	3,83E-05	1252,09	1,77E-05
615,49	3,82E-05	1265,09	1,76E-05
628,48	3,82E-05	1278,08	1,74E-05
641,47	3,81E-05	1291,07	1,71E-05
654,46	3,79E-05	1304,06	1,68E-05
667,46	3,76E-05	1317,06	1,65E-05
680,45	3,71E-05	1330,05	1,61E-05
693,44	3,64E-05	1343,04	1,56E-05
706,43	3,56E-05	1356,03	1,50E-05
719,43	3,47E-05	1369,02	1,44E-05
732,42	3,38E-05	1382,02	1,38E-05
745,41	3,28E-05	1395,01	1,32E-05
758,40	3,17E-05	1408,00	1,25E-05

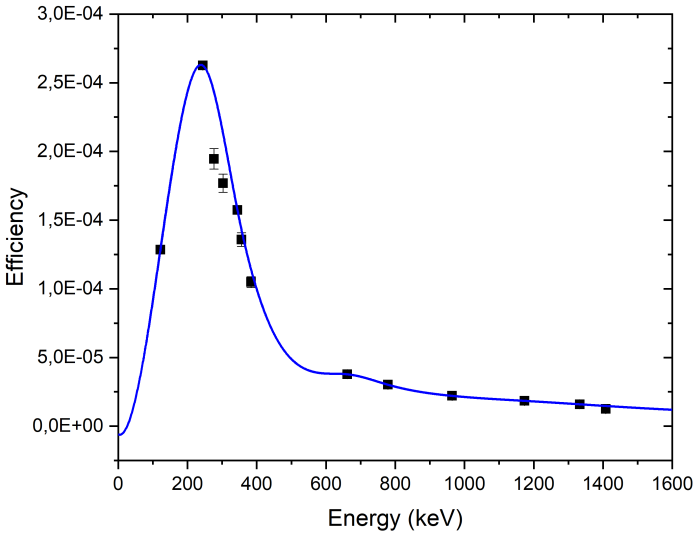

Figure A.2 Cubic Spline Fit of the efficiency curve for the lower position of the detector. The weighted mean values of two methods were used (FitzPeaks and manually assigned peaks using Multispect Software). In this graph the extrapolation of the values can be seen.

Table A.4 Extrapolated values from Cubic Spline fit using the weighted mean values of the efficiency from Fitzpeaks Software and Manually assigned peaks in Multispect Software for the lower position of the detector

Energy (keV)	Efficiency	Energy (keV)	Efficiency
28,85	1,81E-06	73,75	5,02E-05
32,06	3,97E-06	76,95	5,49E-05
35,27	6,36E-06	80,16	5,96E-05
38,47	8,98E-06	83,36	6,45E-05
41,68	1,18E-05	86,57	6,95E-05
44,88	1,49E-05	89,77	7,46E-05
48,09	1,81E-05	92,98	7,97E-05
51,30	2,15E-05	96,19	8,50E-05
54,51	2,51E-05	99,39	9,03E-05
57,72	2,89E-05	102,61	9,56E-05
60,92	3,29E-05	105,81	1,01E-04
64,13	3,70E-05	109,02	1,06E-04
67,33	4,13E-05	112,22	1,12E-04
70,54	4,57E-05	115,43	1,17E-04

Table A.5 Linear fit equations from the Gamma ambient dose rate as a function of the Activity in Bq

Source	Distance(cm)	Equation	Source	Distance(cm)	Equation
As-77	0.1	y = 1.4e-03x	Cu-64	0.1	y = 3.14e-02x - 1e-08
As-77	1	y = 1e-05x - 6e-12	Cu-64	1	y = 3e-04x
As-77	10	y = 1e-07x	Cu-64	10	y = 3e-06x + 1e-12
As-77	40	y = 9e-09x	Cu-64	40	y = 2e-07x
As-72	0.1	y = 2.8e-01x - 2e-07	Cu-67	0.1	y = 1.99e-02x
As-72	1	y = 2.8e-03x	Cu-67	1	y = 2e-04x - 9e-11
As-72	10	y = 3e-05x	Cu-67	10	y = 2e-06x
As-72	40	y = 2e-06x	Cu-67	40	y = 1e-07x - 4e-14
As-74	0.1	y = 1.252e-01x	As-71	0.1	y = 9.44e-02x - 5e-08
As-74	1	y = 1.3e-02x	As-71	1	y = 9e-04x
As-74	10	y = 1e-05x	As-71	10	y = 9e-06x
As-74	40	y = 8e-07x - 4e-13	As-71	40	y = 6e-07x - 4e-13
Bi-212	0.1	y = 1.67e-01x	Ho-166	0.1	y = 5.3e-02x - 3e-09
Bi-212	1	y = 1.7e-03x	Ho-166	1	y = 5.3e-05x - 2e-11
Bi-212	10	y = 2e-05x	Ho-166	10	y = 5.3e-07x
Bi-212	40	y = 1e-06x	Ho-166	40	y = 3e-08x
Bi-213	0.1	y = 2.8E-02x	Lu-177	0.1	y = 6e-03x
Bi-213	1	y = 3e-04x	Lu-177	1	y = 6e-05x - 2e-11
Bi-213	10	y = 3e-06x - 1e-12	Lu-177	10	y = 6e-07x
Bi-213	40	y = 2e-07x	Lu-177	40	y = 4e-08x - 2e-14
Cu-61	0.1	y = 1.36e-01x - 5e-08	Nd-140	0.1	y = 1.11e-01
Cu-61	1	y = 1.4e-03x	Nd-140	1	y = 1.1e-02 - 7e-07
Cu-61	10	y = 1e-05x	Nd-140	10	y = 1e-05
Cu-61	40	y = 9e-07x	Nd-140	40	y = 7e-07 - 4e-13

Table A.6 Linear fit equations from the Gamma ambient dose rate as a function of the Activity in Bq (Continued)

Source	Distance (cm)	Equation	Source	Distance (cm)	Equation
Sm-153	0.1	y = 1.72e-02x - 6e-09	Tb-155	0.1	y = 4.14e-02x
Sm-153	1	y = 2e-04x	Tb-155	1	y = 4e-04x
Sm-153	10	y = 2e-06x - 7e-13	Tb-161	10	y = 1e-06x
Sm-153	40	y = 1e-07x + 4e-14	Tb-161	40	y = 9e-08x - 4e-14
Sr-82	0.1	y = 1.862e-01x	Tb-155	10	y = 4e-06x
Sr-82	1	y = 1.9e-03x - 7e-10	Tb-155	40	y = 3e-07x
Sr-82	10	y = 2e-05x	Tb-156	0.1	y = 3.02e-01x
Sr-82	40	y = 1e-06x - 7e-13	Tb-156	1	y = 3e-03x
Sr-89	0.1	y = 3e-05x	Tb-156	10	y = 3e-05x -1e-11
Sr-89	1	y = 3e-07x	Tb-156	40	y = 2e-06x
Sr-89	10	y = 3e-09x	Yb-166	0.1	y = 2.835e-01x - 2e-07
Sr-89	40	y = 2e-10x	Yb-166	1	y = 2.8e-03x
Tb-149	0.1	y = 2.096e-01x	Yb-166	10	y = 3e-05x -1e-11
Tb-149	1	y = 2.1e-03x	Yb-166	40	y = 2e-06x - 7e-13
Tb-149	10	y = 2e-05x - 1e-11	Tb-152	10	y = 2e-05x
Tb-149	40	y = 2.096e-01x	Tb-152	40	y = 1e-06x
Tb-152	0.1	y = 2.119e-01x + 9e-08	Tb-152	1	y = 2.1e-04x

Table A.7 Linear fit equations from the Beta ambient dose rate as a function of the Activity in Bq

Source	Distance (cm)	Equation	Source	Distance (cm)	Equation
As-71	10	0	Nd-140	10	0
As-71	40	0	Nd-140	40	0
As-72	10	$y = 1e-06x$	Sm-153	10	$y = 2e-06x$
As-72	40	$y = 6e-08x-2e-14$	Sm-153	40	$y = 8e-08x$
As-74	10	$y = 1e-06x$	Sr-82	10	0
As-74	40	$y = 6e-08x-2e-14$	Sr-82	40	0
As-77	10	$y = 2e-06x$	Sr-89	10	$y = 1e-06x$
As-77	40	$y = 8e-08x$	Sr-89	40	$y = 8e-08x$
Bi-212	10	$y = 8e-07x$	Tb-152	10	$y = 3e-07x$
Bi-212	40	$y = 5e-08x$	Tb-152	40	$y = 2e-08x$
Bi-213	10	$y = 1e-06x$	Tb-149	10	$y = 3e-07x+9e-14$
Bi-213	40	$y = 9e-08x-4e-14$	Tb-149	40	$y = 2e-08x-5e-15$
Cu-61	10	$y = 9e-07x-4e-15$	Tb-156	10	$y = 3e-07x$
Cu-61	40	$y = 6e-08x-2e-14$	Tb-156	40	$y = 2e-08x$
Cu-64	10	$y = 9e-07x$	Tb-161	10	$y = 1e-06x-7e-13$
Cu-64	40	$y = 5e-08x$	Tb-161	40	$y = 6E-08x$
Cu-67	10	$y = 1e-06x-7e-13$	Yb-166	10	0
Cu-67	40	$y = 5e-08x-2e-14$	Yb-166	40	0
Ho-166	10	$y = 1e-06x-7e-13$	Lu-177	10	$y = 1e-06x$
Ho-166	40	$y = 8e-08 \times x$	Lu-177	40	$y = 5e-08x$

```
....+....1....+....2....+....3....+....4....+....5....+....6....+....7
TITLE   Title of the job, up to 65 characters.
        . (the dot prevents editors from removing trailing blanks)
        >>>>>>>> Source definition.
SKPAR   KPARP     [Primary particles: 1=electron, 2=photon, 3=positron]
SENERG  SEO                 [Initial energy (monoenergetic sources only)]
SPECTR  Ei,Pi                     [E bin: lower-end and total probability]
SGPOL   SP1,SP2,SP3           [Stokes parameters for polarised photons]
SPOSIT  SXO,SYO,SZO                        [Coordinates of the source]
SBOX    SSX,SSY,SSZ                              [Source box dimensions]
SBODY   KB                [Active source body; one line for each body]
SCONE   THETA,PHI,ALPHA                      [Conical beam; angles in deg]
SPYRAM  THETAL,THETAU,PHIL,PHIU       [Rectangular beam; angles in deg]
        .
        >>>>>>>> Input phase-space file (psf).
IPSFN   psf-filename.ext          [Input psf name, up to 20 characters]
IPSPLI  NSPLIT                                        [Splitting number]
WGTWIN  WGMIN,WGMAX           [Weight window, RR & spl of psf particles]
EPMAX   EPMAX                  [Maximum energy of particles in the psf]
        .
        >>>>>>>> Material data and simulation parameters.
                 Up to MAXMAT materials; 2 lines for each material.
MFNAME  mat-filename.ext                    [Material file, up to 20 chars]
MSIMPA  EABS(1:3),C1,C2,WCC,WCR                 [EABS(1:3),C1,C2,WCC,WCR]
        .
        >>>>>>>> Geometry and local simulation parameters.
GEOMFN  geo-filename.ext                    [Geometry file, up to 20 chars]
DSMAX   KB,DSMAX(KB)                 [KB, maximum step length in body KB]
EABSB   KB,EABSB(1:3,KB)    [KB, local absorption energies, EABSB(1:3)]
        .
        >>>>>>>> Interaction forcing.
IFORCE  KB,KPAR,ICOL,FORCER,WLOW,WHIG   [KB,KPAR,ICOL,FORCER,WLOW,WHIG]
        .
        >>>>>>>> Emerging particles. Energy and angular distributions.
NBE     EL,EU,NBE                          [Energy window and no. of bins]
NBANGL  NBTH,NBPH             [Nos. of bins for the angles THETA and PHI]
        .
        >>>>>>>> Impact detectors (up to 25 different detectors).
        IPSF=0; no psf is created.
        IPSF=1; the psf is created.
        IDCUT=0; tracking is discontinued at the detector entrance.
        IDCUT=1; the detector does not affect the tracking.
        IDCUT=2; the detector does not affect tracking, the energy
                 distribution of particle fluence (averaged over the
                 volume of the detector) is calculated.
IMPDET  EL,EU,NBE,IPSF,IDCUT       [E-window, no. of bins, IPSF, IDCUT]
IDSPC   spc-impdet-##.dat                  [Spectrum file name, 20 chars]
IDPSF   psf-impdet-##.dat              [Phase-space file name, 20 chars]
IDFLNC  fln-impdet-##.dat          [Fluence spectrum file name, 20 chars]
IDBODY  KB                          [Active body; one line for each body]
IDKPAR  KPAR                  [Kind of detected particles, one line each]
        .
        >>>>>>>> Energy-deposition detectors (up to 25).
ENDETC  EL,EU,NBE                      [Energy window and number of bins]
EDSPC   spc-enddet-##.dat           [Output spectrum file name, 20 chars]
EDBODY  KB                          [Active body; one line for each body]
        .
        >>>>>>>> Dose distribution.
GRIDY   YL,YU                     [Y coordinates of the dose box vertices]
GRIDZ   ZL,ZU                     [Z coordinates of the dose box vertices]
GRIDBN  NDBX,NDBY,NDBZ                                [Numbers of bins]
        .
        >>>>>>>> Job properties.
RESUME  dump1.dmp                 [Resume from this dump file, 20 chars]
DUMPTO  dump2.dmp                    [Generate this dump file, 20 chars]
DUMPP   DUMPP                                [Dumping period, in sec]
        .
RSEED   ISEED1,ISEED2             [Seeds of the random-number generator]
NSIMSH  DSHN                       [Desired number of simulated showers]
TIME    TIMEA                         [Allotted simulation time, in sec]
END                                    [Ends the reading of input data]
....+....1....+....2....+....3....+....4....+....5....+....6....+....7
```

Figure A.3 PENMAIN input file guideline